High Resolution X-Ray Observations of the Galactic Center Region

Hiroshi Murakami

Department of Physics. Graduate School of Science,
Kyoto University, Sakyo-ku, Kyoto 606-8502, Japan

Submitted to the Department of Physics,
Kyoto University on January 7, 2002,
for the degree of Doctor of Science (Physics)

Abstract

We present the *ASCA* and *Chandra* observations of diffuse X-ray structures in our Galactic center region. We concentrate on giant molecular clouds, supernova remnants, and other faint structures which are newly discovered with *Chandra*.

We observed four giant molecular clouds: Sgr B2, Sgr C, M0.11−0.08 (at the Radio Arc region), and Clump2. All clouds emit strong 6.4-keV line with the equivalent width of $\gtrsim$ 1 keV, and exhibit larger column densities than interstellar absorption. The distribution of the 6.4-keV line is coincident with molecular cloud. The distribution of Sgr B2 and Sgr C are shifted to the Galactic Center side, in particular. These features imply that heavy molecular clouds are irradiated by an external X-ray source in the direction of the Galactic center and emit fluorescent and scattered X-rays. We call this new category of X-ray source "X-ray Reflection Nebula".

Numerical simulations of X-ray reflection nebula model successfully reproduce the observed image and spectrum when the mass of the cloud is smaller than 0.3 times of the mass estimated by the radio observations of molecular lines. This result supports that the molecular clouds in the Galactic center are in pressure equilibrium, not in gravity equilibrium. The abundances of the clouds are also estimated by numerical simulations. The iron abundance and other lighter elements of the Sgr B2 cloud are estimated to be 1.5–3.0, and 2.0–5.0, respectively in case of cloud mass is 0.2 times of the radio estimated mass. The abundances of other clouds are not constrained in significant region. The lower limit of the iron abundance is 1.0 for all of the three clouds. The abundance of other lighter elements are constrained to be $\lesssim$ 1 for M0.11−0.08, and $\lesssim$ 3 for Sgr C and Clump 2.

The X-ray reflection nebula model are used to investigate the past activities of our Galactic center. The observed fluorescent and scattered X-rays from the molecular clouds reflect the past luminosity of the primary source, which would be the massive black hole Sgr A*. It was as luminous as 10^{39} erg s^{-1} $\sim 300 - 2000$ years ago. Then the luminosity decrease gradually to present value. This time variability agrees with the implication obtained by the *Chandra* observation of Sgr A East. Sgr A East is the 10^4-year-old supernova remnant, and the shock front passed by Sgr A* about 10^3 years ago. Large amount of matters accreted to Sgr A* in the passing time, and then surrounding materials are swept away.

At least three supernova remnants are discovered in the GC region with much higher angular resolution of *Chandra* than past X-ray observatories. The number of detected supernova remnants are insufficient to explain the total energy of the high temperature plasma in the GC

region.

Chandra discovered faint diffuse structures in the GC region. They are candidates of supernova remnants, X-ray reflection nebulae, or something else. Some of them exhibit non-thermal spectrum, and thought to be acceleration sites of high energy cosmic rays.

Contents

List of Figures

List of Tables

Chapter 1

Introduction

The center of our Galaxy, the Galactic center (GC, hereafter), is one of the most interesting targets in astronomy. A large amount of matter concentrates in this region: stars, molecular gas, H_{II} regions, neutron stars, supernova remnants, and so on. The GC is a peculiar region with these various objects. Although many observations have been made to understand the nature of the GC, there are many questions till now. The most puzzling problem is the massive black hole at the Galactic nucleus. The luminosity is anomalously low for the black hole with the mass of $2.6\times10^6 M_\odot$.

In X-ray band, Japanese X-ray satellites *Ginga* and *ASCA* had made important discoveries which imply the past activities in the GC region: a large scale high temperature plasma extending in a $1^\circ\!.8 \times 1^\circ\!.0$ region, and diffuse 6.4-keV line emission. The plasma contains the extremely large energy of 10^{54} erg, and 6.4-keV line suggests that there was a strong X-ray emitter in the GC region. They seem to be contradictory to the present quiescent nucleus. Following these results, *Chandra* is increasing the number of X-ray sources in the GC region with the extremely high angular resolution. These discoveries give us further information on the GC region.

In this thesis, we attempt to reveal the past activities of the GC region with the *ASCA* and *Chandra* observations. For the *ASCA* results, Maeda (1998) summarized the global distribution of X-ray emissions, in particular of emission lines, in the GC region. Then Sakano (2000) investigate the properties of X-ray point sources. Following these results, we mainly study about the discrete diffuse emissions in this thesis.

The main objectives are:

1. to reveal the emission mechanism of 6.4-keV line emissions,

2. to search an origin of the high temperature plasma,

3. to find new discrete diffuse sources.

The contents of this thesis are as follows. In chapter 2, we review the nature of our Galactic center region briefly. Then instruments and the details for observations are explained in chapter 3 and 4, respectively. In chapter 5–7, we report the results of the observations which are related to each item mentioned above. Finally, we discuss and summarize the results in chapter 8.

In this thesis, we assume the distance to the Galactic center to be 8.5 kpc. All the X-ray sources in the GC region are assumed to be at the same distance.

Chapter 2

Review

In this chapter, we review the nature of our Galactic center (GC) region. Because the GC region is highly complex with the various phenomena, we do not cover all the objects in this review. We give here only brief descriptions of the radio and X-ray sources which are closely related to our work. More detailed explanations are shown in already published reviews: e.g. Morris & Serabyn (1996), Mezger, Ducshl, & Zylka (1996), and Melia & Falcke (2001).

2.1 Overview

Optical and ultraviolet wavelengths are heavily absorbed by the interstellar matters along the Galactic disk, and can not penetrate from the GC region to us. We can observe the GC region with radio, infrared, X-ray and γ-ray wavelengths.

With the early radio observations, bright structures are detected, which are named Sgr A–E. The most luminous region, Sgr A, is the Galactic center (section 2.2). Then numerous radio observations have been made, and many objects are found; e.g. giant molecular clouds (GMC), non-thermal filaments, H_{II} regions, and so on. The distribution and the properties of molecular clouds are stated in section 2.3.

In the infrared band, the GC region is filled with many bright stars. The mass density of stars rises toward the Galactic center. There are many high mass stars at the close vicinity of the Galactic nucleus. For example, IRS 16 star cluster, which is at the central parsec of the Galaxy, is comprised of several O type stars (Simons, Hodapp, & Becklin 1990). These stars indicate that the star burst activity was occurred at the GC region within the past 10^7 years.

Also in X-ray band, the distinct features are X-ray point sources, the most of which are neutron star binaries or black hole candidates. Diffuse X-ray emissions also exist. Details for

X-ray observations are shown in section 2.4.

Some γ-ray observations revealed that the large amount of positrons exists in the GC region. The 511 keV line from positron annihilation is observed in many times (e.g. Johnson, Harnden, & Haymes 1972), and the distribution is comprised of three components: a central bulge, the Galactic plane, and an enhancement or extension of emission at positive latitudes above the Galactic center (Purcell et al. 1997; Kinzer et al. 2001). The origin of the positrons is not explained yet.

1.8 MeV line produced by the ^{26}Al decay is also detected from the GC region. The line emission is revealed to concentrate along the Galactic plane with the observation of COMPTEL onboard *CGRO*, and the origin of ^{26}Al is thought to be supernovae (type II) and/or Wolf-Rayet stars (Prantzos 1998). Since the half-life of ^{26}Al is only about 10^6 yr, there should have been star burst activities in recent past at the GC region.

High energy cosmic rays with energies of about 10^{18} eV are also found to concentrate in the GC region and the Cygnus region (Hayashida et al. 1999). This result indicates that cosmic rays up to 10^{18} eV, which have been thought to be an extragalactic origin, are also accelerated in our Galaxy or perhaps at the GC region.

2.1.1 Abundance

It has been debatable whether the GC region is overabundant or not. The observations of the Galactic disk SNRs within 3 kpc from the Sun indicate that the abundance gradually becomes larger toward the GC. From the gradient of abundance increase, the abundance of the GC region is estimated to be about 3 times of the solar value (Binette et al. 1982). While, direct observations of the stars in the GC region indicated that the abundance is consistent with the solar value (Carr, Sellgren, & Balachandran 2000). Due to these contradicted results, the abundance of the GC region is not determined.

2.1.2 Magnetic Field

There are many filamentary structures in the GC region: e.g. Radio Arc (section 2.3.3), Sgr C (section 2.3.2). The radio spectra are non-thermal, and thought to be synchrotron emission with the strong magnetic field. By the measurement of the linear polarization, the magnetic field is determined to be mG order, which is much higher than the averaged interstellar magnetic field strength on the Galactic disk of μG order (e.g. Yusef-Zadeh & Morris 1987).

Thus the GC region is peculiar region with various energetic phenomena. Below we introduce the brief characteristics of individual sources.

2.2 The Sgr A Region

Sgr A is resolved into three parts: Sgr A East, Sgr A West, and a point source Sgr A* (Figure 2.1). Sgr A East has shell-like structure, and thought to be a young supernova remnant. Recently, Maeda et al. (2001) detected diffuse X-ray emission from Sgr A East, and verified the hypothesis (also see section 8.1.2). Sgr A West is the shape of spiral, which is surrounding Sgr A*. Sgr A* is a dynamical center of our Galaxy, or Galactic nucleus (see next subsection).

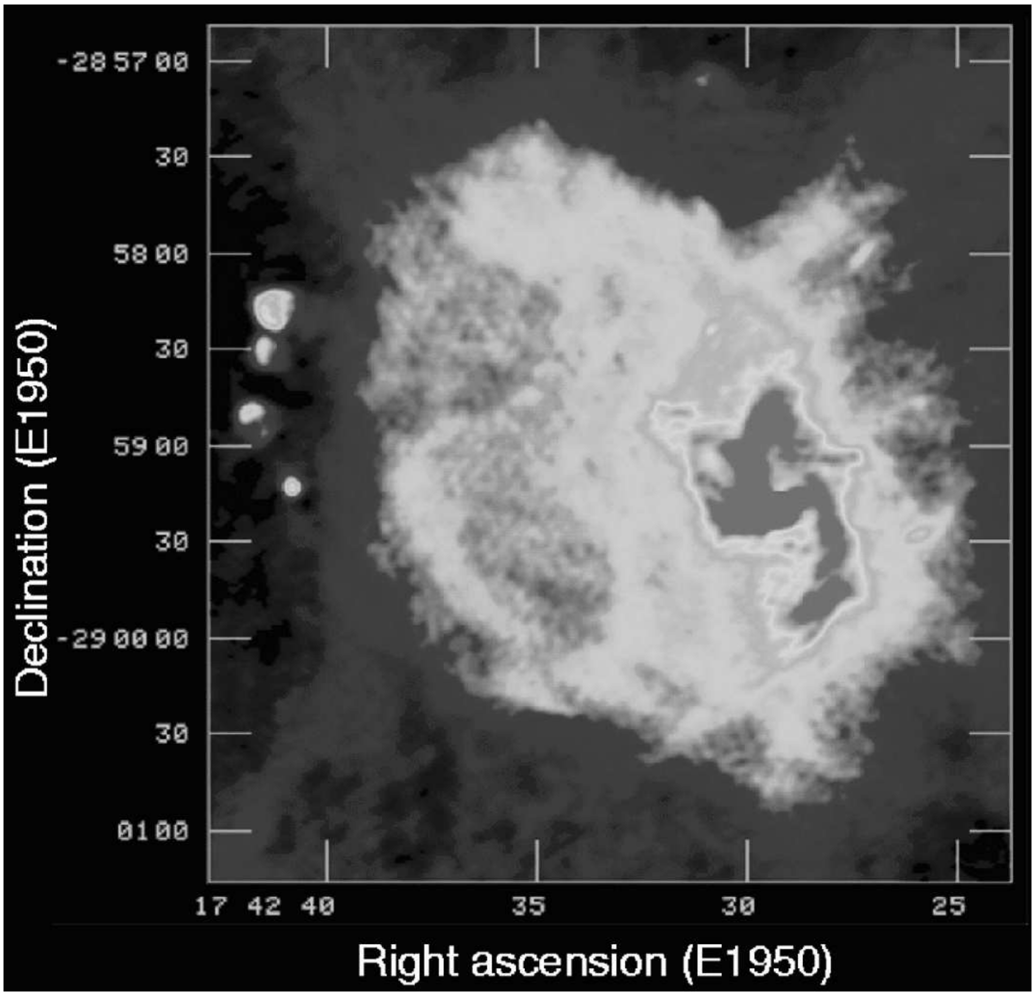

Figure 2.1: VLA radio continuum image of the Sgr A region (Fig. 4 in Yusef-Zadeh, Melia, & Wardle 2000). Shell-like structure Sgr A East (light gray) and the spiral-shaped structure Sgr E West (dark gray) are shown. Note that the coordinates are in equinox 1950.

2.2.1 Galactic Nucleus Sgr A*

Sgr A* was discovered about a quarter of a century ago (Balick & Brown 1974), and is a strong candidate of a massive black hole. Many observations support the presence of the massive black hole. By the observations of the stellar proper motions in the vicinity of the Galactic nucleus Sgr A*, Genzel et al. (1997) revealed a mass of 2.6 $\times 10^6$ $M_\odot$ is confined within about one light-week at Sgr A*. Because there is no stable configuration of normal stars, stellar remnants or substellar entities in such a high concentration of the mass, Sgr A* must be a massive black hole at the Galactic nucleus.

There are many high mass stars around Sgr A*. Based on stellar wind measurements, the gas supply rate is at least $\dot{M} \sim 10^{-6}$ $M_\odot$ yr^{-1} (Genzel et al. 1994). With the standard accretion model, in which the luminosity is calculated to be $\sim 0.1\dot{M}c^2$, the luminosity of Sgr A* should be about 10^{40} erg s^{-1}. However, observed luminosity is several orders smaller than expected value. To solve the contradiction, many theories are presented: e.g. advection-dominated accretion flow (ADAF; Narayan et al. 1998). However, there is no decisive explanation of the quiescent Galactic nucleus. It is one of the most important problems till now.

2.3 The Distribution of Giant Molecular Clouds

In the radio millimeter band, many molecular clouds are found in the GC region. Figure 2.2 shows the global distribution of the molecular clouds in the GC region. These clouds generally exhibit large velocity width of several tens km s^{-1}, and high temperature of 30–60 K. There are some giant molecular clouds: Sgr B2, Sgr C, M0.11$-$0.08 (at the Radio Arc region), and Clump 2.

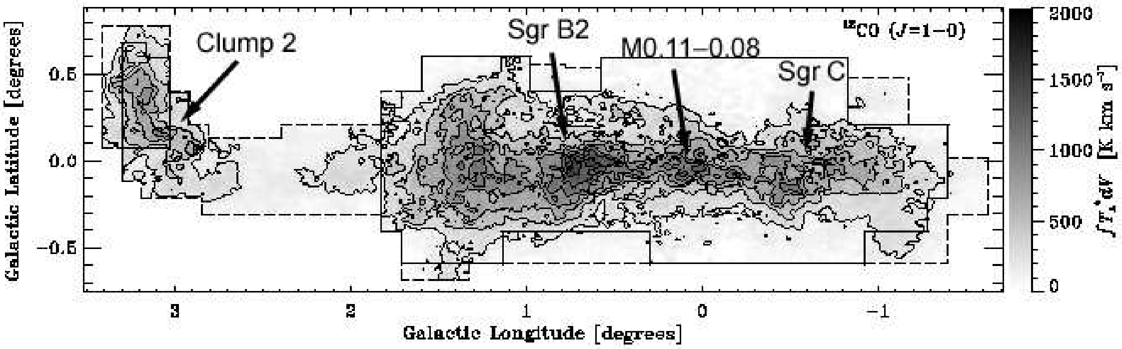

Figure 2.2: The intensity distribution of the ^{12}CO J =1–0 line in the GC region (Oka et al. 1998). The positions of giant molecular clouds are indicated by arrows

2.3.1 Sgr B2

The Sgr B2 cloud is located at $(l, b) \simeq (0\overset{\circ}{.}7,\ 0\overset{\circ}{.}0)$, which is $\sim$ 100 pc from the Sgr A* in the projected distance. The mass of the cloud is estimated to be $\sim$ 6–7 $\times 10^6$ $M_\odot$ with the radio observations of molecular lines (e.g. Oka et al. 1998; Lis & Goldsmith 1989), and one of the most heaviest cloud in the GC region.

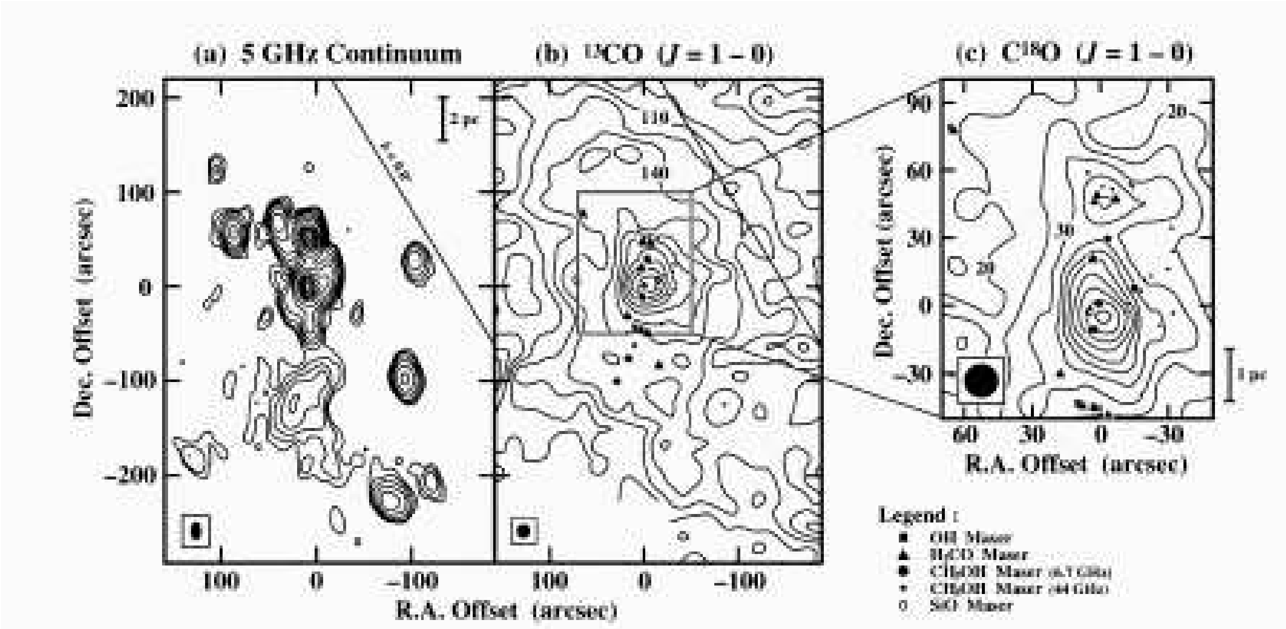

Figure 2.3: Radio images of the Sgr B2 region (Sato et al. 2000). (a) Contour map of the 5 GHz continuum emission imaged with the VLA (J. Whiteoak & F. Gardner 1985, unpublished). The radio peak of Sgr B2 (N), (M), (S) are shown. (b) Contour map of the ^{13}CO emission integrated between $V_{\rm LSR}$ = 35 and 100 km s^{-1}. (c) Contour map of the C^{18}O emission integrated between $V_{\rm LSR}$ = 30 and 100 km s^{-1}. The positions of masers are shown in (b) and (c) (Gaume & Claussen 1990; Mehringer, Goss, & Palmer 1994; Houghton & Whiteoak 1995; Mehringer & Menten 1997; Hasegawa et al. 1985; Morita et al. 1992). The labels are in units of $T_A^* \times \Delta v$ in K km s^{-1}. The coordinates of the maps are relative to $(\alpha,\ \delta)_{1950} = (17^{\rm h}44^{\rm m}10\overset{\rm s}{.}0,\ -18^\circ 22' 00'')$. Half-power beamwidths are shown by a filled ellipse or circle in the lower left-hand corner of each panel.

With the radio observations, there found to be many ultra compact H$_{\rm II}$ regions and masers in the molecular cloud (Benson, & Johnston 1984; De Pree, Goss, & Gaume 1998; Shiki, Ohishi, & Deguchi 1997; Mehringer, Goss, & Palmer 1994). Most of them concentrate in radio continuum peak of Sgr B2 North (N), Main (M), and South (S) (Figure 2.3). The ages of of Sgr B2 (N) and Sgr B2 (M) are estimated to be $\sim 10^4$ years, using the photon flux of the exciting stars and the ambient gas density (De Pree et al. 1995, 1996). In addition, powerful bipolar outflows are found from Sgr B2 (N) and Sgr B2 (M), with the dynamical age of $\sim 10^4$ years (Vogel, Genzel, & Palmer 1987; Lis, et al. 1993; Mehringer 1995; Kuan & Snyder 1996; Liu et al. 1998). All these results indicate that there are many clusters of high-mass young stellar objects (YSOs) in the Sgr B2 cloud.

2.3.2 Sgr C

The prominent objects at the Sgr C region are a shell-like H_{II} region (Sgr C itself) and a filamentary structure perpendicular to the Galactic plane (gray-scale image in Figure 2.4). The filament is non-thermal, and resembles Radio Arc filament (see next section).

There is also a molecular cloud at the Sgr C region as well as these radio continuum structures. In Figure 2.4, ^{13}CO line emission is shown by contours. Near the basis of the filament, and above the H_{II} region, the peak of the cloud is shown (CO 359.4+0.0 in Oka et al. 1998). We call this cloud the Sgr C cloud in this thesis. The mass of the cloud is about $10^6\ M_{\odot}$.

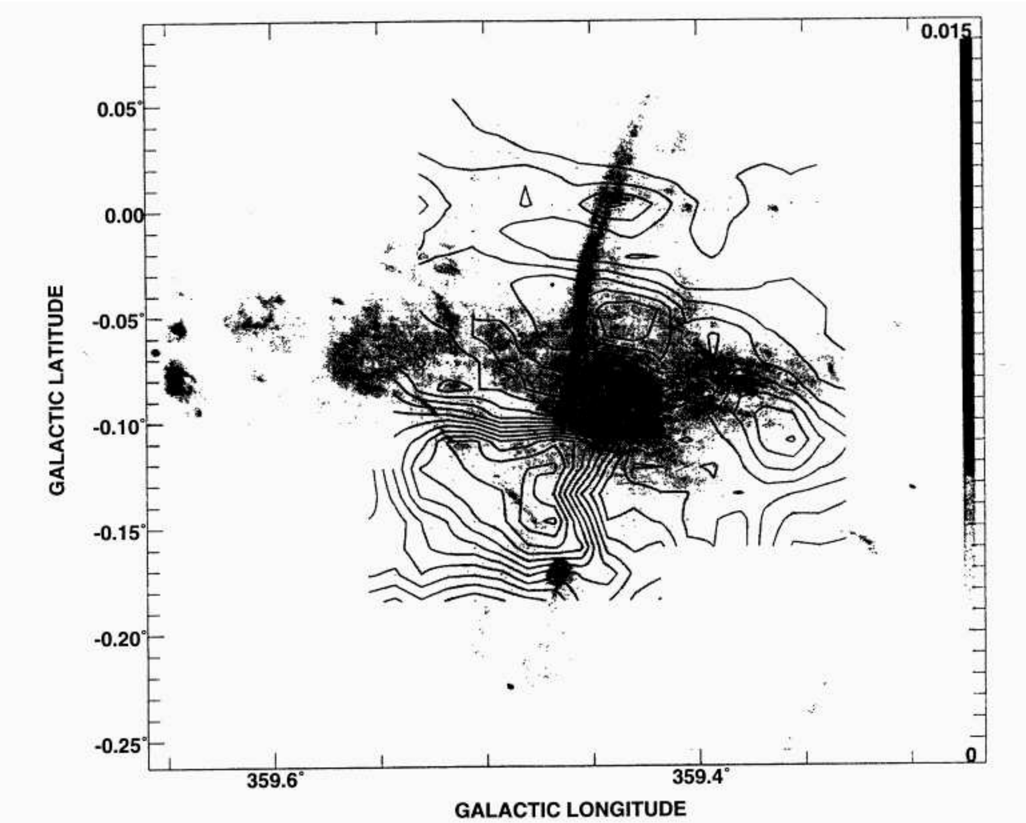

Figure 2.4: Radio image of the Sgr C region. Contours show the ^{13}CO line emission at 10, 20, $\cdots$ 160 K km s $^{-1}$ integrated over the range $-84 \lesssim v \lesssim -24$ km s $^{-1}$. The intensity distribution of 1616 MHz radio continuum emission is superposed with gray scale. (Liszt & Spiker 1995)

2.3.3 Radio Arc

There are notable features of arched filaments and connected straight filaments at the positive-longitude side of the GC (Figure 2.5f). This filed is called the Radio Arc region. The straight filaments are non-thermal, and perpendicular to the Galactic plane with strong linear polarization. The origin of the radio emission is thought to be synchrotron radiation at strong magnetic field.

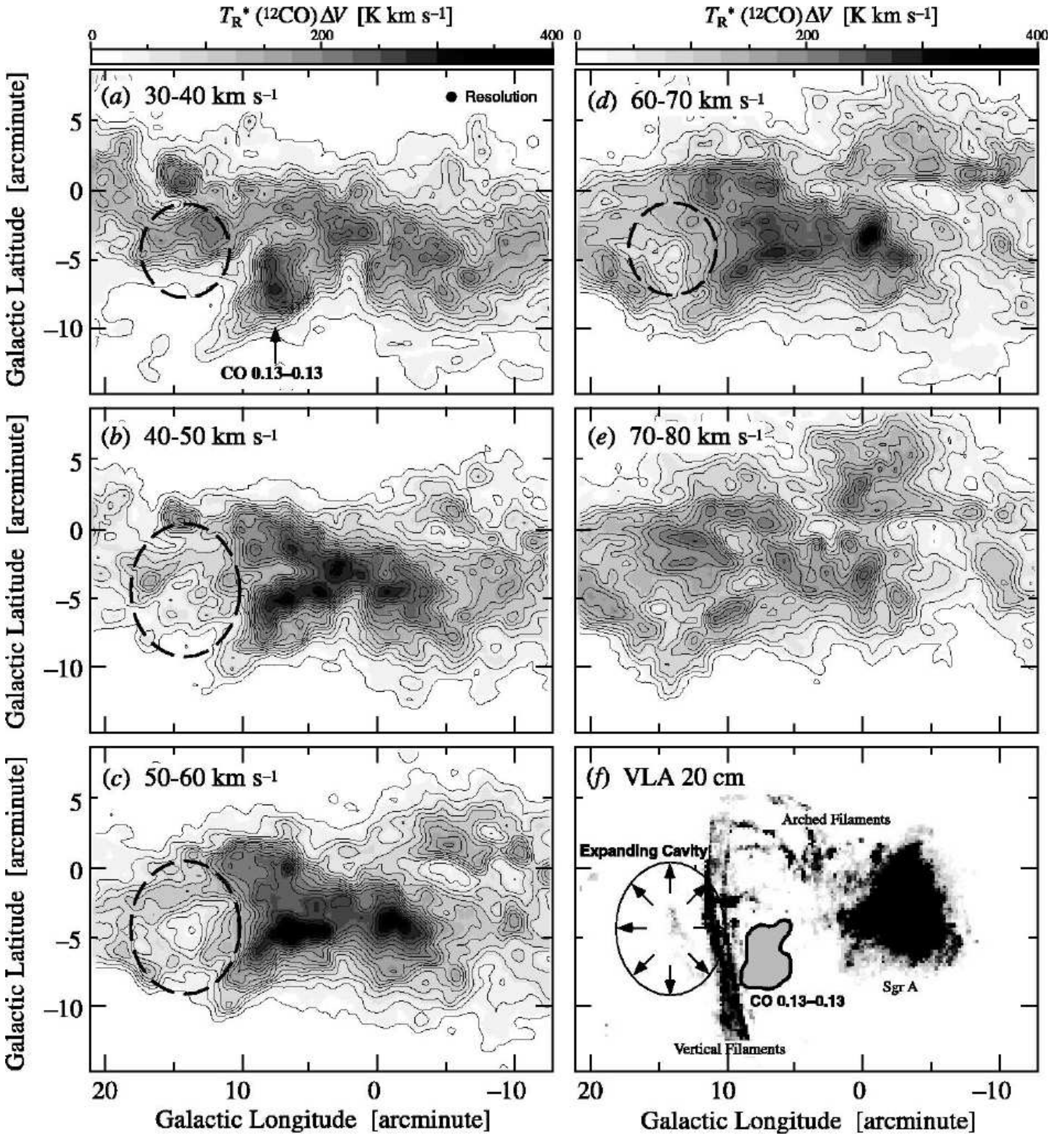

Figure 2.5: The velocity sliced contour maps of ^{12}CO (J =1–0) emissivity (Oka et al. 2001). Contours are drawn at a interval of $\int T_{\rm R}^{*}(V)dV = 20$ K km s^{-1}. The dotted ellipses show a kinematical model for the expanding cavity. (f) A VLA radio continuum image at 20 cm (Yusef-Zadeh et al. 1984) with a schematic view of the molecular features (Oka et al. 2001).

By the observations of radio emission of molecular lines, a molecular cloud is found in the Radio Arc region (M0.11−0.08 in Lindqvist et al. 1995; CO 0.13−0.13 in Oka et al. 2001; see Figure 2.5). The mass of the cloud is estimated to be about 10^6 $M_\odot$ (Oka et al. 2001). Oka et al. (2001) further discovered the expanding cavity at the opposite side of the molecular cloud with respect to the filaments. They suggested that magnetic tubes were swept up by the expanding cavity, and compressed by interacting with the molecular cloud. Then an interaction between the cloud and magnetic field may accelerate electrons to relativistic energies through shock acceleration or magnetic field reconnection.

2.3.4 Clump 2

Clump 2 is a giant molecular cloud located at $(l, b) \simeq (3^\circ, 0.^\circ2)$ found by Bania (1977). As seen in Figure 2.6, the cloud is peculiar with the large velocity width of 50–150 km s^{-1}. The cloud consists of 16 cores, each having densities in excess of $2{\times}10^4$ cm^{-3} (Figure 2.7). The total mass is estimated to be 3×10^6 $M_\odot$ (Stark et al. 1991; Bally et al. 1988).

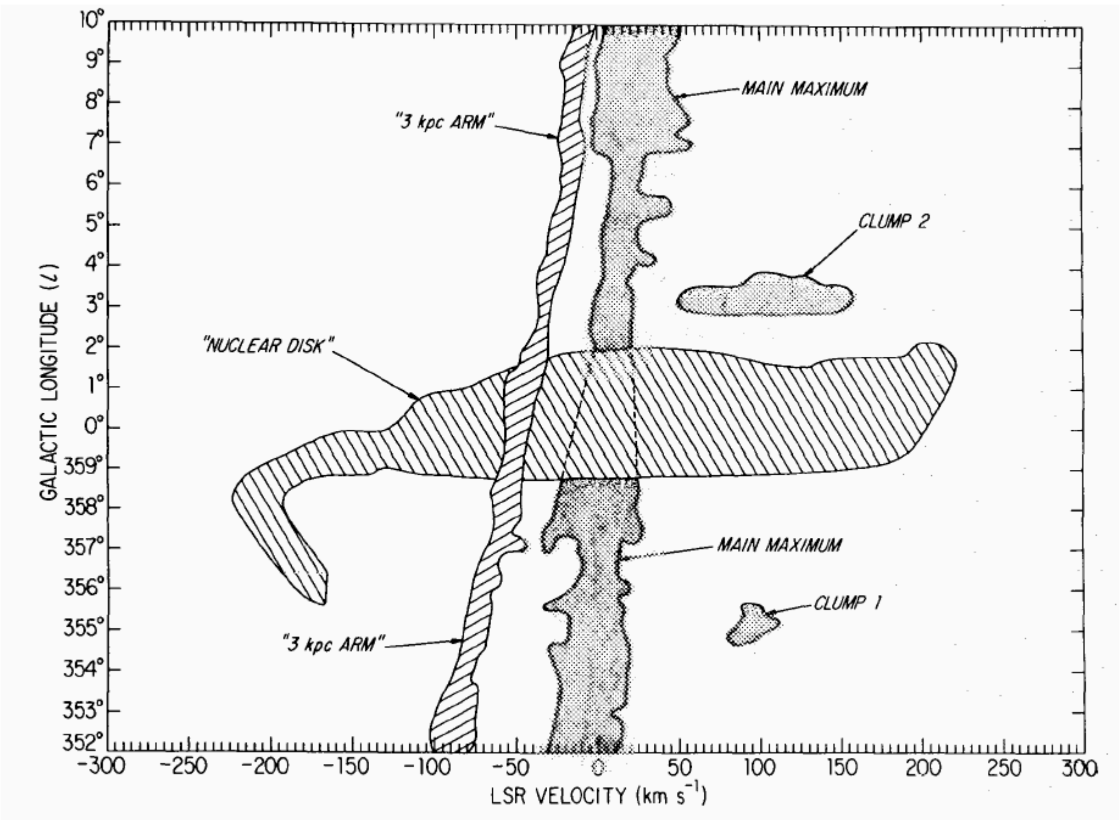

Figure 2.6: Schematic longitude-velocity diagram illustrating the major large-scale kinematic features in the GC region (Bania 1977).

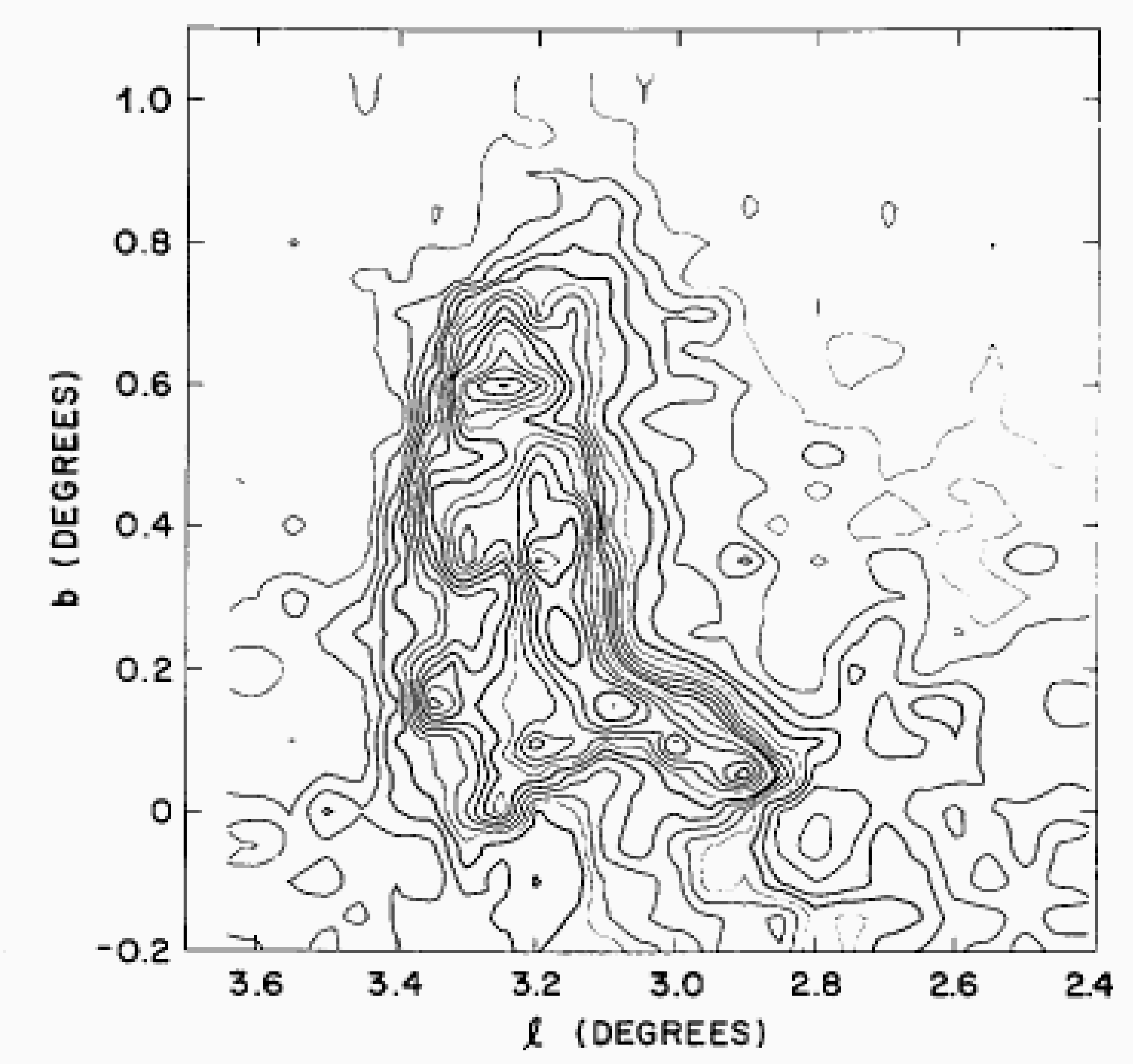

Figure 2.7: Velocity integrated map of ^{12}CO (J =1–0) emission at the Clump 2 (Stark & Bania 1986). The velocity range is from +40 km s^{-1} to +240 km s^{-1}. Contours are drawn at 50 K km s^{-1} interval.

2.4 X-ray Sources in the Galactic Center Region

In X-ray band, some important discoveries are made by Japanese X-ray satellites. Near the end of 1980s, *Ginga* discovered that the central $1^\circ.0 \times 1^\circ.8$ region is filled with the high temperature plasma (Koyama et al. 1989, Yamauchi et al. 1990). Then *ASCA* found the clumpy emissions of neutral iron line (Koyama et al. 1996). The details are mentioned in following sections.

2.4.1 X-ray Luminosity of Sgr A*

As mentioned in section 2.2.1, the most important problem in the Galactic center region is a lack of the activity of the massive black hole Sgr A*. The X-ray emission from the Sgr A region was reported by several X-ray satellites (Skinner et al. 1987; Kawai et al. 1988; Syunyaev et al. 1991) with the intensity variation. However, *ASCA* revealed that the X-ray variability should be attributable to an eclipsing X-ray burster AX J1745.6$-$2901 near Sgr A region (Maeda 1996), and the X-ray emission from the Sgr A region is extended. The upper limit of the X-ray intensity from the Sgr A* is constrained to be $\leq 10^{35}$ erg s^{-1}. *Chandra* resolved Sgr A* for the first time in X-ray band, and the X-ray luminosity is estimated to be 2×10^{33} erg s^{-1} (Baganoff et al. 2001a).

The X-ray luminosity of 2×10^{33} erg s^{-1} is very small for the massive black hole with the mass of $2.6 \times 10^6\ M_\odot$. This value is about 10^{-11} of the Eddington limit.

Recently, *Chandra* detected an X-ray burst from Sgr A* with the luminosity of 10^{35} erg s^{-1} (Baganoff et al. 2001b). However, it is still a small value, which can be radiated by a ordinal neutron star binary.

2.4.2 High Temperature Plasma

Ginga found strong emission of highly ionized iron line from the GC region (Koyama et al. 1989). Since the ionized line emission is typical of the optically thin plasma, the discovery of the iron line indicated the presence of a large amount of high temperature gas at the GC region. The temperature is estimated to be about 10 keV. Then Yamauchi et al. (1990) investigated the distribution of the iron line, and revealed that the plasma is an elliptical structure with the size of $1^\circ.8 \times 1^\circ.0$ (FWHM), which is tilted $21^\circ \pm 3^\circ$ with respect to the Galactic plane (Figure 2.8). The total energy and the total luminosity of the plasma are (4–8) $\times 10^{53}$ erg and (0.9–3) $\times 10^{37}$ erg s^{-1} in the 2–10 keV band, respectively. Note that such high temperature plasma cannot be confined with the gravity of the GC region. The typical time scale of the plasma (obtained by dividing its diameter by the sound velocity) is $\sim$ 50000 yr. Later observation with the higher energy resolution of *ASCA* revealed that the line width of the iron line is slightly broad with the σ of $\sim$ 75 eV (Koyama et al. 1996).

Following the discovery of the $1^\circ\!.8 \times 1^\circ\!.0$ plasma with*Ginga*, *ASCA* found another high temperature plasma at the close vicinity of Sgr A* by the higher angular resolution than *Ginga*. The size and the total energy are $\sim 2' \times 3'$ and 3 $\times 10^{50}$ erg, respectively. Recently, with the much higher angular resolution of *Chandra* ($\sim 0''\!.5$), the plasma was found to fill the radio shell structure, Sgr A East. Maeda et al. (2001) suggested that supernova explosion about 10000 yr ago might produce the plasm. However, the origin of the larger scale plasma is an open question till now.

2.4.3 Neutral Iron Line

ASCA resolved iron lines from the GC region to three characteristic emission lines from the atoms in respective ionized states; 6.4-keV line from neutral iron, 6.7-keV line from He-like iron, and 6.9-keV line from H-like iron. 6.7-keV and 6.9-keV lines should be attributable to the high temperature plasma in the GC region, but 6.4-keV line can not be radiated by the plasma.

The distribution of the 6.4-keV iron line is shown in Figure 2.9 (Koyama et al. 1996). There are two distinct peaks at the Sgr B2 region and the Radio Arc region, which roughly agree with the position of the giant molecular clouds. In addition, Martín-Pintado et al. (2000) found the correlation between the 6.4-keV line emission and the SiO (J = 1–0) line intensity. Because 6.4-keV line is a characteristic radiation from neutral irons, it is natural to think that X-rays are emitted by molecular clouds. However, clouds are very cold, and can not emit high energy X-rays in themselves. Koyama et al. (1996) implied that clouds are irradiated by an external X-rays, and emit fluorescent X-rays as 6.4-keV line. It is the most important theme in this thesis to reveal the origin and the radiation mechanism of the 6.4-keV line.

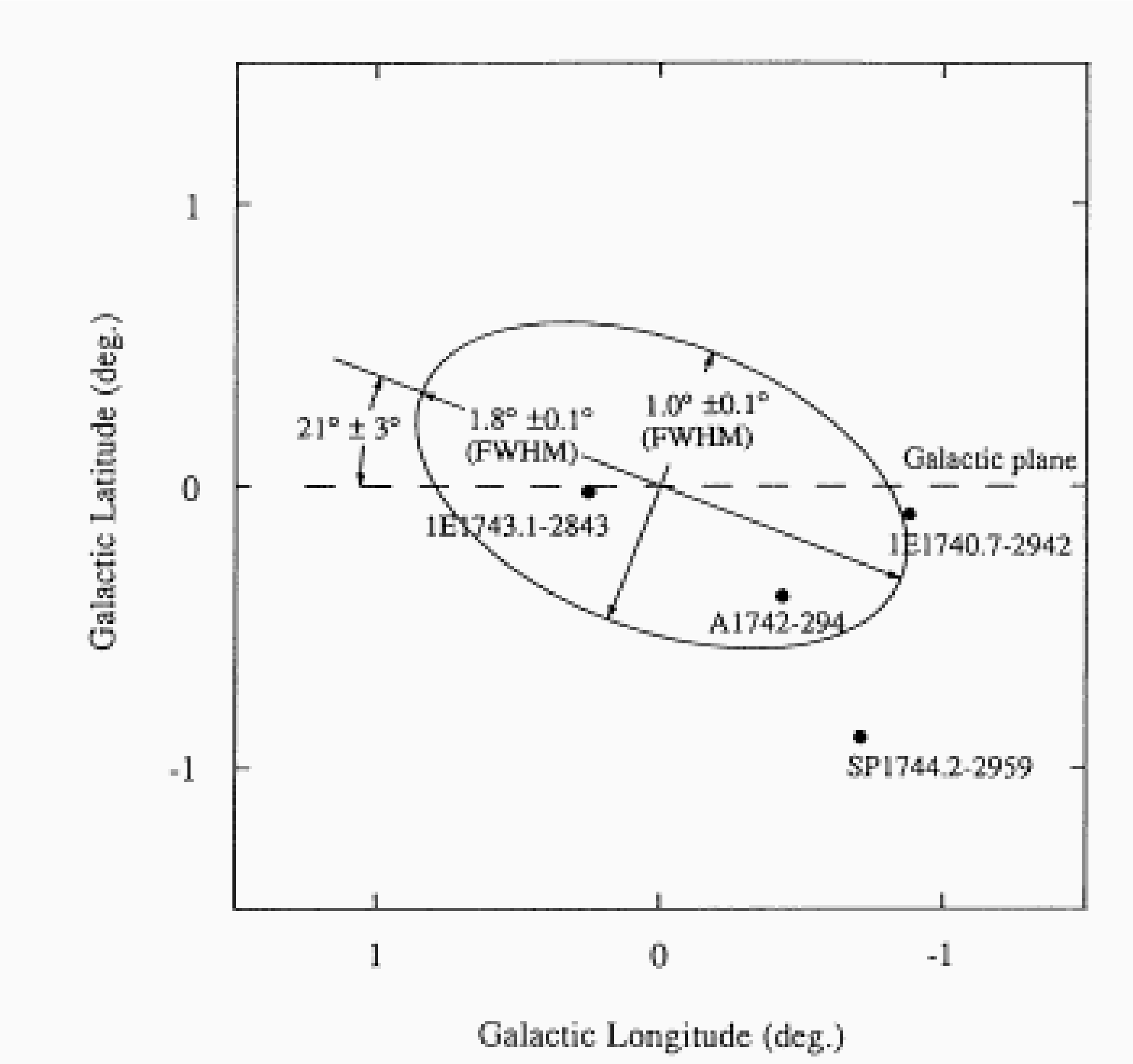

Figure 2.8: The schematic distribution of the GC plasma obtained with *Ginga* (Yamauchi et al. 1990)

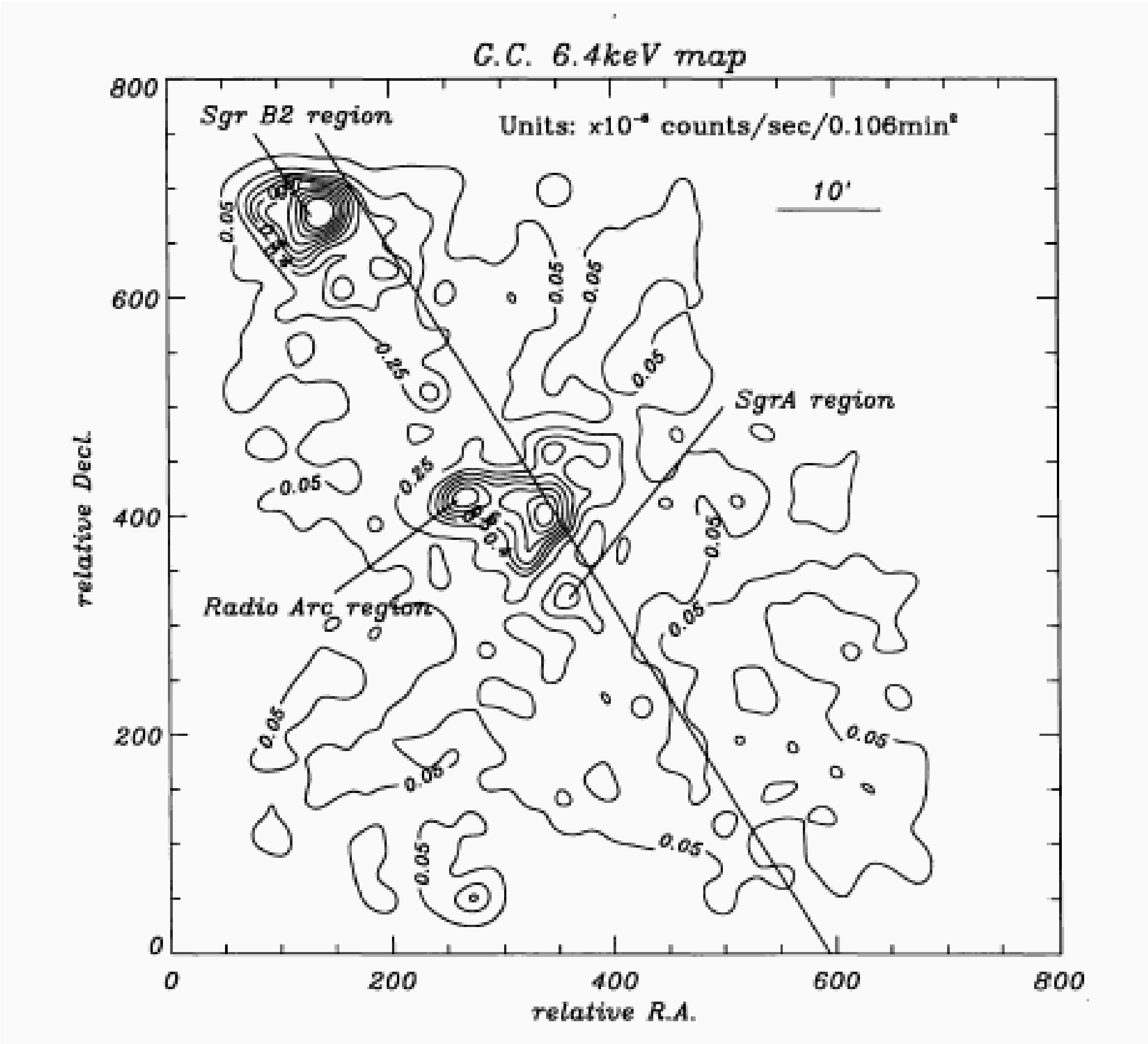

Figure 2.9: The distribution of the 6.4-keV line intensity in the GC region.

Chapter 3

Instruments

We use the *ASCA* and the *Chandra* data in this thesis. In this chapter, we introduce the properties of both satellites.

3.1 *ASCA*

3.1.1 Overview

ASCA was the fourth Japanese astronomical X-ray satellite, which was launched into orbit on February 20, 1993 (Tanaka et al. 1994). The orbital heights at perigee and apogee were about 520 km and 620 km, respectively, whereas the inclination was $31.^\circ1$. The orbital period was approximately 96 minutes. The satellite have been reentry into the atmosphere on March 2, 2000.

ASCA was the first satellite which can obtain X-ray images in hard X-ray band above 2 keV (to 10 keV). The X-Ray Telescopes (XRTs) enable to gather high energy X-rays with the large number of thin-foil layers. *ASCA* was equipped with two sets of the Gas Imaging Spectrometers (GISs) and the Solid-state Imaging Spectrometers (SISs) at the foci of four identical XRTs. Figure 3.1 shows the appearance and the schematic configuration of instruments aboard *ASCA*.

3.1.2 Attitude Control System

The satellite attitude was controlled with four reaction wheels (RW) and three-axis magnetic torquers (MTQ). RWs exchange the angular momentum with the satellite to control the attitude, and MTQs are used to adjust the total angular momentum by interacting with an external magnetic force. As an attitude sensor, *ASCA* had five inertial reference units (IRUs),

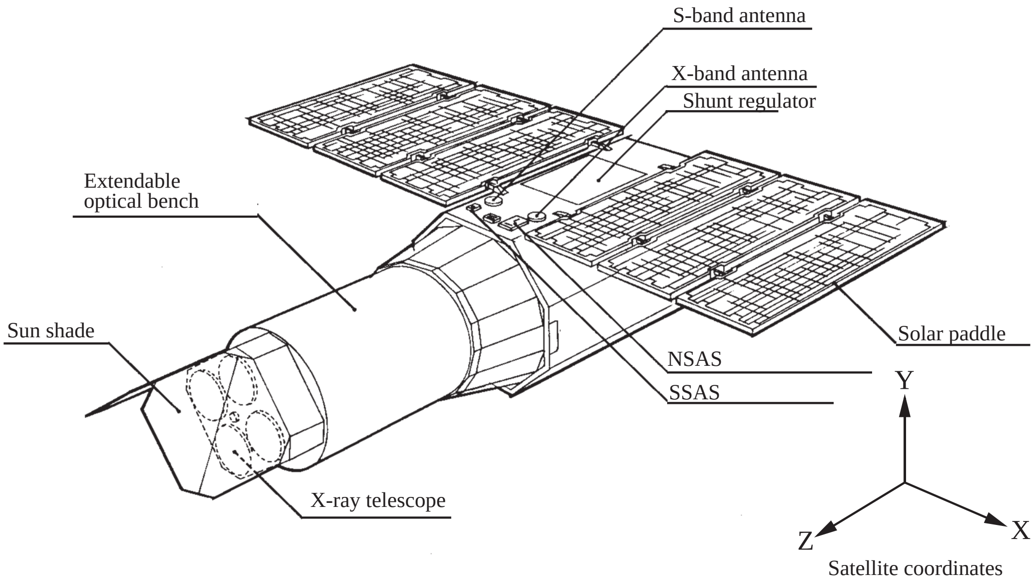

(a) The appearance of the *ASCA* satellite

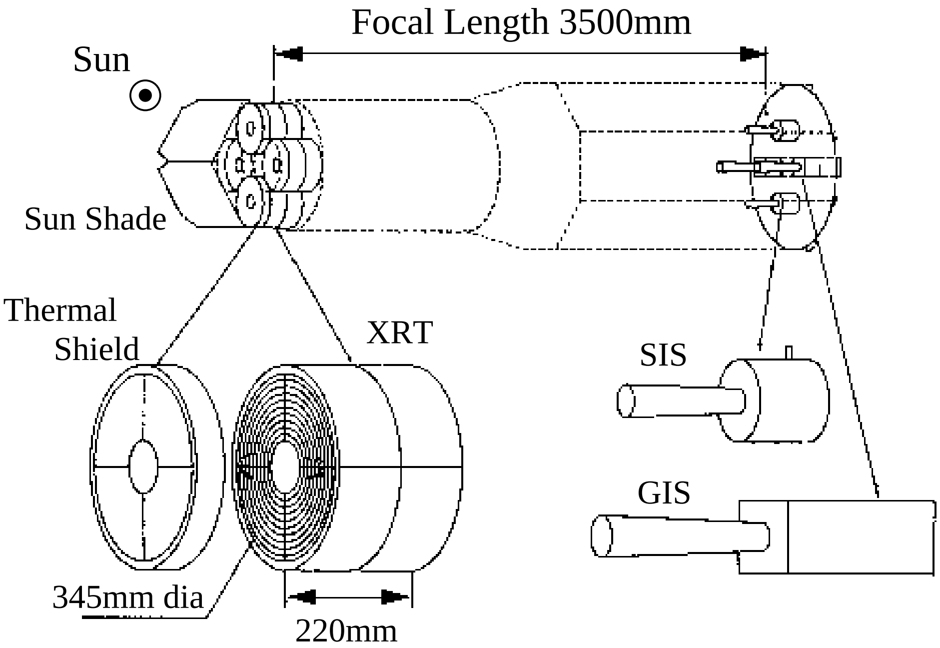

(b) The configuration Φ of XRTs and the detectors aboard *ASCA*

Figure 3.1: The schematic images of the *ASCA* satellite. (a) The appearance of the satellite. There is four XRTs pointing to the lower left. (b) Configuration of XRTs and the detectors aboard *ASCA*. The XRTs are pointing to the left. Two GISs and two SISs are located at the focal plane.

two star trackers (STTs; optical CCD camera), one non-spinning solar aspect sensor (NSAS), one spinning solar aspect sensor (SSAS), and 3-axis geomagnetic aspect sensors (GAS). IRUs monitor the relative change of the attitude, whereas STTs are used to determine the absolute attitude of the satellite. The stability of the attitude was normally better than $10''$, whereas the absolute pointing accuracy was $\simeq 40''$[1] (Gotthelf 1996), except just after maneuver. The accuracy can be improved by correction

3.1.3 XRT (X-Ray Telescope)

The *ASCA* telescopes are configured according to the Wolter type-1 system: concentric parabola and hyperbola. The four X-ray telescopes aboard *ASCA* are identical. The mirrors are formed by a large number of thin-foils (120 foils) with the diameters from 120 mm to 345 mm, and the focal length of 3.5 m. On the focal plane, 1 mm corresponds to 0.9822 arcmin. Each of XRTs consists of four identical quarter mirrors, called quadrants.

Figure 3.2a shows the effective area of XRT in relation to an X-ray energy. In general, the effective area becomes smaller with the higher energy X-rays: about 300 cm^2 below 2.0 keV, and 200 cm^2 at 5.0 keV. The effective area also decrease with the larger off-axis angles[2] (Figure 3.2b). At the off-axis angle of $20'$, the effective area becomes 1/4–1/5 of on-axis value.

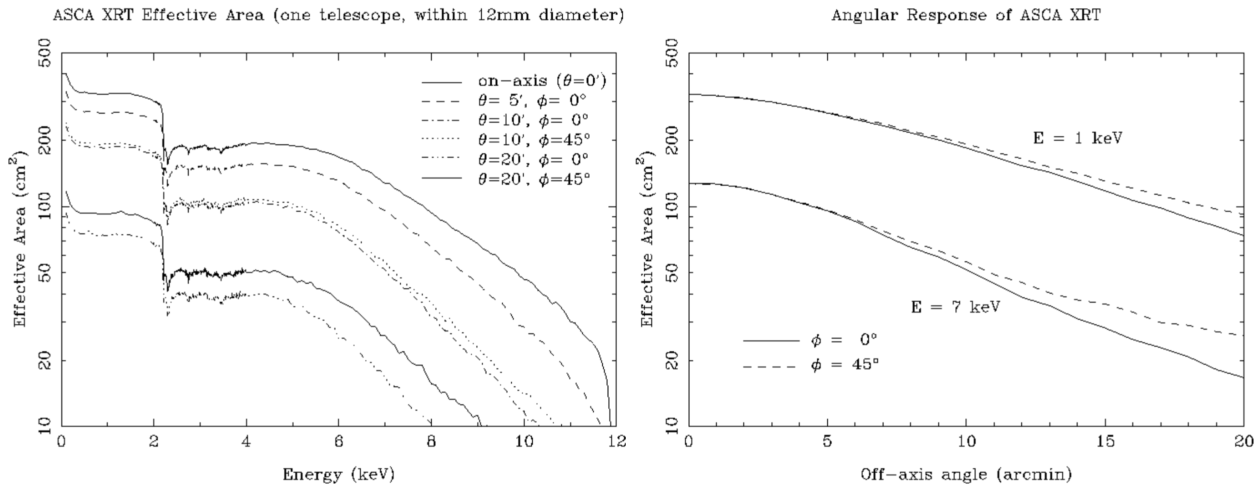

(a) Effective area vs. X-ray energy (b) Effective area vs. off-axis angle

Figure 3.2: Energy and position dependence of *ASCA* XRT effective area.

A point source image, which is called Point Spread Function (PSF), is shown in Figure 3.3.

[1]The accuracy can be improved to $\simeq 24''$ for GIS by correcting temperature dependent deviation of the attitude (Gotthelf 2000)

[2]This dependence of effective area on incident angle is called vignetting.

Since XRTs are made with 4 parts of quadrants, the image seems to be a so-called 4-leaves pattern. The 4-leaves image becomes flatter in larger off-axis angle.

A useful parameter for representing the performance of the mirror is "encircled energy function" shown in Figure 3.4. This function shows how many photons are included in a circular region of each diameter with the point spread function of mirrors. When we observe a point source, about a half of X-rays are gathered in $3'$-diameter region, and 80% of X-rays are in $6'$-diameter.

X-ray photons are designed to reflect twice on the surface of the mirror with the Wolter type-1 system, but some of X-ray photons from out of the field of view (FOV) reach the focal plane through incorrect paths (Figure 3.5). These photons are called stray light. The intensity of stray light depends on the spectral shape of the source, as well as the source intensity and structure, because softer photons are more easily reflected with large angle than harder photons.

The stray light does not focus on the focal plane as the usual image, but produces a diffuse image; for example, the stray light from a point source out of FOV makes a shell-like structure depending on the source offset distance and the angle. Fig. 3.6 shows the observed stray light structures on the GIS detector, where the stray light source is Crab. The stray light from largely extended sources like the cosmic X-ray background, on the other hand, produces no distinct structure, but smooth extended structure over the focal plane, because of the large solid angles.

Details for XRTs are found in Serlemitsos et al. (1995).

3.1.4 GIS (Gas Imaging Spectrometer)

The Gas Imaging Spectrometer (GIS) is an imaging gas scintillation proportional counter (Ohashi et al. 1996; Makishima et al. 1996). *ASCA* has two GISs called GIS2 and GIS3, which are operated in parallel. Fig. 3.7 shows the schematic diagram of the principle of photon detection with GIS. GISs are superior to SISs in following points: a wide FOV with radius of $\sim$25 mm ($\sim 25'$), good time resolution, high detection efficiency in high energy band, and a little degradation for years in orbit.

GIS has sensitivity from 0.7 to 15 keV, whereas the nominal energy range is actually limited below 10 keV, due to lack of sensitivity with XRT above 10 keV. Although GIS has three observational modes: PH, PCAL and MPC modes, we here concentrate on the performance in only the PH mode because all of the observations that we use in this thesis were operated with PH mode.

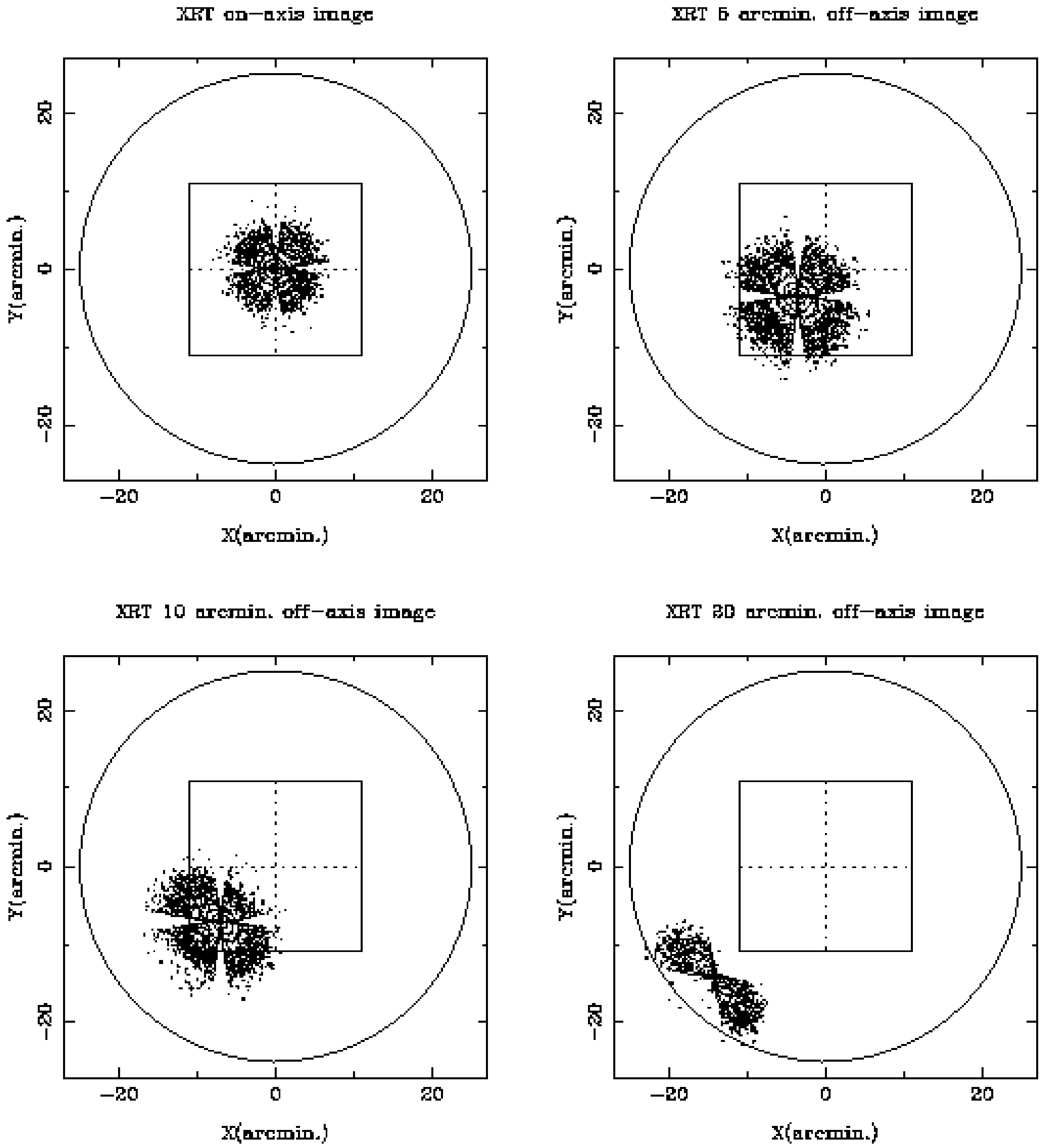

Figure 3.3: Point spread functions of *ASCA* XRT at four different off-axis angles. Circle and square shows the field of view for GIS and SIS, respectively.

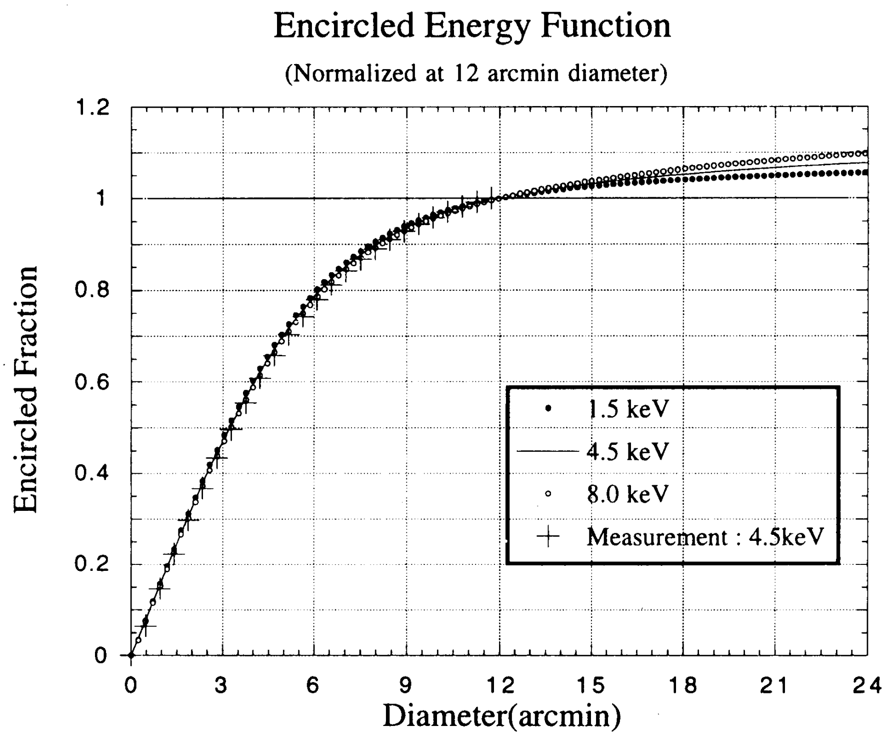

Figure 3.4: The encircled energy functions of the XRT, which are normalized at 12′.

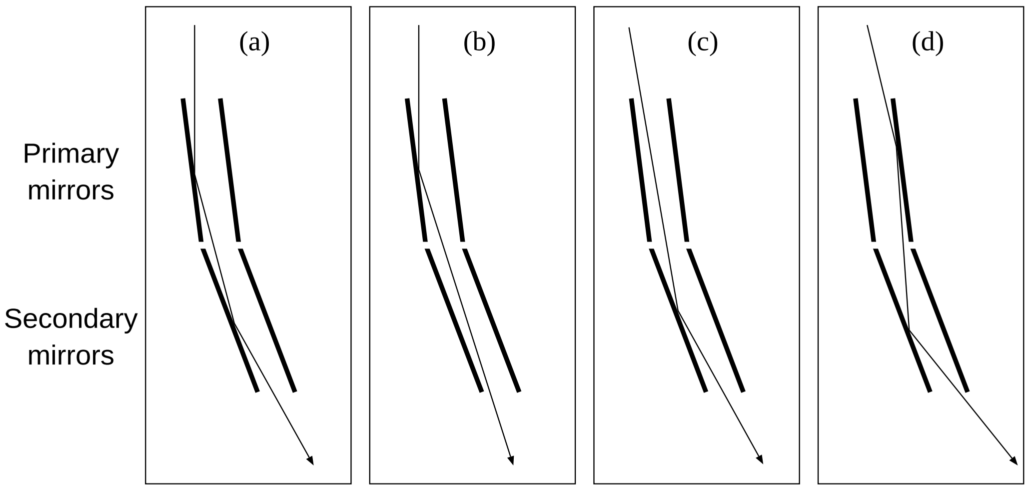

Figure 3.5: Schematic views for incorrect light paths with the stray light photons: (a) normal path, (b) reflection only by primary mirrors, and (c) only by secondly mirrors, (d) reflection by back surface of mirrors (Ishisaki 1997).

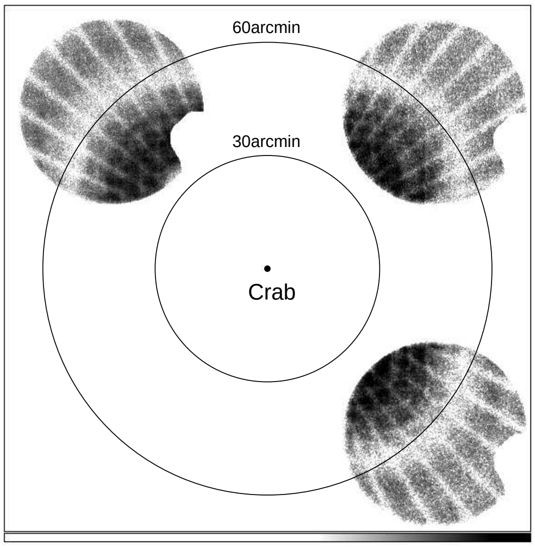

Figure 3.6: Observed stray light structures due to Crab taken with GIS (Ishisaki 1997).

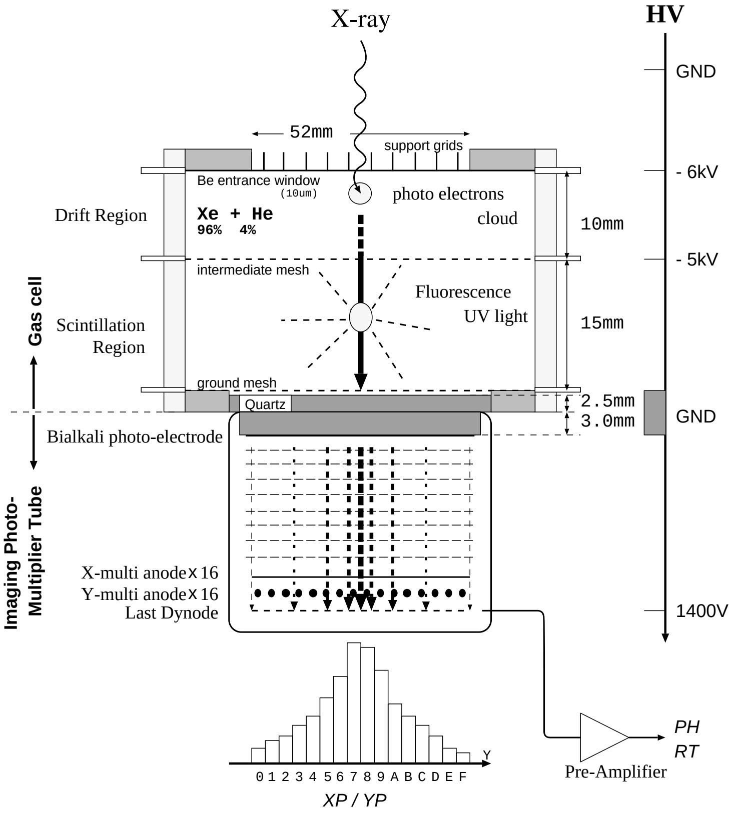

Figure 3.7: Schematic diagram of the principle of the GIS detector.

GIS achieves low background count rate with effective discriminations of non-X-ray events with pulse height, rise time, spread of light, and the position information. Most of non-X-ray events are rejected in orbit, whereas some of them are rejected in the data analysis at ground[3]. Fig. 3.8 shows the GIS spectra of day earth[4], blank sky[5] and night earth[6]. The night earth data (image and spectrum) are thought to represent the non-X-ray events.

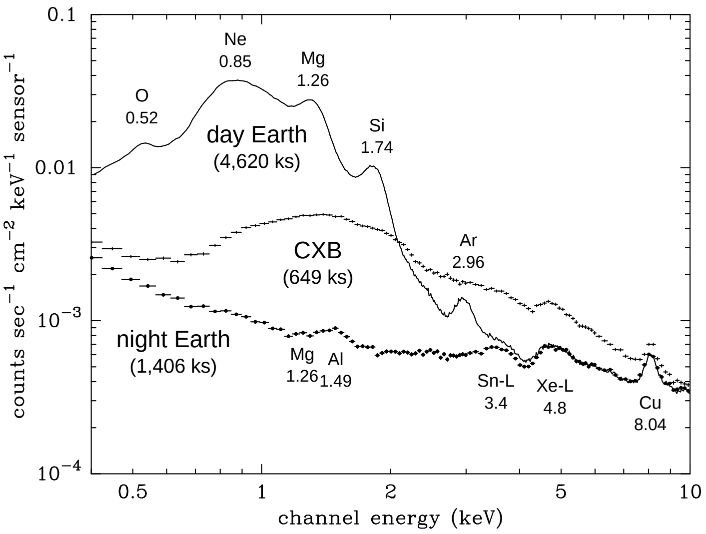

Figure 3.8: GIS spectra of day earth, blank sky and night earth (Ishisaki 1997).

The long-term monitoring of the night earth data shows that the GIS non-X-ray background (NXB) has been gradually increasing since the launch, whereas the spectral shape has not changed significantly (Ishisaki et al. 1997; see also Fig. 3.9). The reason is still not clear, although it is generally thought to be caused by a gradual build-up of long-term decay radioisotopes.

The bit assignment for the GIS telemetry data represents the quantity of information on (sensor-ID), pulse height, X-ray detected position for X- and Y-axes, rise time information, spread of light, and time stamp for each event. The standard bit assignment, with which most of the observations are done, are (1-)10-8-8-5-0-0 for the above items, respectively; it means that pulse height information is expressed with 10 bits, namely 1024 ch, and the X-axis information

[3]Sometimes the important data (especially, rise time information) to reject the non-X-ray events are not included in the telemetry data, depending of the selected GIS bit assignment; in that case, the rejection of non-X-ray events at ground is not so effective.

[4]The earth surface which is illuminated by the sun (at day).

[5]The high Galactic latitude fields where no bright X-ray sources are seen.

[6]The same as day earth, but at night.

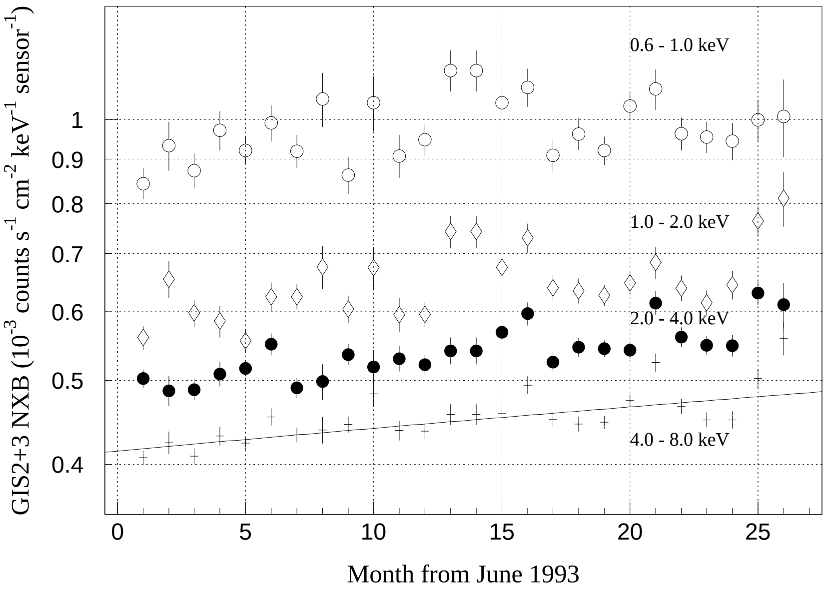

Figure 3.9: Change of GIS NXB fluxes with several energy bands since the launch (Ishisaki 1997) NXB shows gradual increase since the launch.

is expressed with 8 bits, namely 256 ch, for example. For the standard bit assignment, 1 ch for X- or Y-axis corresponds to 0.250 mm, and 1 ch for pulse height corresponds to $\sim$0.012 keV.

The time resolution of GIS depends on bit-rate and GIS bit assignment that the observer selects. In high bit-rate, the best time resolution is achieved, whereas in medium and low bit-rates, the resolution is worse by a factor of 8 and 32, respectively, than that in high bit-rate. For standard bit assignment, the time resolution in high bit-rate is 65 msec. We can increase the time resolution by changing the bit assignment, sacrificing other information, such as, rise time information.

The energy gain of GIS is the function of the temperature, the detected position, and the time from launch, etc. Each of GIS sensor (GIS2 and GIS3) is equipped with the isotope ^{55}Fe at the edge of the sensor; we can refer the peak of the spectrum of the calibration isotope to correct the gain. Thus we correct the raw gain to the linear scale one.

Details for GIS are found in Ohashi et al. (1996), Makishima et al. (1996).

3.1.5 SIS (Solid-state Imaging Spectrometer)

The Solid-state Imaging Spectrometer (SIS) is an X-ray CCD camera (Burke et al. 1991, 1994; Yamashita et al. 1997; Yamashita 1998). *ASCA* has two SISs called SIS0 and SIS1, which are operated in parallel. SISs exhibit better energy resolution (130 keV at 5.9 keV, at launch), higher detection efficiency in low energy band, higher rejection rate of the particle events, and better spatial resolution[7] than GISs.

Each of SISs has 4 chips, each of which has 420×422 pixel with a pixel size of 27 μm. Geometrical area of each chip is 11 mm×11 mm, corresponding to about $11' \times 11'$. All of the SIS chips can be operated in parallel, although only the selected chips are used in most of the observations to avoid telemetry saturation. The energy range of SIS is from 0.4 to 10 keV. Although many kinds of operation modes for SIS are available, we used only the Faint and the Bright modes in the observations of the GC region (see Burke et al. 1991, 1994). Hence we here concentrate on these two modes.

The time resolution of SIS is 4, 8, or 16 seconds, depending on how many chips are used for the observation. The events detected with SIS are often extended for two or more than two pixels. We classify the shape of extension into eight categories (Grade 0–7: Fig. 3.11). Nominally we regard Grade 0, 2, 3 and 4 events as X-ray events, whereas we regard others as non-X-ray events.

The SISs are known to have the serious degradation since the launch due to the accumulated radiation damage (Dotani et al. 1997; Yamashita et al. 1997; Yamashita 1998). It makes the large calibration uncertainty as well as the degradation of energy resolution, the detection efficiency, and the increase of the hot/flickering pixels.

[7] The pixel size of SIS, 27μm, corresponding to $0.'027$, is the angular resolution of SIS, whereas the half power diameter of XRTs is $3'$.

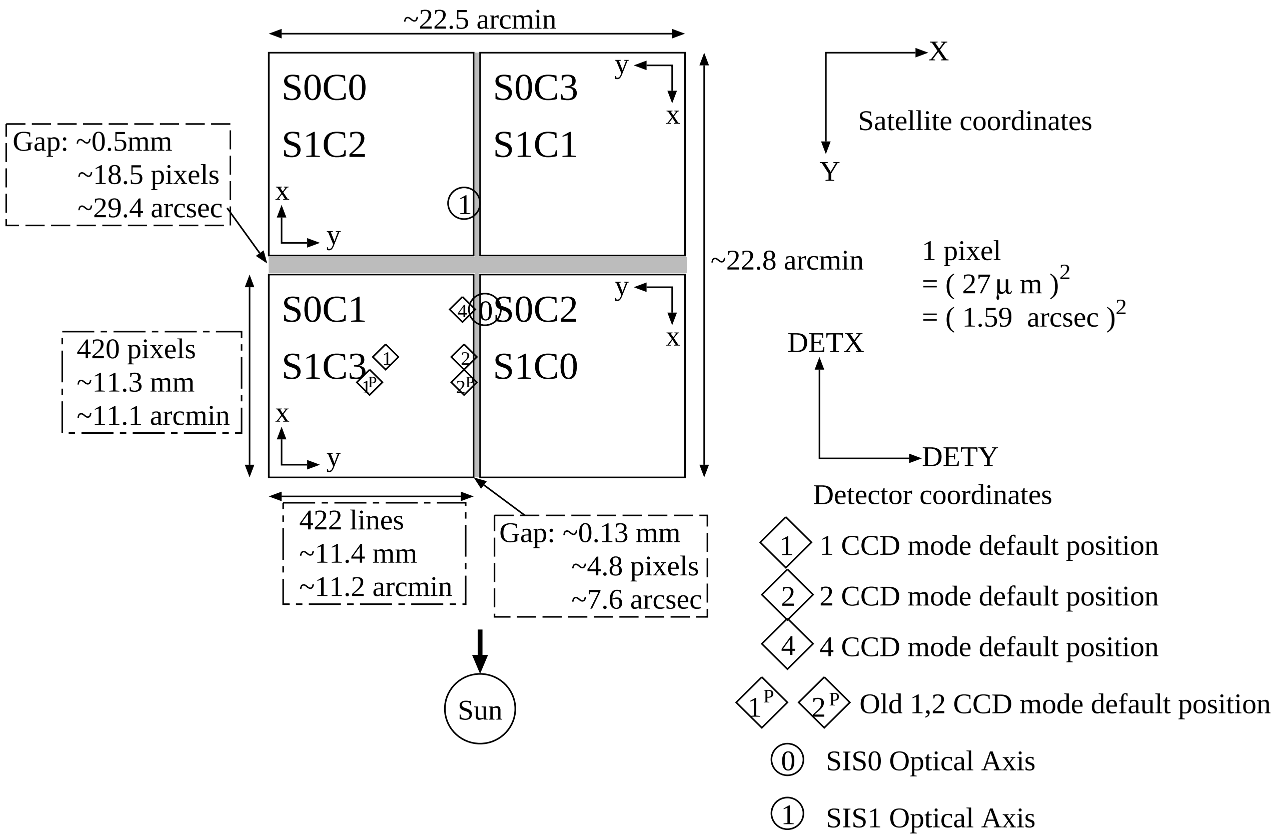

Figure 3.10: The layout of the SIS chips.

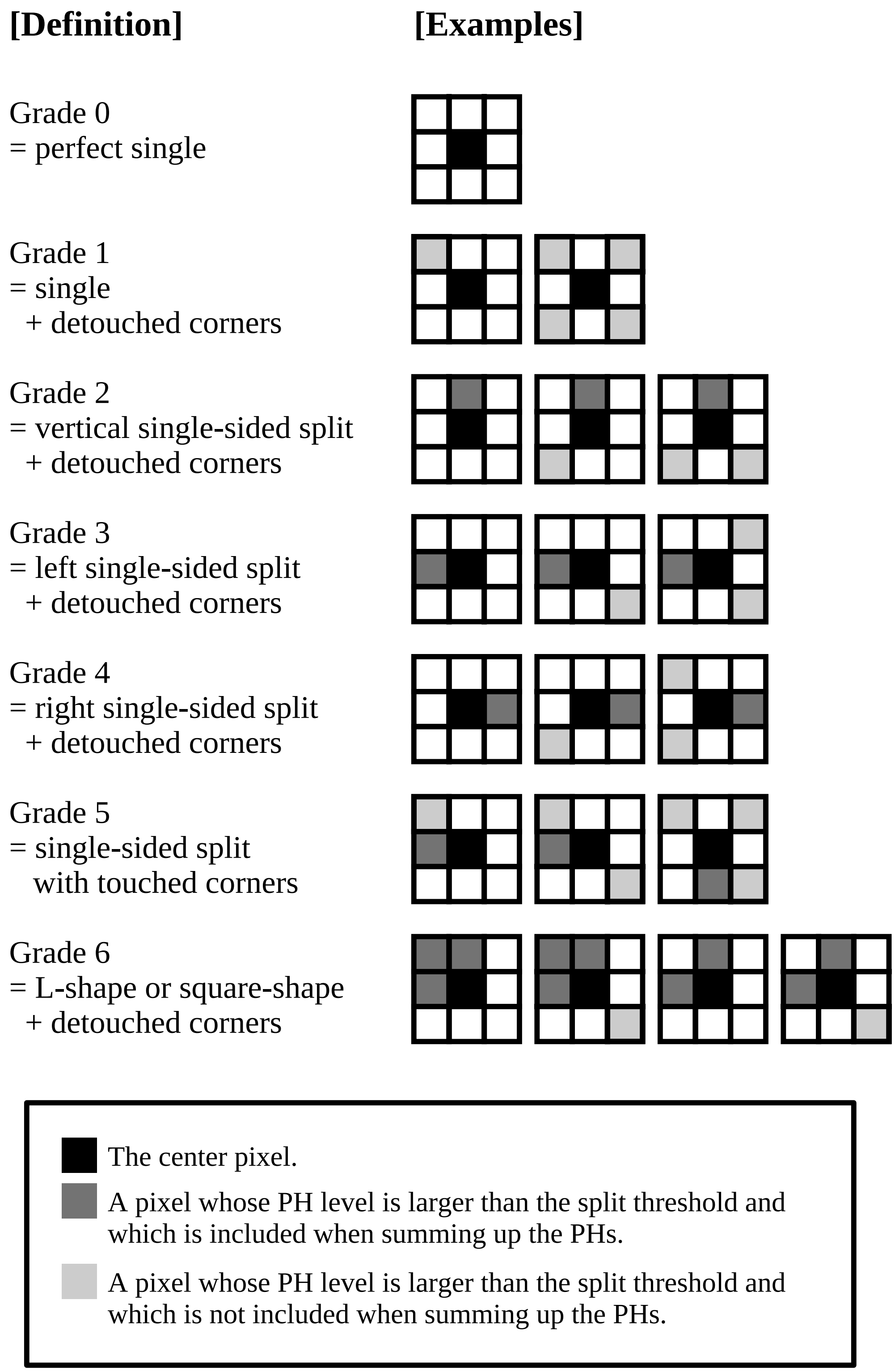

Figure 3.11: Grade definition and the rule to add pulse heights. The events out of these criteria are defined as Grade 7.

3.2 *Chandra*

In this section, we introduce the property of the *Chandra* satellite. The large portion of descriptions, figures, and tables are referred to the *Chandra* Observatory Guide v.3 (`http://asc.harvard.edu/udocs/docs/docs.html`).

3.2.1 Overview

Chandra was launched on the Space Shuttle Columbia on July 23, 1999. The orbit of the satellite is elliptical with the perigee altitude of 10,000 km, the apogee altitude of 140,000 km. The orbital period is about 64 hours, which is allowing uninterrupted observing intervals of more than 48 hours.

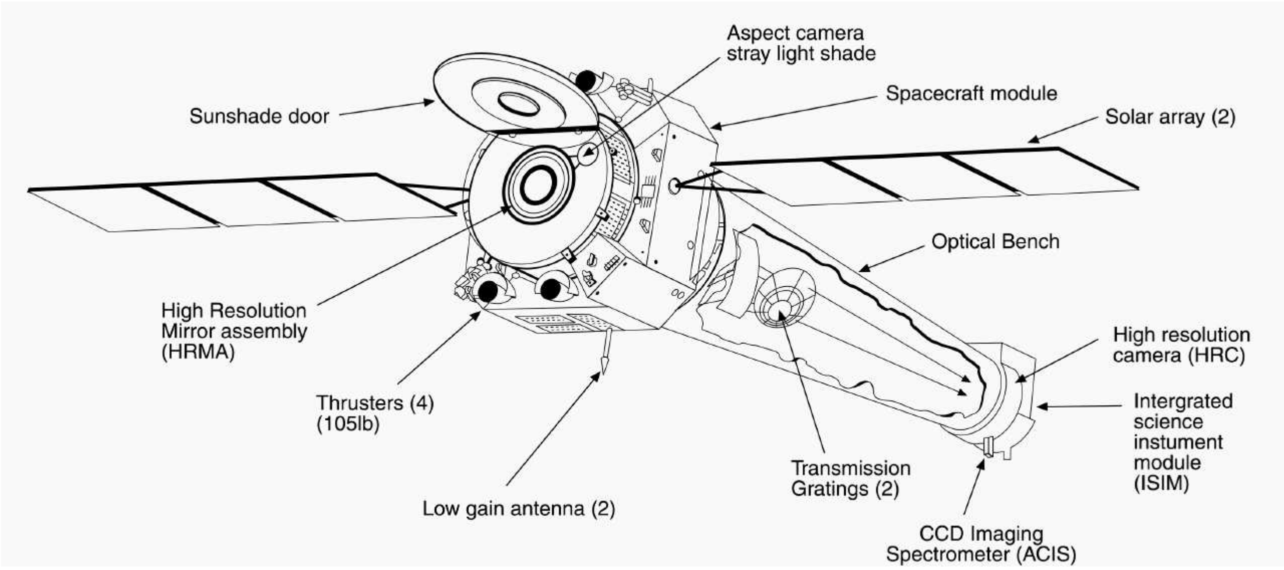

Figure 3.12: The schematic view of the *Chandra* satellite

The most vivid characteristic of *Chandra* is higher angular resolution than all the previous X-ray satellites. The *Chandra* telescope, "High Resolution Mirror Assembly (HRMA)", consists of 4 mirrors of Wolter type 1 geometry formed by glass, and achieved the angular resolution of $0\farcs5$. The satellite attitude is controlled and determined by "Pointing Control and Aspect Determination (PCAD)" system with the higher accuracy than angular resolution.

Chandra has two focal plane instruments: a microchannel plate, named "High Resolution Camera (HRC)", and a X-ray CCD camera, "Advanced CCD Imaging Spectrometer (ACIS)". *Chandra* also has two gratings: "High-Energy Transmission Grating (HETG)", and "Low-Energy Transmission Grating". To protect the instruments from the particle radiation damage, *Chandra* is equipped with a charged-particle detector, the "Electron, Proton, Helium INstrument (EPHIN)". The schematic view of the satellites is shown in Figure 3.12. The detailed properties of the instruments are mentioned in following subsections.

3.2.2 PCAD (Pointing Control and Aspect Determination) System

Aspect control

The satellite attitude is controlled by the Reaction Wheel Assembly (RWA). Six wheels are mounted in a pyramidal configuration, and adjust the angular momentum. To unload accumulated momentum by external torques (e.g. gravity gradient, magnetic force), thrusters are used, which is named the Momentum Unloading Propulsion System (MUPS). Reaction Control System (RCS) also consists of thrusters which change the spacecraft attitude in powered flight, RCS maneuver, and RCS safe sun modes. PCAD modes and concerned instruments used in each mode is summarized in Table 3.1.

Table 3.1: PCAD Modes and Concerned Instruments Used in each Mode

Mode	Sensors	Control	Description
Standby	—	—	On-board computer commands to RWA, RCS, and Solar Array Drive Assembly (SADA) disabled, for initial deployment, subsystem checkout, etc.
Normal Pointing	IRU, ACA	RWA	Point at science target, with optional dither
Normal Maneuver	IRU	RWA	Slew between targets at peak rate of 2° per minute
Normal Sun	IRU, CSS, FSS	RWA	Acquire sun and hold spacecraft −Z axis and solar arrays to the sun
Powered Flight	IRU	RCS	Control *Chandra* during Liquid Apogee Engine burns
RCS Maneuver	IRU	RCS	Control *Chandra* using the RCS
Safe Sun	IRU, CSS, FSS	RWA	Safe mode: acquire sun and hold spacecraft −Z axis and solar arrays to the sun
Derived Rate Safe Sun	IRU, CSS, FSS	RWA	Similar to Safe Sun Mode, but using only one gyro (two axes) plus sun sensor data
RCS Safe Sun	IRU, CSS, FSS	RCS	Same as Safe Sun Mode, but using RCS instead of RWA for control

Aspect monitor

To determine the accurate pointing of the satellite, *Chandra* has two kinds of aspect monitor system. One is Inertial Reference Units (IRU), and the other is constructed with Aspect Camera Assembly (ACA), Fiducial Light Assemblies (FLA), and Fiducial Transfer System (FTS).

IRU consists of two 2-axis gyroscopes, and can measure angular rates about 4 axes. Since two IRUs are boarded, 8 axes can be measured in total. All 8 axes are in different directions and no three axes lie in the same plane. However, only four axes data can be read at one time.

ACA is a CCD camera, which is placed on the side of the HRMA, to track optical stars. Simultaneously, fiducial lights irradiated from the LEDs at the science instrument (SI) module passes through FTS, and is also imaged onto the ACA CCD (Figure 3.13). ACA can track up to 8 images, which are typically 5 stars and 3 fiducial lights. Only star images are used to control the attitude. Fiducial lights are used in ground processing to determine the accurate position by comparison with the star images.

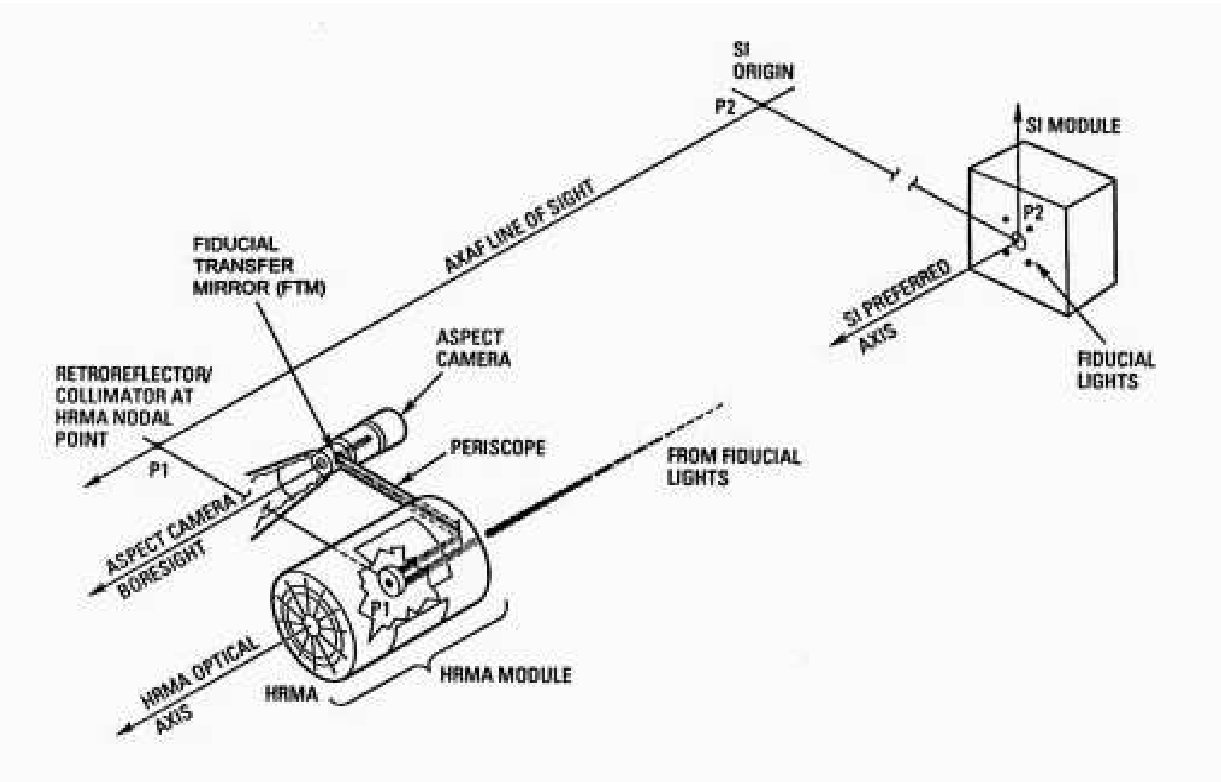

Figure 3.13: Aspect determination subsystem of ACA, FLA, and FTS. Optical stars and the fiducial light from the SI module are monitored by the CCD camera.

In addition to aspect monitors, there are two sun sensors: Coarse Sun Sensor (CSS) to cover 4π steradian, and Fine Sun Sensor (FSS) for higher resolution of $0^{\circ}.02$. Earth Sensor Assembly

(ESA) is used during the orbital insertion phase. These sensors are not used in processing X-ray images.

Dithering

HRMA exhibits very high spatial resolution, which is comparable to the pixel size of focal instruments (section 3.2.3). To avoid X-rays from a point source falling on a limited number of pixels, the line-of-sight is dithered continuously in Normal Point Mode. Dithering distributes photons over many detector elements (microchannel pores or CCD pixels), and serves several purposes: reduces uncertainty due to pixel to pixel variation in quantum efficiency (QE); allows sub-sampling of the image, and; provides some exposure in the gaps between the CCD.

The dither pattern is a Lissajous figure with an peak-to-peak amplitude of $16''$ for ACIS, and $40''$ for HRC. This pattern is corrected in ground processing by using the data of aspect monitors. The default dither periods are 706.96 sec (pitch) and 999.96 sec (yaw). Due to the dithering, point sources near the edge or the gap of the CCD chips observed intermittently. These sources could exhibit fake periodicity at these periods.

Performance

The uncertainties of the pointing and the reconstructed image are shown in Table 3.2. Absolute celestial pointing and PCAD 10-second pointing stability show the accuracy of the satellite attitude (the direction of the optical axis of HRMA) in the observation time. Then the images are reconstructed in ground processing, and each X-ray position is determined with the uncertainty of less than $0''.3$ (RMS diameter). Celestial location accuracy measures the absolute accuracy of the point sources with accurately known coordinates.

Table 3.2: Aspect System Performance of *Chandra*

Description	
Absolute celestial pointing	$3''.0$ (99.0%, radial)
PCAD 10 sec pointing stability	pitch $0''.043$ (RMS, 1-axis)
	yaw $0''.030$
Image reconstruction	$0''.3$ (RMS diameter)
Celestial location	$0''.6$ (RMS radius)

3.2.3 HRMA (High Resolution Mirror Assembly)

The *Chandra* telescope has four pairs of Wolter Type-I mirrors, which were fabricated from Zerodur glass, polished, and coated with iridium on a binding layer of chromium (Figure 3.14). The outer diameters of mirrors are 1.23, 0.99, 0.87, and 0.65 meter, and the focal length is 10.066 meter.

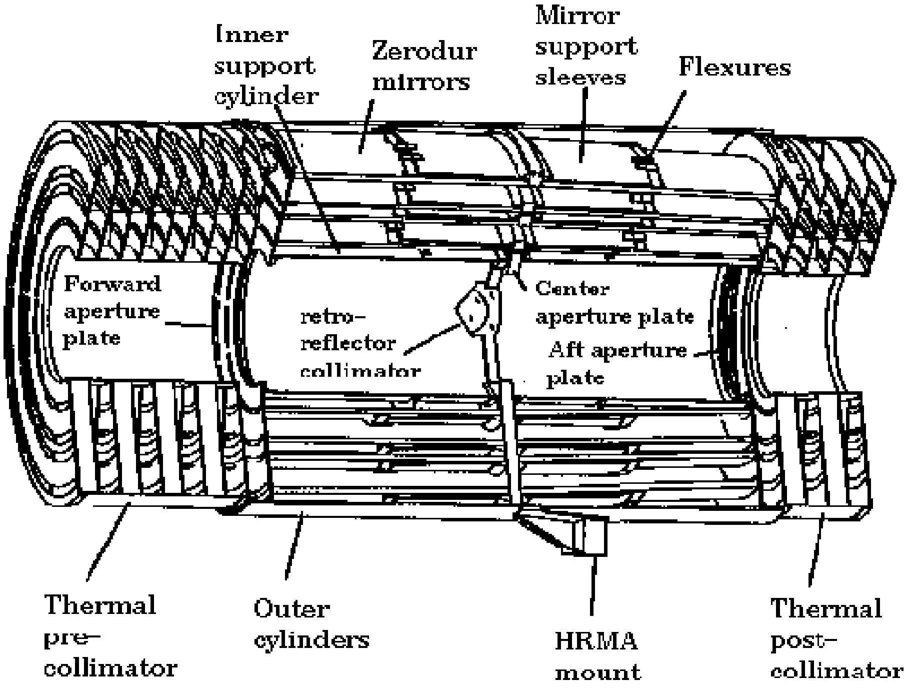

Figure 3.14: HRMA mirrors

Figure 3.15a,b show the effective area of HRMA in relation to X-ray energy and off-axis angle, respectively. On-axis effective area is about 800 cm^2 at 0.25 keV, and declines to 400 cm^2 at 5.0 keV, 100 cm^2 at 8.0 keV. The effective area also decreases as source position departs from on axis.

The point-spread function (PSF) is very sharp, and most of X-ray photons are collected within $1''$-radius region (Figure 3.16). The encircled energy function of HRMA is shown in Figure 3.17a. At 4.51 keV, the 50% photons are included in about $0.''35$-radius, which is called the encircled energy radius. The encircled energy radius increase, or PSF becomes broad, at the larger off-axis angle. Encircled energy radius is shown in Figure 3.17b. The diameter, which encircles 50% energy, is called Half Power Diameter (HPD).

The central $29'$ diameter region of the field of view is free from stray light, because baffles prevent non-reflected or singly reflected X-rays. Then, there is no ghost image.

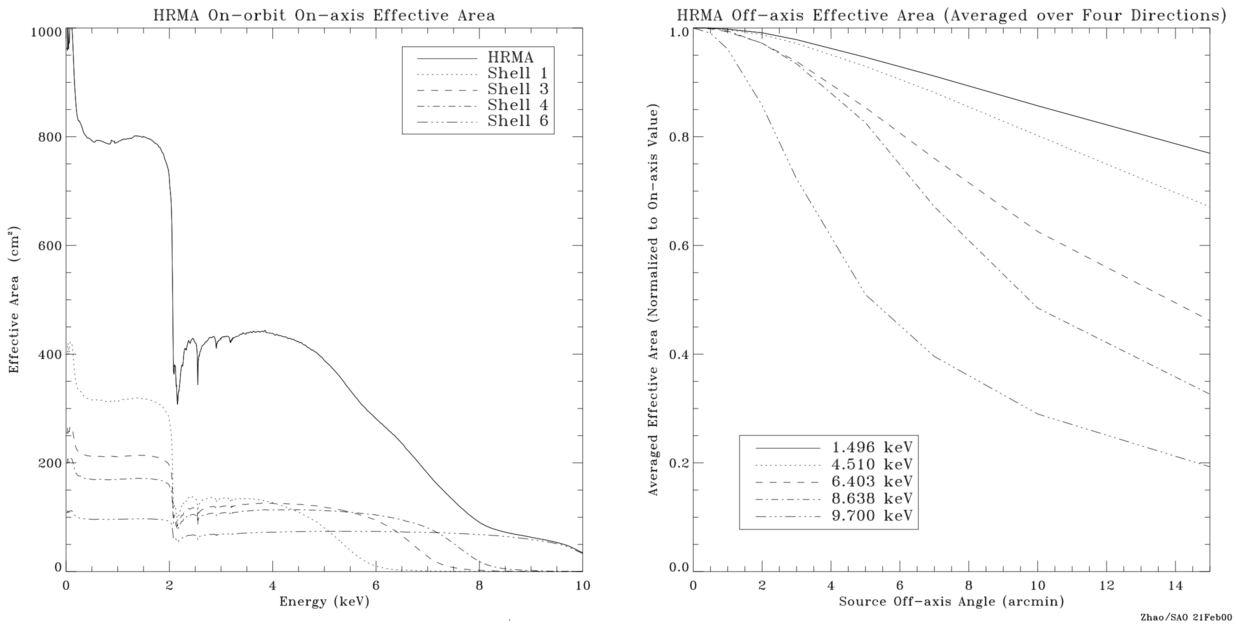

(a) Effective area vs. X-ray energy (b) Effective area vs. off-axis angle

Figure 3.15: The HRMA effective area versus X-ray energy (left; a) and off-axis angle (right; b). In the left panel, shell 1, 3, 4, 6 indicate the mirror layers from outside to inside.

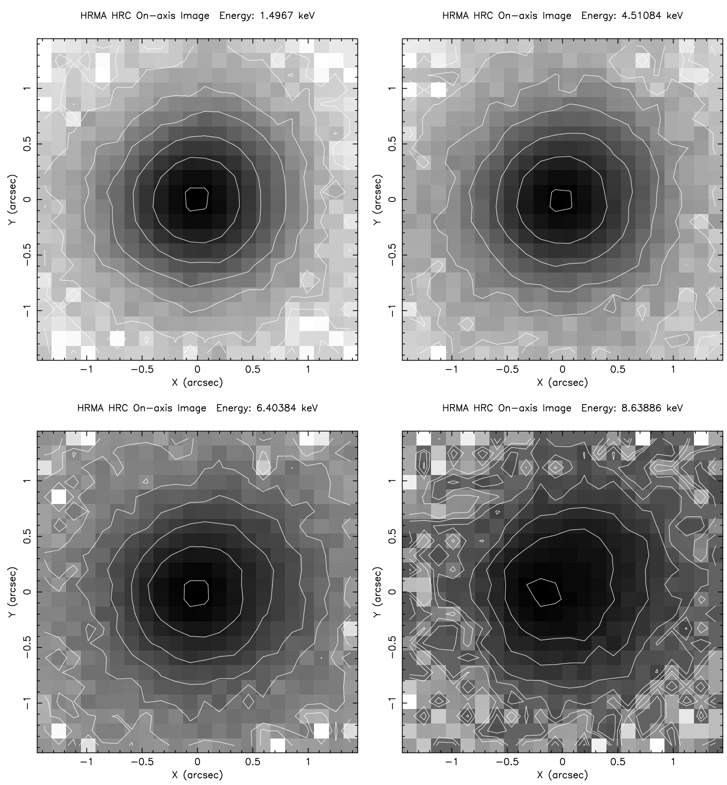

Figure 3.16: Simulated on-axis images with the energies of 1.49, 4.51, 6.40, and 8.63 keV. Surface brightness contours are logarithmic and spaced in factors of 3. The innermost contour is at 90% of the peak brightness. The 8.6 keV image core is off-center due to the shell misalignment.

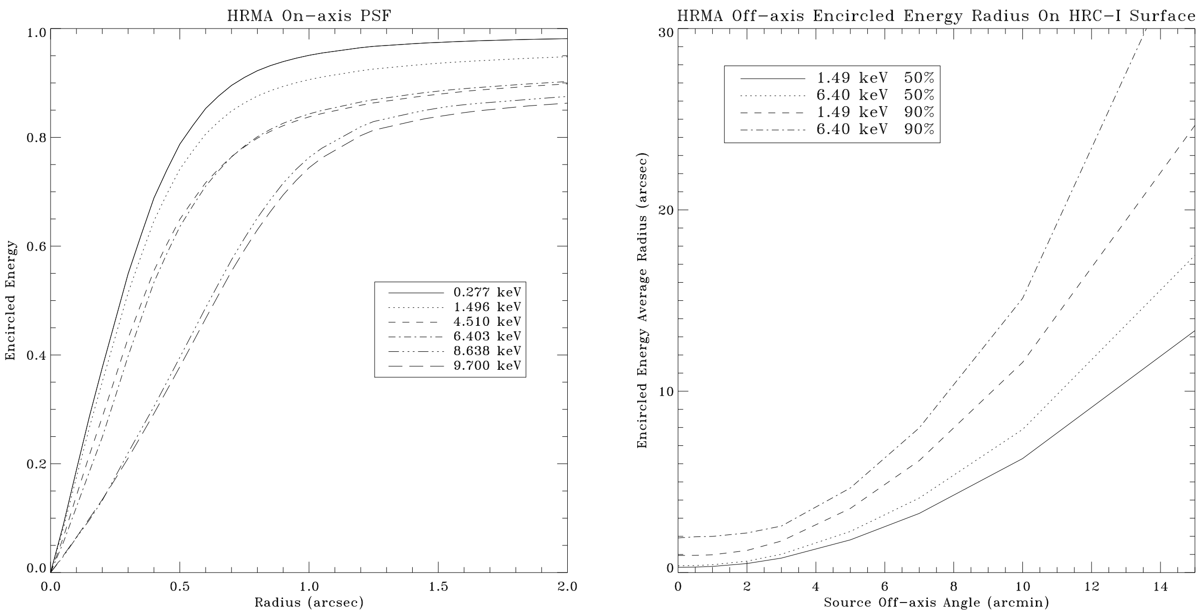

(a) Encircled energy function (b) Encircled energy radius

Figure 3.17: Encircled energy radius of HRMA

3.2.4 ACIS

The Advanced CCD Imaging Spectrometer (ACIS) is comprised of ten 1024 × 1024 pixel CCDs; 2 × 2 array of ACIS-I (I0–I3) for imaging and 1 × 6 array of ACIS-S (S0–S5) for imaging and grating spectroscopy. The pixels are 24 μm ($\sim 0''.5$) square. Two CCDs (S1 and S3) are back-illuminated (BI) and the others are front-illuminated (FI). The layout of CCD chips is shown in Figure 3.18 and Figure 3.19. The CCD chips of ACIS-I and ACIS-S are tilted to follow the HRMA focal surface and the HETG focal surface, respectively.

ACIS has many observing modes to apply variety observations, but we use only Timed-Exposure mode with the readout time of 3.24 s. X-ray events are extracted by the same way as *ASCA* or grade method. Though grade identification number is different from that of *ASCA*, X-ray events which are equivalent to *ASCA* grade 0, 2, 3, 4, 6 are used in standard analysis.

Figure 3.20(a) shows the energy resolution of CCDs before launch. The energy resolution of FI chips are near the theoretical limit, while BI chips exhibit poorer resolution. After the launch, the CCD chips are damaged with low energy protons, reflected by X-ray telescope onto the focal plane during radiation belt passages. Low energy protons deposit there energy in the buried channels at the HRMA side of the FI chips, and increase the Charge Transfer Inefficiency (CTI), which leads the degeneration of the energy resolution. Hence the energy resolution becomes a function of the row number shown in Figure 3.20(b). Since the gate structure of BI chips are at opposite side to the HRMA, the energy resolution of BI CCDs

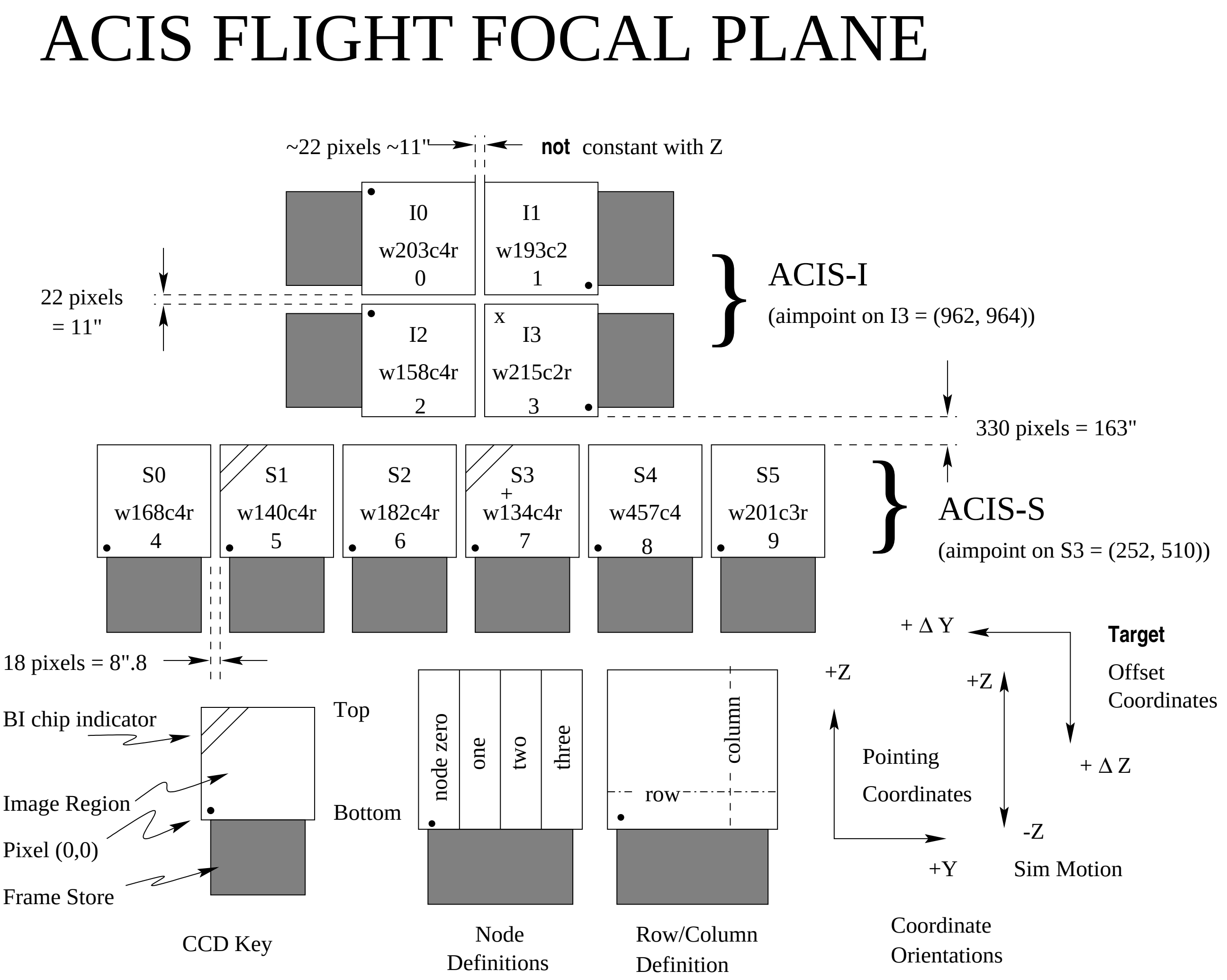

Figure 3.18: A schematic overhead view of the ACIS focal plane; the legend of the terminology is given in the lower left. Nominal aimpoints of ACIS-I and ACIS-S are shown by 'x' and '+' mark, respectively.

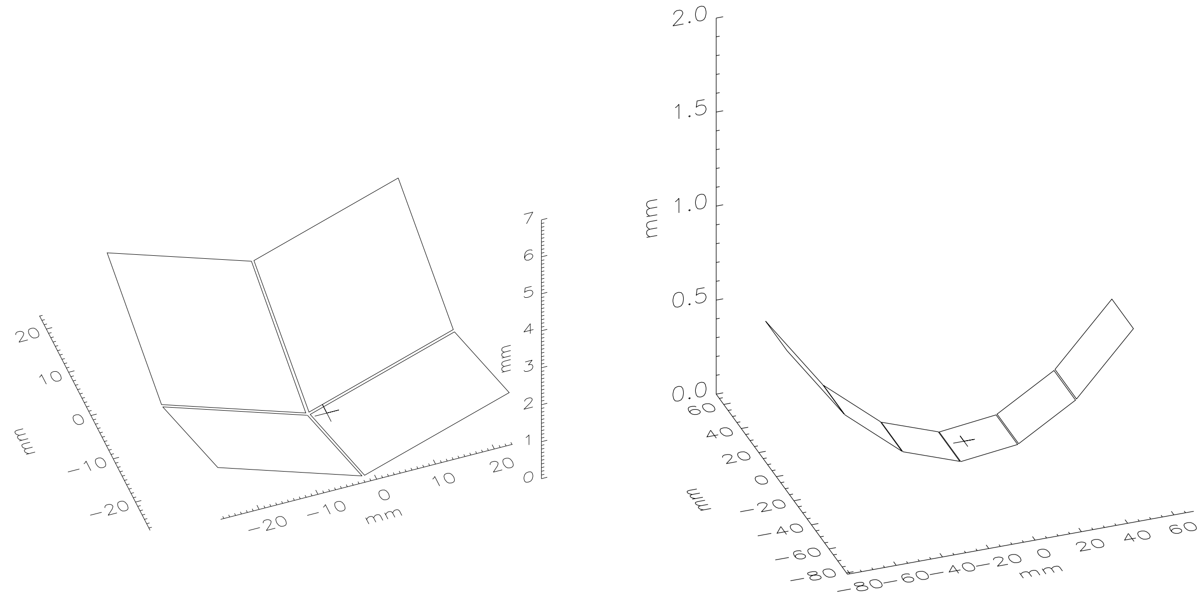

(a) ACIS-I (b) ACIS-S

Figure 3.19: A schematic perspective view of the layout of (a) ACIS-I and (b) ACIS-S; note that vertical axes are not to scale. The aimpoints are indicated in '+' marks.

remains at their prelaunch values. In the present operation, the ACIS is not left at the focal position during radiation belt passages, and no further degradation in performance has been encountered. By decreasing the CCD temperature from −90°C (before damaged) to −120°C, the CTI effect is reduced as possible.

The quantum efficiency of ACIS is shown in Figure 3.21. Low-energy X-rays are largely absorbed by Optical Blocking Filter (OBF) and the gate structure of the CCD chips. Since BI chips have the gate at the opposite side to HRMA, the quantum efficiency of BI CCDs are larger than those of FI CCDs in low-energy band. By the increase of CTI, the quantum efficiency becomes smaller at the farther side from the readout.

3.2.5 Other Instruments — HRC, HETG & LETG

HRC is a microchannel plate comprised of HRC-I for imaging and HRC-S for grating spectroscopy with LETG. The features are a large field of view ($30' \times 30'$; HRC-I), faster time resolution ($\sim 16\mu$s), and higher angular resolution (FWHM $\sim 20\mu$m). However, energy resolution is poor with $\Delta E/E \sim 1$ at 1 keV.

HETG and LETG are designed for grating spectroscopy with ACIS-S or HRC-S. HETG is used for higher energy range of 0.4–10.0 keV, and LETG is for lower energy of 0.07–7.29 keV with HRC-S and 0.2–8.86 keV with ACIS-S. Their characteristics are high energy resolving

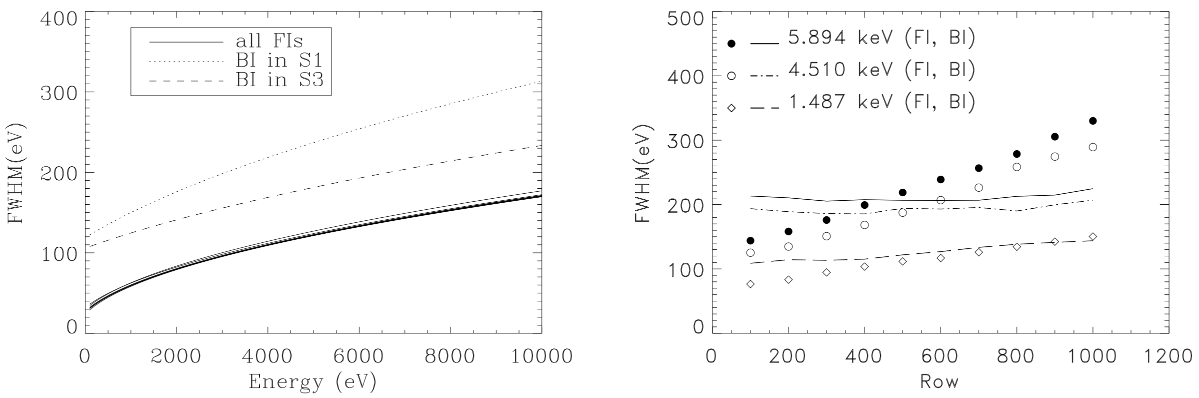

(a) prelaunch energy resolution (b) energy resolution after damaged

Figure 3.20: (a) The prelaunch energy resolution of ACIS FI chips (solid lines) and BI chips (dashed and dotted lines). (b) The energy resolution of proton damaged ACIS CCDs (I3 and S3) as a function of row number. The energy resolution of FI chip (I3) is shown by data points (diamonds, open circles, filled circles), and that of BI chip is shown by lines (dashed, dash-dotted, solid). These data were taken at −120 °C.

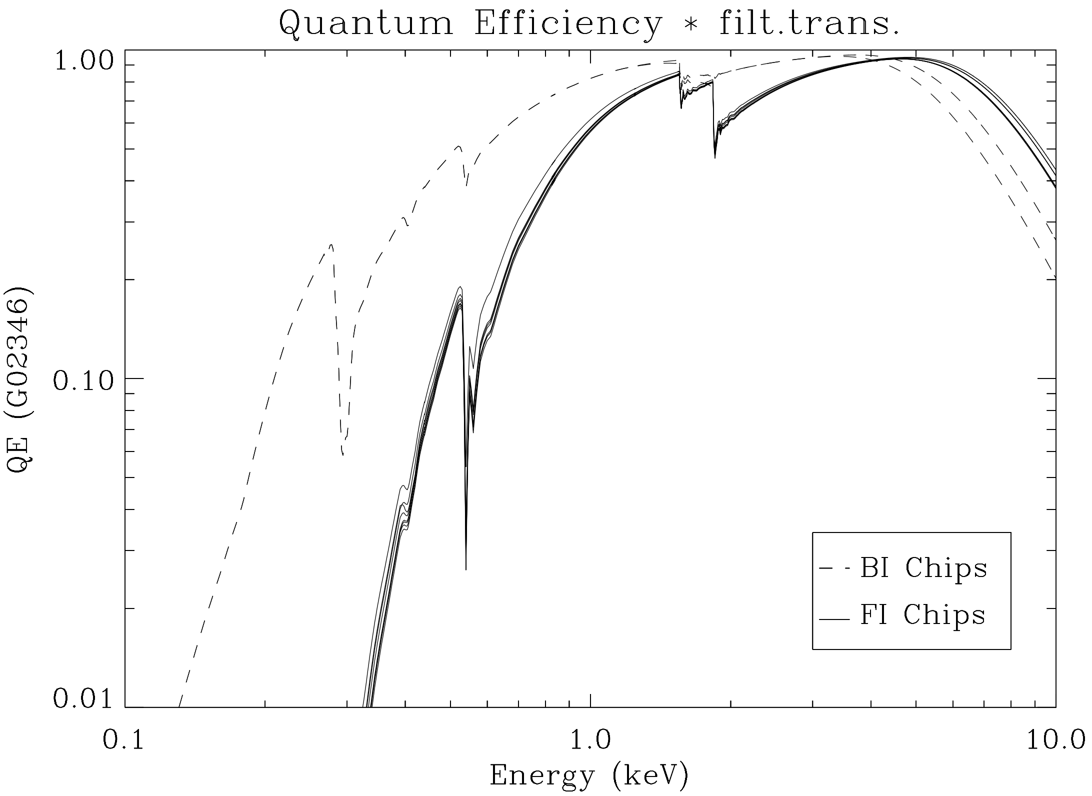

Figure 3.21: The quantum efficiency of the ACIS CCDs. Note that values are including the transmission rate of the OBF.

power of $\Delta E/E \lesssim 1000$ (1000 at 1 keV) for HETG, and $\Delta E/E \gtrsim$ 1000 between 0.07–0.15 keV for LETG. Since the resolution of wavelength is constant in each instrument, the resolving power becomes lower at higher energy band.

These instruments are not used in this thesis. For our objective of investigating diffuse structures in the GC region, ACIS-I is the best instrument with the moderate energy resolution and sufficiently good spatial resolution.

Chapter 4

Observations

4.1 *ASCA*

With *ASCA*, we observed the GC region over 100 times. Beginning with the mapping observations of central $1^\circ \times 1^\circ$ region in PV (Performance Verification) phase, we almost cover $4^\circ \times 4^\circ$ of the GC region till AO-7 (7th Announcement of Opportunity) phase (see exposure map in Fig 4.1; also refer to Sakano 2001). In this thesis, we analyze the data of the regions which include the giant molecular clouds: Sgr B2, Sgr C, Radio Arc (M0.11$-$0.08), and Clump2. Most of these regions are observed in many times, and the exposure time of each region is generally large with about 100 ksec in total. However, the Sgr C region is observed only about 20 ksec in PV phase. The exposure time, the observing date, and the pointing coordinate of each observation are shown in Table 4.1.

GISs are operated in the PH mode with the standard bit-assignment (10-8-8-5-0-0; see the previous chapter). While SIS mode varies from 4-CCD mode in the early observations to 1-CCD mode in the later observations, because SISs are largely damaged with charged particle radiations. In addition, the SISs are smaller FOVs and poorer quantum efficiency than GISs. We mainly use GIS data in this thesis.

The data were post-processed to correct for spatial gain non-linearity. We removed data taken at low Earth elevation angles, at low geomagnetic cutoff rigidities, or during the passage through the South Atlantic Anomaly. For the SIS, we also excluded the data taken at elevation angles from the bright Earth rim less than 25°.

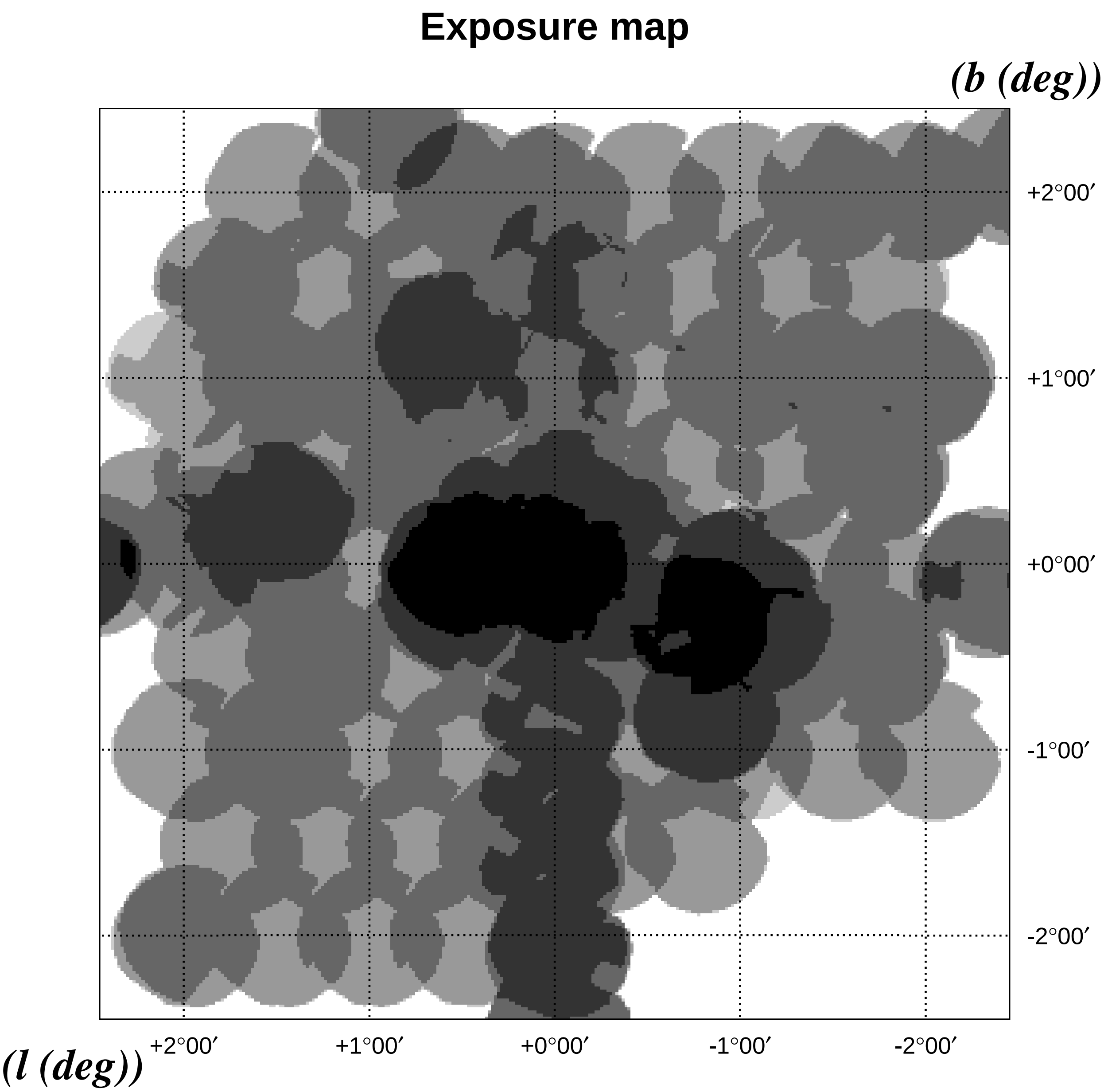

Figure 4.1: Exposure map of the *ASCA* observations in the GC $5^\circ \times 5^\circ$ region with the galactic coordinates (Sakano 2001). The gray levels are log(EXP[sec]) of 3.0, 3.5, 4.0, 4.5, 5.0, 5.5. The position of the calibration source for GISs is removed from each pointing. Sgr B2 and Radio Arc is in the darkest region near the center of the image, and Sgr C is in the second darkest region at the right of the center. Clump2 ($l_{\rm II} \sim 2\overset{\circ}{.}6$) is out of the figure.

Table 4.1: Observational log of *ASCA*

ID	Date		Coordinates		Exp.†	Name
	Start	End	l_{II}	b_{II}		
	(UT)‡	(UT)‡	(deg.)	(deg.)	(ksec)	
1	1993/10/01-21:14	1993/10/02-10:25	0.49	−0.09	17.2	GC(0.37,−0.37) §
2	1993/10/04-02:11	1993/10/04-16:30	359.44	0.09	19.8	GC(−0.37,0.37) §
3	1994/09/15-22:01	1994/09/17-14:00	359.99	−0.06	81.9	SGR A §
4	1994/09/22-03:44	1994/09/23-12:10	0.54	−0.02	58.1	SGR B N1
5	1994/09/24-02:03	1994/09/24-14:41	0.54	−0.02	19.7	SGR B N2
6	1999/09/06-02:19	1999/09/08-18:12	2.61	0.01	77.1	Clump2

†: The average of the exposures with GIS2 and GIS3 after the screening.

‡: (Year/Month/Date-Hour:Minute).

§: Observations ID 1–3 include Sgr B2, Sgr C, and the Radio Arc region, respectively.

4.2 *Chandra*

Chandra observed the GC region 34 times with ACIS-I: 4 pointing observations for particular objects (Sgr A*, Sgr B2, Radio Arc, 1E1740.7−2942) and 30 mapping observations of the GC survey. Exposure time of a each observation for the GC survey is about 10 ksec, while pointing observations have larger exposure time of about 50–100 ksec except for 1E 1740.7−2942 ($\sim$ 9 ksec). The observation log is shown in Table 4.2.

Figure 4.2 shows the schematic figure of the FOVs of *Chandra*, and Figure 4.3 shows the exposure map. GC survey covers $-1^\circ \leq l_{II} \leq 1^\circ$, $-0\overset{\circ}{.}4 \leq b_{II} \leq 0\overset{\circ}{.}4$ with about 10 ksec exposure. FOVs of GC survey are overlapping on the Galactic plane ($-0\overset{\circ}{.}2 \leq b_{II} \leq 0\overset{\circ}{.}2$), hence 20 ksec exposure is made in these region. All observations are made in Timed-Exposure mode.

Observed data are screened in a standard criteria to remove flaring pixels and artificial stripes caused probably by hot pixels in the frame-store region and by particles which hit on the CCD node boundaries. The standard Good Time interval (GTI) filter is also applied to the events. Then we use a standard ACIS grade set of *ASCA* grade 0, 2, 3, 4, 6 to distinguish X-ray events from non X-ray background (NXB) events.

Table 4.2: Observational log of *Chandra*

ID	Date		Coordinates		Exp.†	Name
	Start (TT)‡	End (TT)‡	l_{II} (deg.)	b_{II} (deg.)	(ksec)	
1	1999/09/21-02:52	1999/09/21-16:53	359.94	−0.05	48.720	SGR A *
2	2000/03/29-09:44	2000/03/30-13:53	0.59	−0.02	98.989	SGR B2
3	2000/07/07-19:08	2000/07/08-09:14	0.14	−0.10	49.379	GALACTIC CENTER ARC
4	2000/08/30-16:59	2000/08/30-20:00	359.11	−0.11	9.357	1E 1740.7−2942
5	2001/07/16-02:15	2001/07/16-05:35	0.77	−0.20	10.746	GCS 1
6	2001/07/16-05:35	2001/07/16-08:44	0.78	0.00	10.550	GCS 2
7	2001/07/16-08:44	2001/07/16-11:52	0.77	0.19	10.560	GCS 3
8	2001/07/16-11:52	2001/07/16-15:01	0.58	−0.20	10.560	GCS 4
9	2001/07/16-15:01	2001/07/16-18:09	0.58	0.00	10.560	GCS 5
10	2001/07/16-18:09	2001/07/16-21:21	0.58	0.19	10.544	GCS 6
11	2001/07/17-14:11	2001/07/17-17:51	0.39	−0.20	11.939	GCS 7
12	2001/07/17-17:51	2001/07/17-21:19	0.39	0.00	11.754	GCS 8
13	2001/07/17-21:19	2001/07/18-00:48	0.39	0.19	11.760	GCS 9
14	2001/07/18-00:48	2001/07/18-04:16	0.19	−0.20	11.760	GCS 10
15	2001/07/18-04:16	2001/07/18-07:45	0.19	0.00	11.763	GCS 11
16	2001/07/18-07:45	2001/07/18-11:13	0.19	0.19	11.760	GCS 12
17	2001/07/18-11:13	2001/07/18-14:25	0.00	−0.20	10.762	GCS 13
18	2001/07/18-14:25	2001/07/18-17:37	0.00	0.00	10.762	GCS 14
19	2001/07/18-17:37	2001/07/18-20:49	359.99	0.19	10.762	GCS 15
20	2001/07/18-20:49	2001/07/19-00:01	359.80	−0.20	10.762	GCS 16
21	2001/07/19-00:01	2001/07/19-03:21	359.80	0.00	11.261	GCS 17
22	2001/07/19-03:21	2001/07/19-06:41	359.80	0.19	11.261	GCS 18
23	2001/07/19-06:41	2001/07/19-10:01	359.61	−0.20	11.261	GCS 19
24	2001/07/19-10:04	2001/07/19-13:25	359.61	0.00	11.632	GCS 20
25	2001/07/20-04:37	2001/07/20-08:00	359.61	0.19	10.950	GCS 21
26	2001/07/20-08:04	2001/07/20-11:10	359.41	−0.20	10.758	GCS 22
27	2001/07/20-11:15	2001/07/20-14:38	359.41	0.00	11.760	GCS 23
28	2001/07/20-14:44	2001/07/20-18:07	359.41	0.19	11.747	GCS 24
29	2001/07/20-18:12	2001/07/20-21:35	359.21	−0.20	11.763	GCS 25
30	2001/07/20-21:41	2001/07/21-01:04	359.22	0.00	11.763	GCS 26
31	2001/07/21-01:09	2001/07/21-04:32	359.22	0.19	11.763	GCS 27
32	2001/07/21-04:35	2001/07/21-08:03	359.02	−0.20	11.763	GCS 28
33	2001/07/21-08:03	2001/07/21-11:32	359.02	0.00	11.763	GCS 29
34	2001/07/21-11:32	2001/07/21-15:03	359.02	0.19	11.763	GCS 30

†: The exposure time of ACIS

‡: (Year/Month/Date-Hour:Minute). The unit is Terrestrial Time
(see `http://tycho.usno.navy.mil/systime.html`).

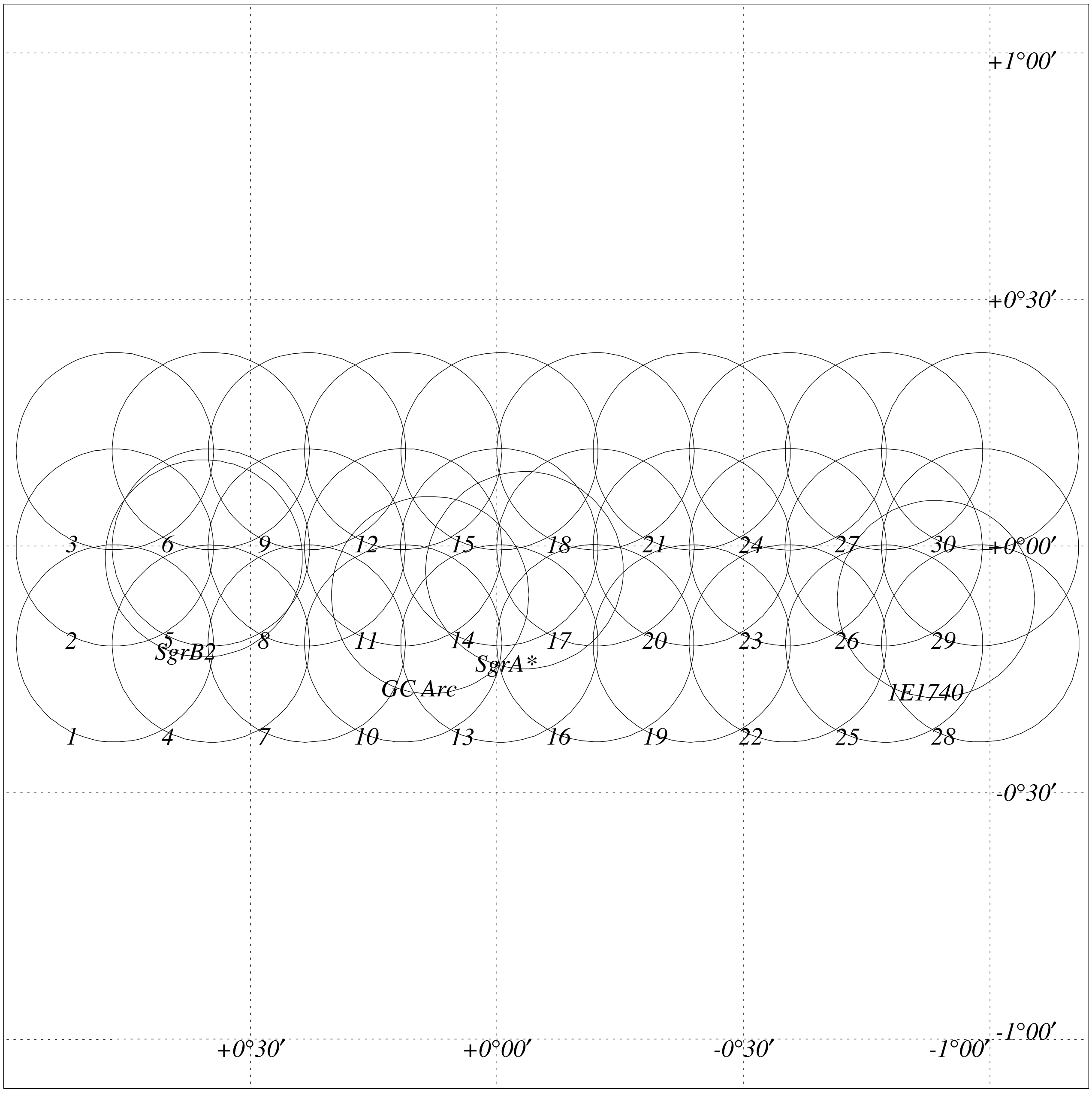

Figure 4.2: The FOVs of *Chandra* at the GC region. Each FOV is drawn in 12′-diameter circle. Note that the real field of ACIS-I is a inscribed square of the circle. Label 1–30 shows the observed field of GCS 1–30, and Sgr A*, Sgr B2, Galactic center Arc (GC Arc), 1E1740.7−2942 (1E1740) are indicated in their own names.

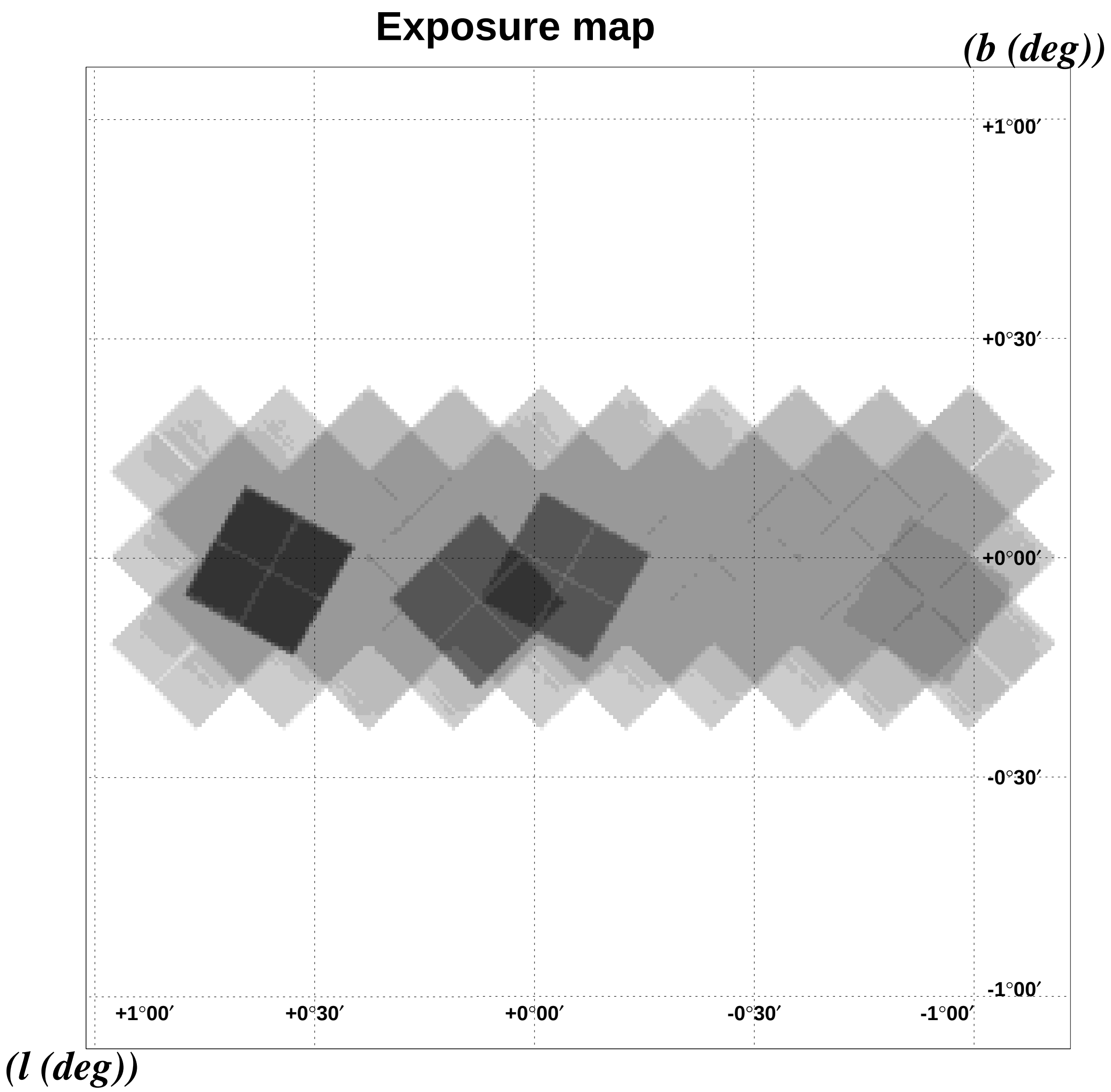

Figure 4.3: The exposure map of the *Chandra* observations in the GC region. The observed time of each observation is shown in gray scale with log of $10^{3.5}$–$10^{5.5}$ sec.

Chapter 5

Results I. — 6.4-keV line emissions

At first, we study about the origin of the 6.4-keV line in the GC region. Koyama et al. (1996) already indicated that 6.4-keV line emissions are coincident with the giant molecular clouds (Figure 2.9). Then we investigate the X-ray spectra and images of the heavy molecular clouds: Sgr B2, Sgr C, M0.11−0.08 (at the Radio Arc region), and Clump 2. Most of the clouds are observed with both *ASCA* and *Chandra*, but Clump 2 is observed only with *ASCA*.

5.1 Sgr B2

Sgr B2 is one of the heaviest giant molecular clouds in the Galactic center region, and the most luminous in the 6.4-keV line band (see section 2.3, 2.4).

5.1.1 *ASCA* Observations

Two observations of Sgr B2 were made with *ASCA* on October 1 1993, and on September 22–24 1994. In these observations, we analyze both GIS and SIS data. The net observed time is about 95 ksec for GIS and 85 ksec for SIS (section 4.1). Since no time variability is found between the two observations, we analyzed the combined data. The results are already published in Murakami et al. (2000).

6.4-keV line image

Figure 5.1 shows the X-ray images in narrow energy bands with a central energy of 6.4 keV and width of twice the energy resolution (FWHM): 5.8–7.0 keV for the GIS and 6.2–6.6 keV for the SIS. We found a distinct peak near the center of the molecular cloud. The position of the X-ray peak is determined as R.A. (2000) $= 17^{\rm h}\ 47^{\rm m}\ 20^{\rm s}\!.5$, Dec (2000) $= -28^\circ\ 24'\ 20''$ ($l = 0^\circ\!.6496$, $b = -0^\circ\!.0470$) and R.A. (2000) $= 17^{\rm h}\ 47^{\rm m}\ 20^{\rm s}\!.3$, Dec (2000) $= -28^\circ\ 24'\ 13''$ ($l = 0.6509$, $b = -0.0454$), for GIS and SIS respectively. The statistical errors are $10''$ for the GIS and $15''$ for the SIS.

The SIS image is laid over the radio intensity contours of the CH_3CN line (Bally et al. 1988). The X-ray peak is shifted from that of the radio distribution by $\sim 1'.2$ to the Galactic center side.

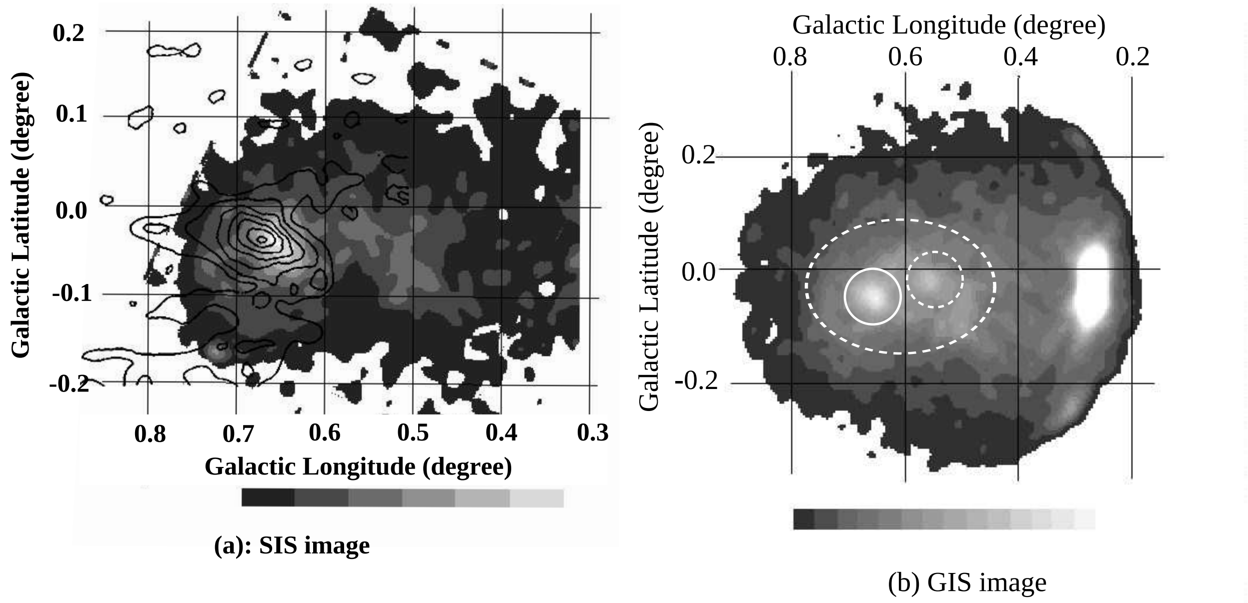

Figure 5.1: 6.4-keV line image of Sgr B2 obtained with *ASCA*. (a) SIS image laid over the CH_3CN line contours (Bally et al. 1988). The 6.4-keV brightness distribution is shifted from the radio distribution by $\sim 1'.2$ to the Galactic center side (to the right in the figure). (b) The 6.4-keV line image with GIS. The source and the background regions are shown by the solid circle and the dotted ellipse, respectively. The dotted circle encloses the other X-ray bright spot (G0.570−0.018; see section 6.2), which is excluded from the background region. The bright source at the boundary is a galactic binary X-ray source (1E 1743.1−2843).

Spectrum

The GIS spectrum given in Figure 5.2 is obtained by summing the X-ray photons in $3'$-radius circle around the X-ray peak of the GIS image. For the background spectrum, we used an elliptical region with the major axis parallel to the Galactic plane, excluding the region of Sgr B2 (a $3'$-radius circle) and the other X-ray bright spot (the other $3'$-radius circle) at the west of Sgr B2 (G 0.570−0.018; see section 6.2). The source and the background regions are

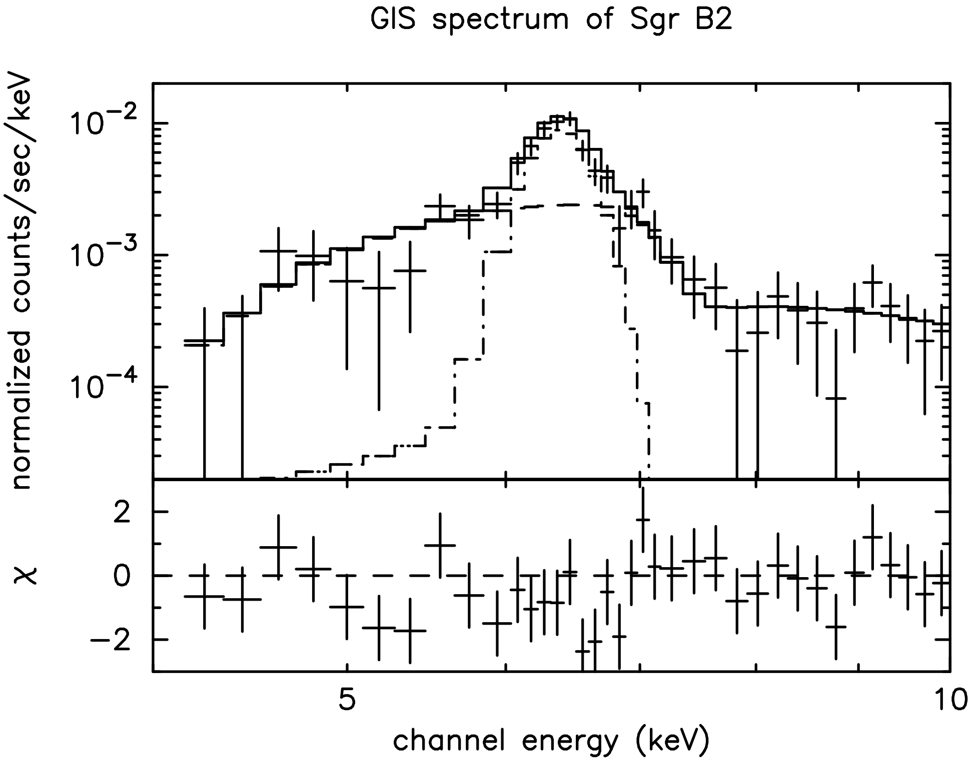

Figure 5.2: The GIS spectrum of Sgr B2. The best-fit model is shown in solid line.

shown in Figure 5.1b with the solid circle and dotted ellipse, respectively.

In order to derive quantitative feature of the Sgr B2 X-rays, we fit the spectrum to a phenomenological model, a power-law model with a Gaussian line. We used the Morrison & McCammon (1983) cross section for the absorption. Due to large absorption at low energy, the available data to be fitted are in the 4.0–10.0 keV band. However the limited energy band and rather poor statistics do not allow us to constrain all parameters simultaneously. Therefore we assumed a power-law of (fixed) photon index 2.0 (same as Koyama et al. 1996). We obtained the acceptable fittings with the best-fit χ^2 of 30.9 (34 degrees of freedom; hereafter d.o.f). The best-fit parameters are given in Table 5.1. The 6.4-keV line, as we expected, is very strong with an equivalent width of 2.9 keV. The hydrogen column density is $N_{\rm H} \sim 8 \times 10^{23}$ H cm^{-2}, and the absorption corrected luminosity is $\sim 10^{35}$ erg s^{-1}.

We also made a SIS spectrum and fit it with the same model of the GIS. However, since the limited photon statistics prevented us from determining the absorption depth, we fixed the hydrogen column to the best fit value for the GIS. The results are given in Table 5.1. The SIS results were found to be consistent with the GIS. The narrow field of view of SIS severely constrains the selection of the background region for the SIS spectrum and increases background-subtraction uncertainties. Here and after, we thus analyzed only the GIS spectrum for more detailed studies.

Table 5.1: Best-Fit Results of the *ASCA* Spectrum of Sgr B2.

	Continuum			Iron line				
	$N_{\rm H}$ [a]	Γ [b]	$F_{\rm X}$ [c]	$E_{\rm C}^{\rm d}$	$F_{\rm X}$ [c]	EW [e]	$L_{\rm X}$ [f]	χ^2/d.o.f.
GIS	$8.3^{+2.5}_{-2.0}$	2.0 (fixed)	15^{+3}_{-2}	6.38 ± 0.03	9.7 ± 1.0	$2.9^{+0.3}_{-0.9}$	$1.1^{+0.7}_{-0.5}$	30.9/34
SIS	8.3 (fixed)	2.0 (fixed)	18 ± 6	$6.43^{+0.02}_{-0.03}$	9.7 ± 1.7	$2.1^{+2.1}_{-0.8}$	$1.4^{+0.7}_{-0.9}$	35.1/45

^{a} : Hydrogen column density [10^{23} H cm^{-2}].

^{b} : Photon index of a power-law model for the continuum spectrum.

^{c} : Flux (no correction of absorption) in the 4–10 keV band [10^{-5} photons cm^{-2} s^{-1}].

^{d} : Center energy of iron line [keV].

^{e} : Equivalent width of iron line [keV].

^{f} : Absorption corrected luminosity in the 4–10 keV band [10^{35}erg s^{-1}].

To estimate the contamination of the 6.7-keV line from diffuse hot plasma in the Galactic center region, we fit the spectrum to the power-law and two narrow Gaussian lines at 6.4 and 6.7 keV. We found no significant line at 6.7 keV, with the flux less than 10% of the 6.4-keV line. Thus the observed line profile is reproduced by the 6.4-keV line alone.

The observed hydrogen column of 8×10^{23} H cm^{-2} is at least 5 (nearly 10) times larger than that of interstellar gas to the GC region (Sakano et al. 2000; see also section 5.5.1). This means that the large absorption column is due to local gas near or at the Sgr B2 cloud.

We found a deep iron edge in the spectrum. We fit the spectrum allowing the iron column density to be free. Then the iron column density is estimated to be $4{\times}10^{19}$ Fe cm^{-2}.

5.1.2 *Chandra* Observation

With Chandra, we can obtain highly resolved image, which arrows us to exclude the contribution of the point sources, and study detailed structure of the diffuse emission. The results are already published in Murakami, Koyama, & Maeda (2001).

6.4-keV line image

We make the 6.4 keV-line (6.15–6.55 keV) image to highlight the most detailed structure. Using the procedure given in Baganoff et al. (2001) and the algorithm of Ebeling, White & Rangarajan (2000), the image is flat-fielded, and is smoothed adaptively with circular Gaussian kernels. Figure 5.3 is the 6.4 keV line image overlaid on the radio intensity contours of the ^{13}CO molecule (Sato et al. 2000). The global morphology of the 6.4-keV emission is a concave-shape located at the south-west side (right hand side) of the molecular cloud pointing to the Galactic center direction (right hand side). The diffuse emission is distributed at R.A. (2000) $= 17^{\rm h}\ 47^{\rm m}\ 13^{\rm s}$–$27^{\rm s}$, Dec (2000) $= -28^\circ\ 21\rlap{.}'3$–$24\rlap{.}'8$ ($3' \times 3\rlap{.}'5$ rectangle shown by solid line in Figure 5.3).

We search the point sources in this region by the "wavdetect" method with the 3–8 keV image. 17 point sources are resolved in $3'\times3\rlap{.}'5$ region. The positions of the resolved point sources are indicated by solid circles with diameters of six times of the HPD of PSF. No significant excess of the point sources is found in this narrow band (6.15-6.55 keV) image, which indicates that the 6.4 keV line of normal point sources, unlike the diffuse emission, is not prominent. The local excess near the center and upper-left of the molecular cloud are possibly due to $\mathrm{H_{II}}$ complexes, Sgr B2 Main at $(l, b) \simeq (0.67, -0.04)$ and North at $(l, b) \simeq (0.68, -0.03)$. These two local excess occupy only 5 % flux in the total diffuse flux.

Spectrum

We first fit the combined spectrum of the resolved point sources. The spectrum can be reproduced by a thin thermal plasma model with the temperature of $\sim$ 8.5 keV. The best-fit parameters are shown in Table 5.2. The large column density of hydrogen indicates that most of these sources are located in the cloud. A detailed study of the point sources is made by Takagi, Murakami, & Koyama (2001).

Table 5.2: Best-Fit Results of the Combined Spectrum of Point Sources Obtained with *Chandra*

$N_{\rm H}^{a}$	kT^{b}	$F_{\rm X}^{c}$	$L_{\rm X}^{d}$	χ^2/d.o.f.
$1.9^{+0.6}_{-0.4}$	$8.5^{+9.3}_{-3.7}$	$1.5^{+0.5}_{-0.2}$	$2.9^{+1.1}_{-0.8}$	12.2/12

^{a} : Hydrogen column density [10^{23}H cm^{-2}].

^{b} : Temperature of a thin thermal plasma [keV].

^{c} : Flux (no correction of absorption) in the 2–10 keV band [10^{-5}photons cm^{-2} s^{-1}].

^{d} : Absorption corrected luminosity in the 2–10 keV band [10^{33}erg s^{-1}].

Figure 5.4 shows the spectrum of the diffuse X-ray emission by using the data from the solid square and subtracting background taken from the dotted circle in Figure 5.3. We find a faint peak at 7.1 keV, which is the center energy of Kβ line of neutral iron. We then fit the

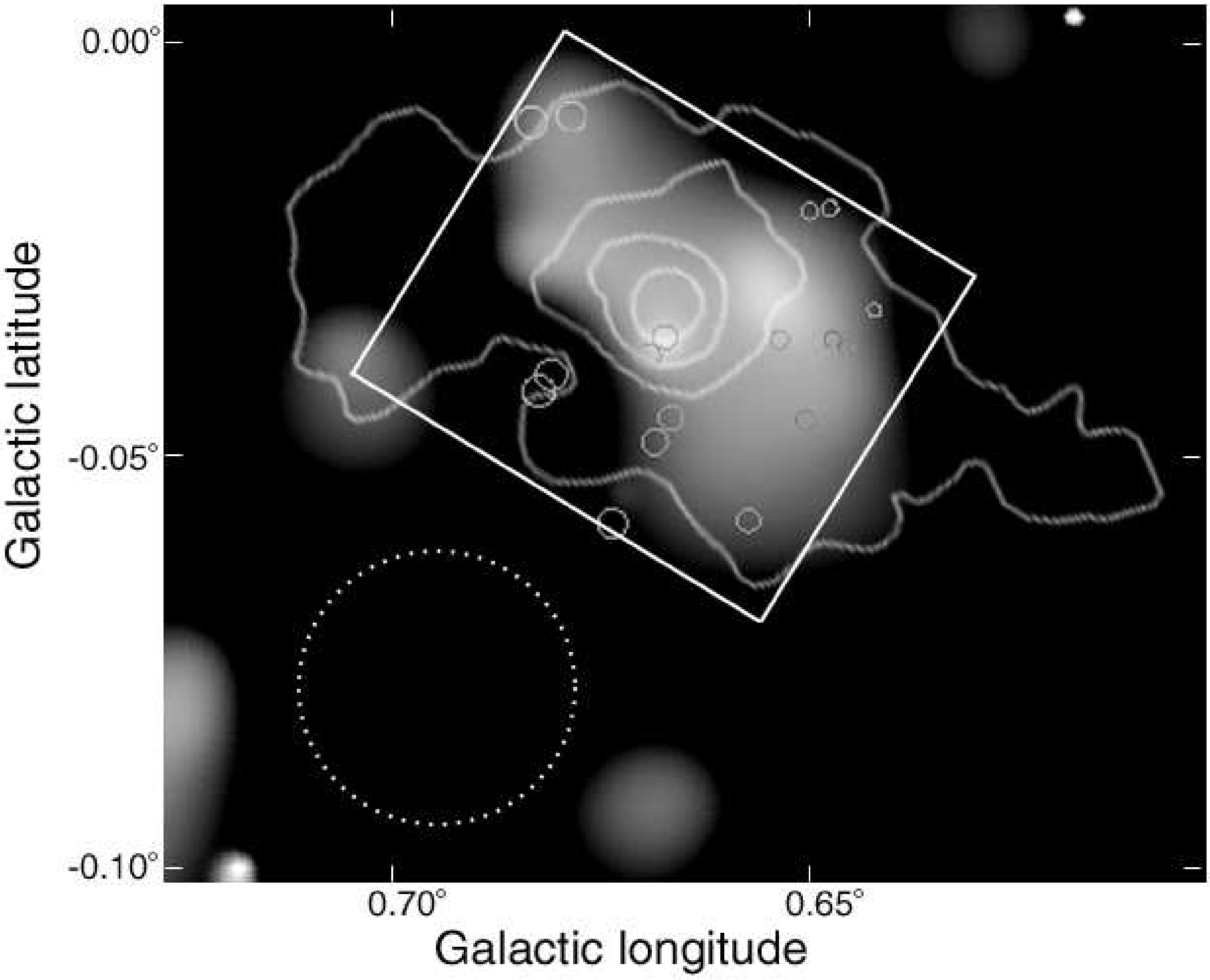

Figure 5.3: *Chandra* ACIS image of the Sgr B2 region in the 6.4-keV line band (6.15–6.55 keV). The contours show the radio intensity of the ^{13}CO molecule (Sato et al. 2000). The X-ray emission is located at the south-west (right hand) side of the molecular cloud. The source and the background regions are shown by solid and dotted lines, respectively.

spectrum with a phenomenological model, a power-law function of photon index 2.0, adding Kα and Kβ lines of neutral iron and absorption with the Bałucińska-Church & McCammon (1992) cross-sections for the solar abundances (Feldman 1992). Iron abundance, which is sensitive to the edge depth, is treated separately as a free parameter. The center energy and flux of iron Kα line are free parameters, but those of Kβ are linked to the Kα parameters by fixing the ratio to the laboratory values. Point source contamination is taken into account by adding the best-fit model of the combined point-source spectrum.

The best-fit parameters are given in Table 5.3. We find that the iron Kα line energy is $6.38^{+0.02}_{-0.01}$ keV, which is consistent with neutral irons of 6.40 keV. In order to examine whether highly ionized irons are present or not, we add 6.70 keV line, Kα of He-like iron, and constrain that the equivalent width is less than 0.07 keV, or at most 3 % of that of neutral irons. Column density of neutral iron ($N_{\rm Fe}$) determined from the K-edge structure is $\sim 3.4 \times 10^{19}$ cm^{-2}, while $N_{\rm H}$ determined from the low energy cutoff is $\simeq 8.8 \times 10^{23}$ cm^{-2}. Both are nearly ten times larger than those of the Galactic interstellar absorption (Sakano 2000; see 5.5.1), hence are attributable to the gas in Sgr B2. The *ASCA* results, in spite of its poor spatial resolution, are roughly consistent with the *Chandra* best-fit parameters, supporting that the contribution of the point sources is almost negligible.

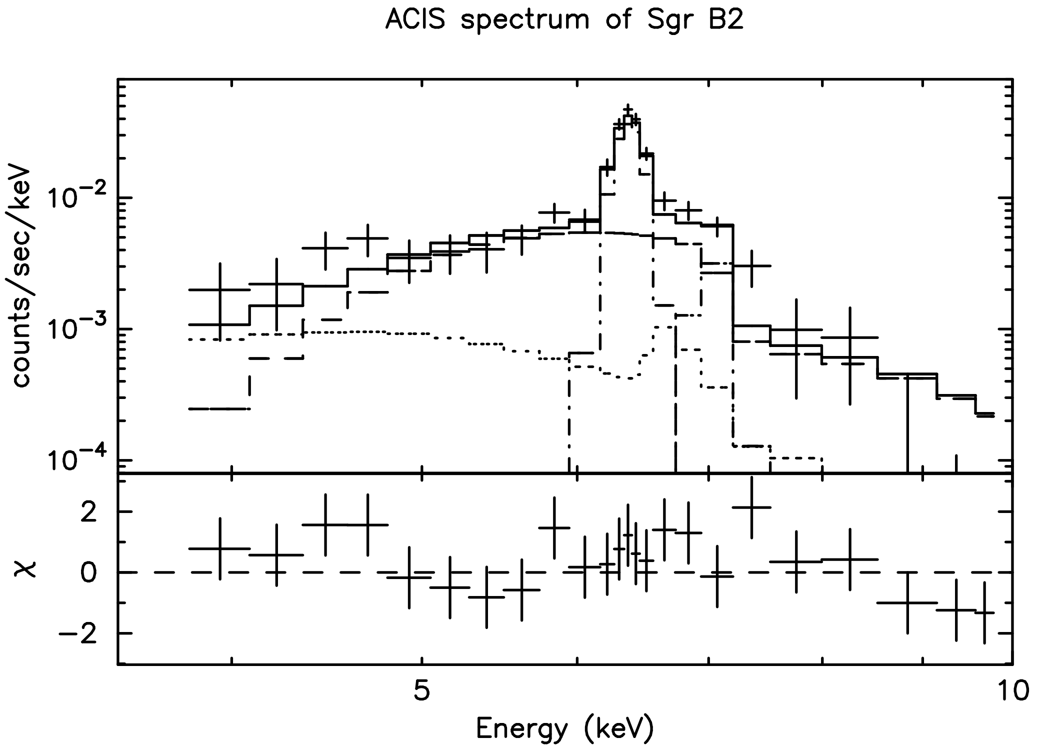

Figure 5.4: X-ray spectrum of Sgr B2 obtained with *Chandra* ACIS. The best-fit spectrum is shown in solid line.

Table 5.3: Best-Fit Results of the X-ray Spectrum of Sgr B2 obtained with *Chandra*.

		Continuum				Iron line					
N_H [a]	N_{Fe} [b]	Γ [c]	F_X [d]	E [e]	F_X [d]	EW [f]	E_C [e]	F_X [d]	EW [f]	L_X [g]	χ^2/d.o.f.
$8.8^{+2.0}_{-1.5}$	$3.4^{+3.6}_{-2.2}$	2.0 (fixed)	12^{+2}_{-1}	$6.38^{+0.02}_{-0.01}$	5.6 ± 0.5	$1.7^{+0.2}_{-0.1}$	$7.04^{+0.02}_{-0.01}$	1.1 ± 0.1	$0.28^{+0.02}_{-0.03}$	$1.0^{+0.4}_{-0.2}$	20.6/19

[a] : Hydrogen column density [10^{23}H cm^{-2}].

[b] : Iron column density [10^{19}H cm^{-2}].

[c] : Photon index of a power-law model for the continuum spectrum.

[d] : Flux (no correction of absorption) in the 4–10 keV band [10^{-5}photons cm^{-2} s^{-1}].

[e] : Center energy of iron line [keV].

[f] : Equivalent width of iron line [keV].

[g] : Absorption corrected luminosity in the 4–10 keV band [10^{35}erg s^{-1}].

5.1.3 Discussion

The *ASCA* observations discovered a 6.4-keV line emission, and the *Chandra* observation clearly detect diffuse X-rays from Sgr B2 by resolving underlying point sources. The diffuse X-rays are emitted from the south-west half (right side in Figure 5.3) of the cloud with a concave-shape morphology pointing to the Galactic center direction. The spectrum is characterized with the pronounced iron Kα line at $6.38^{+0.02}_{-0.01}$ keV, heavy absorption at iron K-edge and at low energy. Furthermore, Kβ line at $7.04^{+0.02}_{-0.01}$ keV is also discovered with *Chandra*. We examine the origin of the diffuse X-rays based on these results.

Young stellar objects

The giant molecular cloud Sgr B2 is known to be one of the richest regions of ongoing star formation in the Galaxy (e.g., de Vicente et al. 2000). In fact, many compact H_{II} regions as well as maser sources have been found from the cloud. These sources trace the star forming site in the cloud, and are found from the ridge running north to south (Figure 2.3). Since young stellar objects (YSO), regardless low mass or high mass stars, are rather strong X-ray sources with luminosity ranging from 10^{32-33} (massive YSO) to 10^{28-29} erg s^{-1} (low mass YSO) (e.g., Feigelson 1999), numerous unresolved YSOs in Sgr B2, if any, may mimic the diffuse X-rays. Sidoli et al. (2001) also proposed the point source origin from the observations by BeppoSAX. The spatial distribution of the diffuse X-rays, a concave-shape, however is largely different from that of the north-south ridge of star formation. The X-ray spectra of YSOs are generally consistent with optically thin thermal plasma of temperature ranging from 1 keV to a few keV, with the 6.7 keV line of He-like irons present in some cases. The spectrum of the Sgr B2 diffuse is completely different from that of typical YSOs, hence a YSO origin is ruled out for the bulk of the diffuse X-rays. Partial contribution of YSOs may still be conceivable in the two local enhancement at the cloud center and north, Sgr B2 Main and North (see Figure 5.3). We hence examine the X-ray spectrum from these two regions and find no essential difference from the total diffuse spectrum. We only see a hint of a weak 6.7 keV line with the equivalent width of 0.10 ± 0.07 keV. Consequently, we can safely conclude that no significant contribution of YSOs is found in the spectrum and morphology of the diffuse X-rays of Sgr B2.

X-Rey reflection due to internal point sources

It may be conceivable that the resolved point sources in Sgr B2 irradiate the surrounding gas and produce the reflected X-rays. These point sources, however, are uniformly distributed in the cloud (see Figure 5.3), which disagrees with the concave-shape of the diffuse X-rays. The integrated luminosity of all the resolved point sources is 3×10^{33} erg s^{-1}, which is only 3% of the luminosity of the diffuse X-rays. Therefore internal point sources can be ignored.

X-Ray Reflection Nebula model

The most plausible scenario is "X-ray Reflection Nebula" (XRN) model, as proposed in Koyama et al. (1996).In this model, the molecular cloud is irradiated by an external X-ray source, and emit fluorescent and scattered X-rays. The large absorption, the strong neutral iron line, and the shifted X-ray peak from the cloud core agree with the X-ray features irradiated heavy molecular cloud. The 6.4-keV line is strong evidence of reflection, in particular. Since X-ray emitting gas is very hot with the temperature of $\gtrsim 10^7$ K, iron atoms are immediately ionized to He- or H-like state. Neutral irons are too cold to emit thermal X-rays by themselves, and can emit only fluorescent X-rays.

Inoue (1985) calculated the equivalent width of fluorescent 6.4-keV line in three cases (Figure 5.5). If we observe only scattered and fluorescent X-rays, the equivalent width should be about 2 keV at the range of column density $\lesssim 10^{24}$ H cm^{-2}. The observed equivalent width of 1.71 keV from Sgr B2 is consistent to this case, and other two cases (fluorescent and primary X-rays are observed simultaneously) cannot produce such a strong 6.4-keV line.

We examine this scenario in detail with numerical simulations in section 5.5.

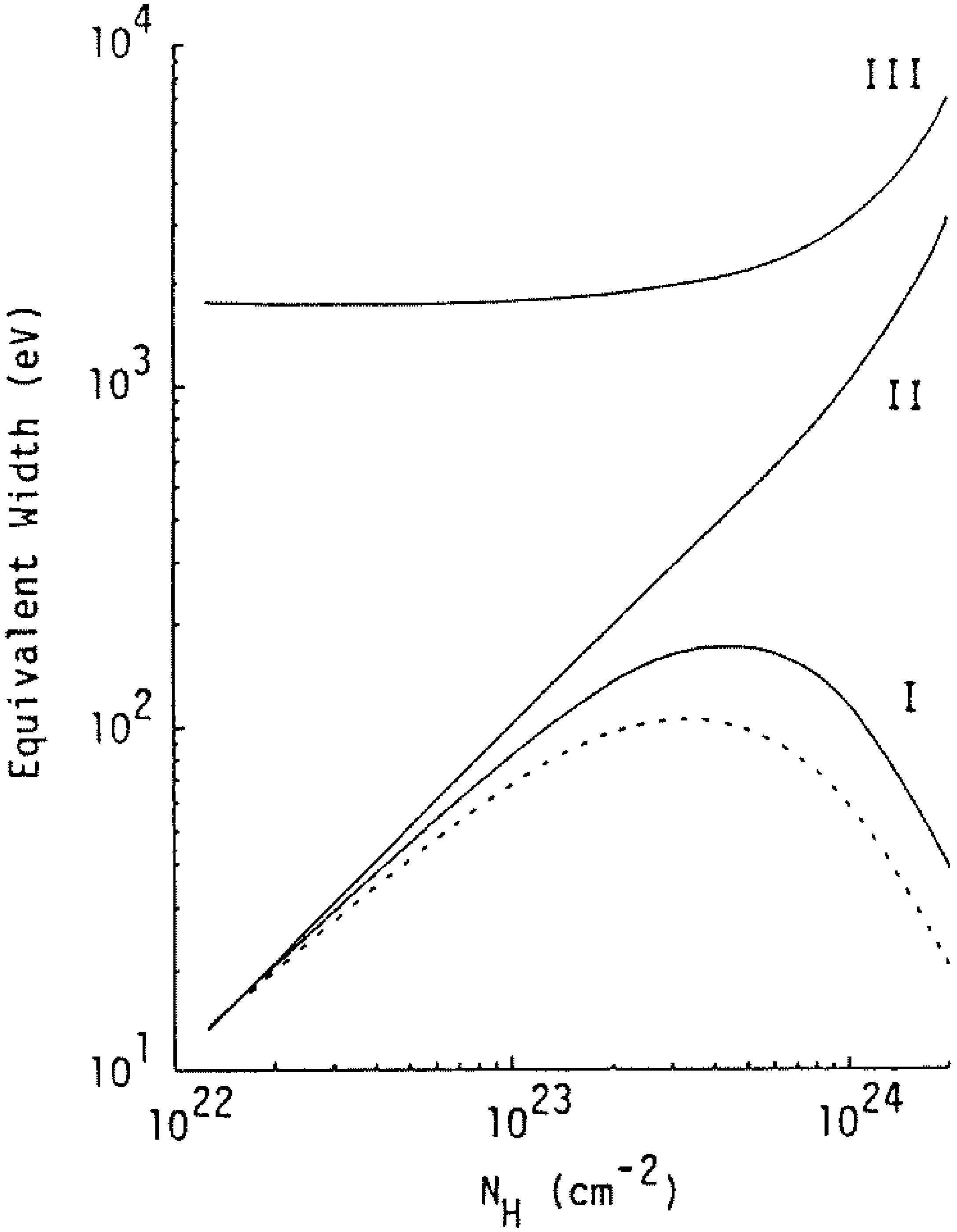

Figure 5.5: The simulated equivalent width of fluorescent iron 6.4-keV line as a function of column density of scattering matter. The simulation is made in three cases as follows. I. Primary source can be directly observed. Both fluorescent X-rays and incident (not absorbed) X-rays are seen. II. X-rays from primary source are also absorbed by surrounding matter. III. Primary source is hidden or scattering matter is irradiated by an external source. Only fluorescent X-rays are observed.

5.2 Sgr C

In the opposite side of the Sgr B2, there is the other giant molecular cloud at the Sgr C region. The cloud is also heavy of about 10^6 $M_\odot$, and we call the cloud the Sgr C cloud in this thesis (section 2.3).

5.2.1 *ASCA* Observation

ASCA observed the Sgr C region on October 4 1993 in PV phase. The net observed time is about 20 ksec (section 4.1). The results are already published in Murakami et al. (2001).

6.4-keV line image

We made a narrow energy band image with a central energy of 6.4 keV and a width of twice the energy resolution (FWHM): 5.8–7.0 keV for the GIS. Figure 5.6 shows the GIS image overlaid with the contour map of the density distribution of the cold cloud by the radio observation of CS with the radial velocity of -120 km s^{-1} to -110 km s^{-1} (Figure 3 in Tsuboi, Handa, & Ukita 1999). The position accuracy is about $5''$ for the radio map, and $24''$ for the GIS image (Gotthelf et al. 2000) The 6.4 keV band image shows an X-ray peak (inner region of the solid circle) near the molecular cloud core CO 359.4+0.0 (Oka et al. 1998), which is one of the giant molecular clouds in the Sgr C complex, with a mass of $\sim 10^6$ $M_\odot$. We therefore suspect that the X-ray emission is associated with the molecular cloud Sgr C.

Spectrum

We made X-ray spectrum using the X-ray photons in a circle of $2'.7$ radius around the X-ray peak (see Figure 5.6). The background region is selected as a $2'.7$ radius region with the same Galactic latitude (dotted circle in Figure 5.6).

Figure 5.7 shows the background subtracted GIS spectrum. We fit the spectrum with a power-law continuum and a Gaussian line model. Due to the limited statistics, we fixed the power-law photon index Γ to be 2.0, the same value as assumed for Sgr B2. The fit is acceptable, with the best-fit parameters shown in Table 5.4. The central energy of the line appears at $6.28^{+0.15}_{-0.21}$ keV, in agreement with the fluorescent line from neutral irons. The line equivalent width and absorption column density are both very large: ~ 0.8 keV and $1.3^{+0.3}_{-0.4} \times 10^{23}$ H cm^{-2}, respectively.

Since the Galactic diffuse background may not be uniform, we checked the ambiguity of

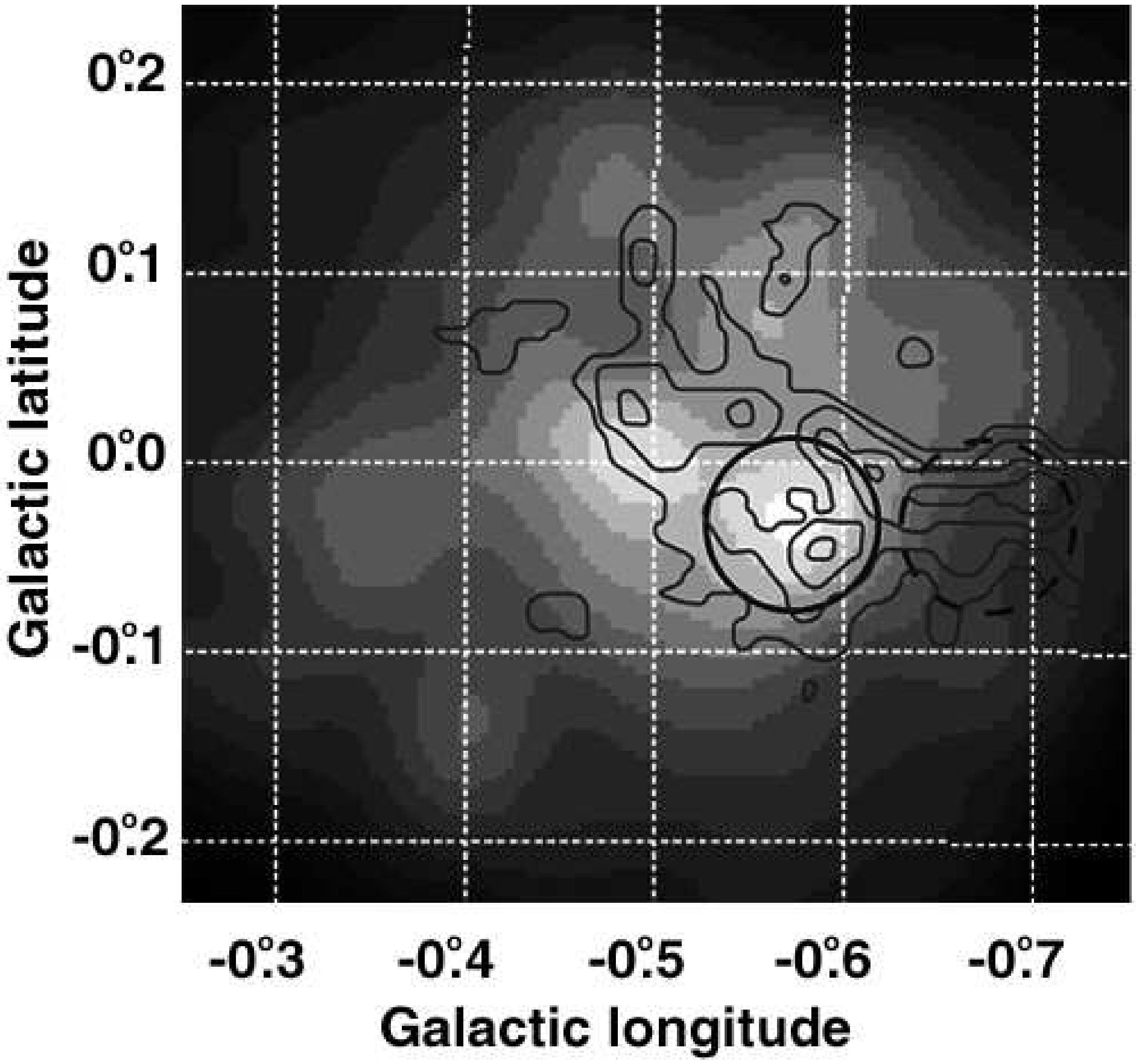

Figure 5.6: 6.4-keV line image of Sgr C. The contour shows the radio intensity distribution of CS with the radial velocity of -120 km s^{-1} to -110 km s^{-1} (Tsuboi, Handa, & Ukita 1999). The source and the background regions are shown by solid and dotted lines, respectively.

the background selection. We selected three other background regions with the same Galactic latitude as the source region, and fitted them with the same model. The best-fit parameters of the line central energy, line intensity, and the absorption are in the range of statistical errors. However, X-ray flux of the continuum component differs larger than the error. The 2.0–10.0 keV flux varies 12–38 $\times 10^{-5}$ photons s^{-1} cm^{-2}. Thus the continuum flux has large uncertainty by the background selection, however, since we are generally interested in the iron line flux, this flux variation is not serious.

Adding two narrow Gaussian lines at 6.4 and 6.7 keV on a power-law continuum, we found that the 6.7-keV line from highly ionized iron is very weak; the upper limit of 9 $\times 10^{-14}$ erg s^{-1} cm^{-2} is about 1/4 of the best-fit value of the 6.4-keV line. We thus conclude that the emission line from the Sgr C cloud is dominated by the fluorescent line from cold irons.

We also made an SIS spectrum from the same region of GIS, and fitted it with the same model as with the GIS. The best-fit spectral parameters are shown in 5.4, and are consistent with those obtained from the GIS spectrum. Due to the limited statistics, the SIS spectrum does not further constrain the spectral parameters.

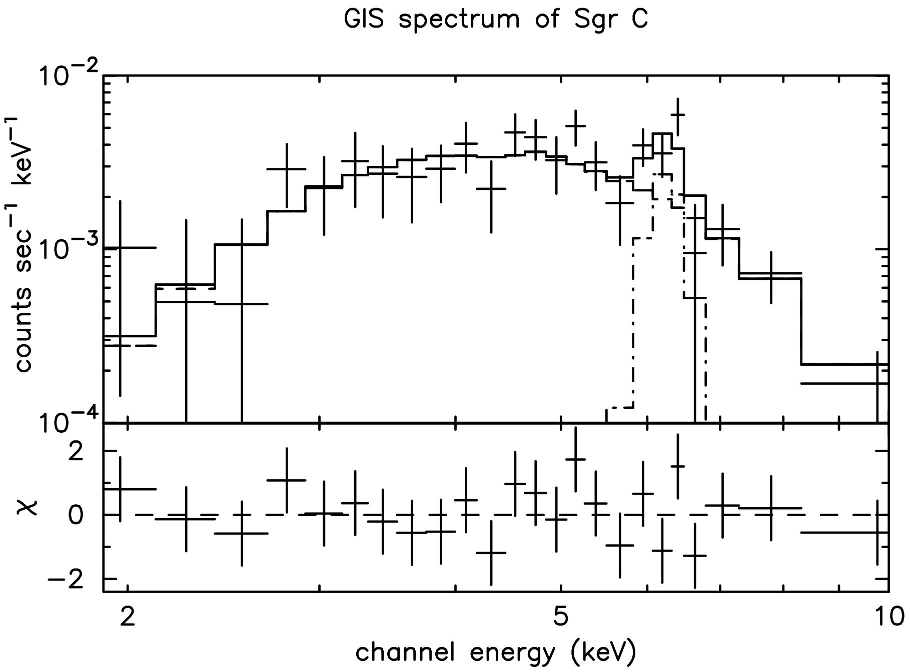

Figure 5.7: The GIS spectrum of Sgr C. The best-fit model is shown by solid line

Table 5.4: Best-Fit Results of the X-ray Spectrum of Sgr C obtained with *ASCA*.

	Continuum			Iron line				
	N_H[a]	Γ[b]	F_X[c]	E_C^d	F_X[c]	EW[e]	L_X[f]	χ^2/d.o.f.
GIS	$12.6^{+3.5}_{-3.3}$	2.0 (fixed)	30^{+9}_{-6}	$6.28^{+0.15}_{-0.21}$	$3.5^{+1.4}_{-2.2}$	$0.8^{+0.4}_{-0.5}$	$5.0^{+1.3}_{-1.0}$	16.1/20
SIS	$9.7^{+3.9}_{-2.5}$	2.0 (fixed)	20^{+7}_{-5}	$6.38^{+0.10}_{-0.31}$	$2.7^{+2.3}_{-1.5}$	$1.1^{+1.1}_{-0.7}$	$3.0^{+0.9}_{-0.8}$	8.9/14

[a] : Hydrogen column density [10^{22}H cm^{-2}].

[b] : Photon index of a power-law model for the continuum spectrum.

[c] : Flux (no correction of absorption) in the 4–10 keV band [10^{-5}photons cm^{-2} s^{-1}].

[d] : Center energy of iron line [keV].

[e] : Equivalent width of iron line [keV].

[f] : Absorption corrected luminosity in the 4–10 keV band [10^{34}erg s^{-1}].

5.2.2 *Chandra* Observation

Sgr C region is observed twice with *Chandra* as a part of the Galactic center survey (section 4.2). The net observing time is about 20 ksec.

6.4-keV line image

We first applied the "wavdetect" method to the 3–8 keV image to remove a contamination of point sources, and detected 37 point sources in the $17' \times 17'$ field. Since no point sources are found around the molecular cloud, we simply exclude X-rays from point sources within the diameter of twice of the PSF size, and smoothed with Gaussian function of $\sigma = 16''$ to investigate a distribution of diffuse emissions. Figure 5.8 shows the smoothed image superposed with radio intensity of the CS line (Tsuboi, Handa, Ukita 1999).

The diffuse X-ray emission is detected at (l =359$^\circ\!\!.$4–359$^\circ\!\!.$5, $b = -0^\circ\!\!.1$–$0^\circ\!\!.0$), which is almost the same position as *ASCA* observation. The distribution of X-ray intensity has a crescent shape which is symmetric to Sgr B2 with respect to the GC, and at the Galactic center side of the cloud core. Note that the radio image is sliced in radial velocity, and we cannot estimate accurate separation between the X-ray peak and the cloud core.

There is another diffuse filamentary structure at (359$^\circ\!\!.$42, $-0^\circ\!\!.13$), which is near the faint emission detected by BeppoSAX (Sidoli et al. 2001). The nature of this emission is discussed in section 7.2.2. Other three bright spots at (l, b) = (359$^\circ\!\!.$32, 0$^\circ\!\!.$06), (359$^\circ\!\!.$39, 0$^\circ\!\!.$01) and (359$^\circ\!\!.$55, 0$^\circ\!\!.$01) are contamination of bright point sources.

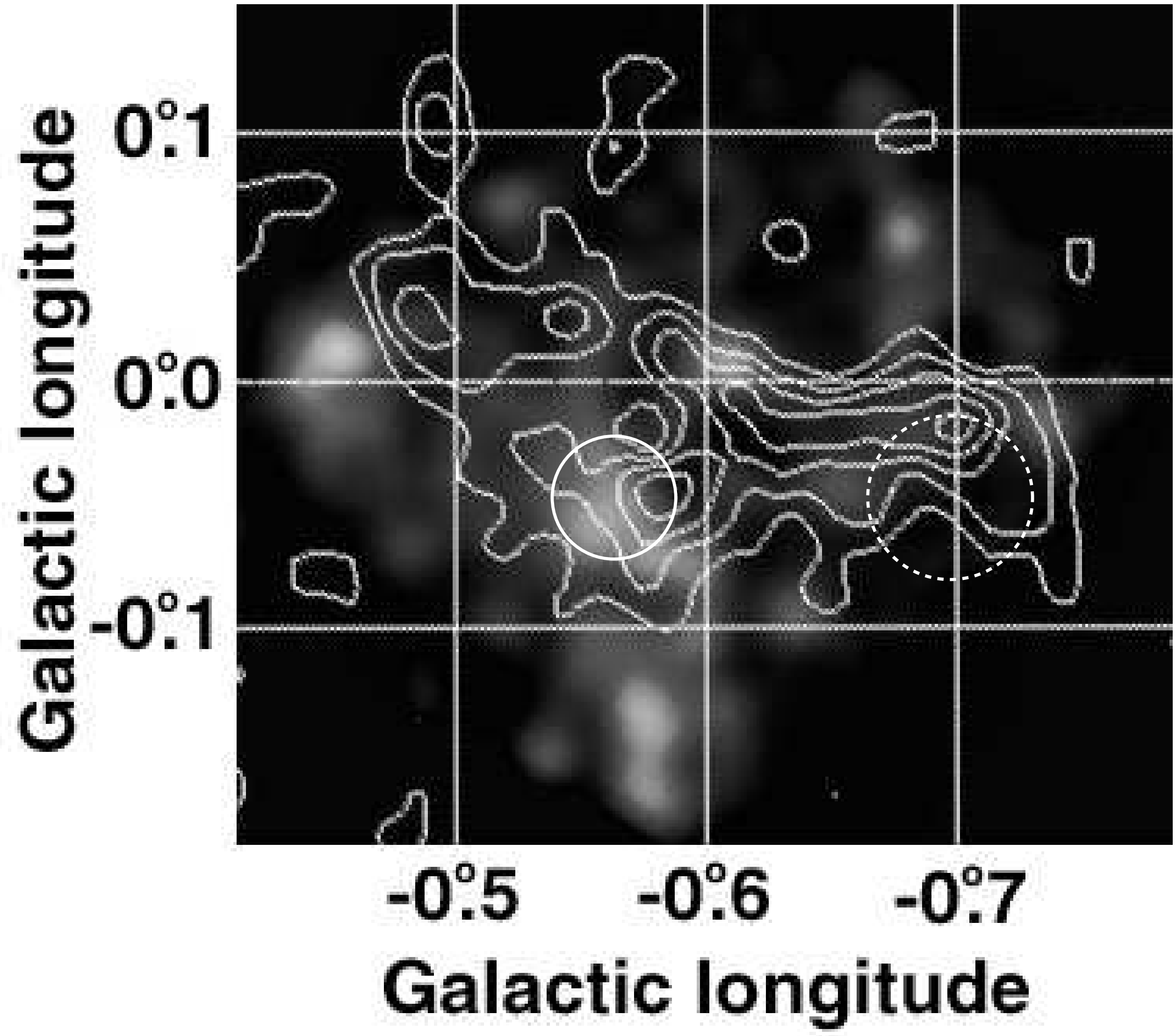

Figure 5.8: *Chandra* image of Sgr C obtained with ACIS. The contour shows the radio intensity distribution of CS with the radial velocity of -120 km s^{-1} to -110 km s^{-1} (Tsuboi, Handa, & Ukita 1999). The source and the background regions are shown by solid and dotted lines, respectively.

spectrum

We accumulated X-rays from the circular region indicated by the solid line in Figure 5.8, and make a spectrum. No point source is detected in this region with the 3.0–8.0 keV band image. The background spectrum is obtained from the other $2'$-radius circle at the same Galactic latitude (dotted circle in Figure 5.8). The spectrum is shown in Figure 5.9. There are large excesses at ~ 6.4 and ~ 7.1 keV, which are the center energies of Kα and Kβ lines of neutral iron. We then fit the spectrum with a power-law and two narrow Gaussian lines with the fixed ratio of the center energy and the intensity. We fixed a photon index of the power-law model to be 2.0 as Sgr B2. The best-fit parameters are shown in Table 5.5.

The strong neutral iron is detected with the equivalent width of ~ 3.2 keV. The absorption of 13.8×10^{22} H cm^{-2} is slightly larger than the Galactic interstellar absorption (Sakano 2000; see section 5.5.1). X-ray flux is smaller than *ASCA* results. It would be attributable to smaller size of source region ($\sim 1/4$) and difference in background region.

We further fit the spectrum adding 6.7-keV line. The equivalent width is constrained to be < 260 eV.

Table 5.5: Best-Fit Results of the X-ray Spectrum of Sgr C Obtained with *Chandra*.

	Continuum			Iron line							
	$N_{\rm H}$[a]	Γ[b]	$F_{\rm X}$[c]	$E_{\rm C}$[d]	$F_{\rm X}$[c]	EW[e]	$E_{\rm C}$[d]	$F_{\rm X}$[c]	EW[e]	$L_{\rm X}$[f]	χ^2/d.o.f.
ACIS	$13.8^{+14.2}_{-5.9}$	2.0 (fixed)	29 ± 13	$6.38^{+0.06}_{-0.29}$	14^{+6}_{-7}	3.2 ± 1.5	$7.04^{+0.06}_{-0.32}$	2.0 ± 0.9	$0.5^{+0.3}_{-0.2}$	$6.4^{+7.8}_{-3.6}$	10.4/13

[a] : Hydrogen column density [10^{22}H cm^{-2}].

[b] : Photon index of a power-law model for the continuum spectrum.

[c] : Flux (no correction of absorption) in the 2–10 keV band [10^{-6}photons cm^{-2} s^{-1}].

[d] : Center energy of iron line [keV].

[e] : Equivalent width of iron line [keV].

[f] : Absorption corrected luminosity in the 2–10 keV band [10^{33}erg s^{-1}].

5.2.3 Discussion

Comparison with radio observations

In the radio continuum band, the most distinct features are H$_{\rm II}$ regions and non-thermal filaments. However, no X-ray peak agrees with the radio filament. The filamentary structure in

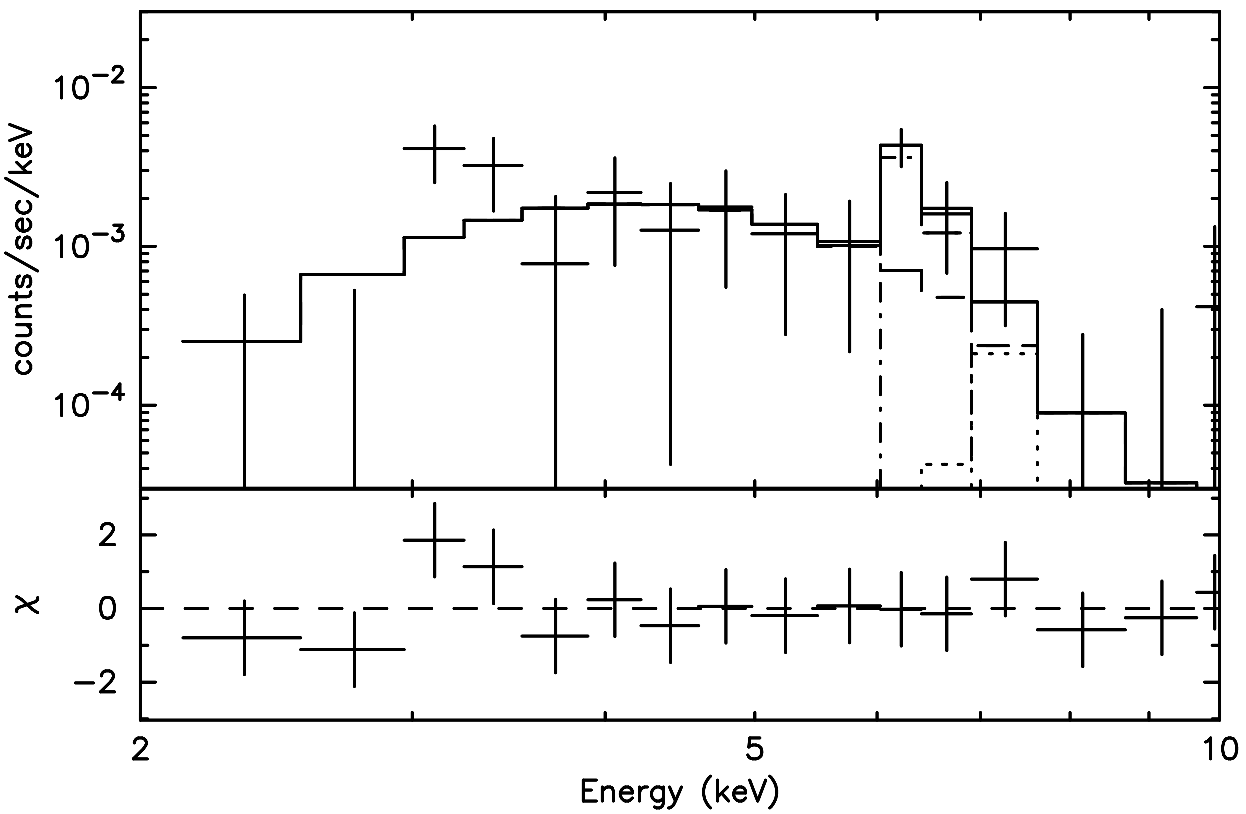

Figure 5.9: *Chandra* spectrum of Sgr C with the best-fit spectrum in solid line.

Figure 5.8 is slightly shifted from the radio filament. While the distribution of the molecular cloud agree with the 6.4-keV line emission.

Emission mechanism

We detected a diffuse X-ray emission from the molecular cloud near Sgr C. Strong neutral iron lines and large absorption column are confirmed. The X-ray image resembles Sgr B2; the peak is shifted to GC side. No point source is detected in the cloud, which clearly rejects the internal point source origin. With the similarity of Sgr B2, the molecular cloud is a candidate for an XRN.

The detailed verification of the XRN model is mentioned in section 5.5.

5.3 M0.11−0.08

M0.11−0.08 is a molecular cloud near the Radio Arc, and the nearest giant molecular cloud to the Galactic center. Koyama et al. (1996) already reported the detection of strong neutral iron line around here with *ASCA*. In this section, we further study the X-ray spectrum and distribution by long exposure observation with *ASCA* and *Chandra*.

5.3.1 *ASCA* Observation

After the discovery of the 6.4-keV line emission in the PV phase (Koyama et al. 1996), we made follow-up observation of the Radio Arc region $\sim$ 80 ksec with *ASCA* (section 4.1).

6.4-keV line image

Figure 5.10 shows the 5.8–7.0 keV image in the Radio Arc region with 80 ksec exposure. There is a faint peak at $(l, b) \simeq (0.^\circ1,\ -0.^\circ1)$ as shown by solid white circle, which agrees with the position of the bright spot seen in the brightness distribution map of the 6.4-keV line with early observation in Koyama (1996) (see Figure 2.9).This position is also coincident with M0.11−0.08. However, the detailed comparison with the distribution of molecular cloud is made by using the *Chandra* image in the next subsection.

spectrum

We make a spectrum with the source region of $3'$-radius circle. To exclude the contamination from the Sgr A region, the background region is determined to be another $3'$-radius circle which

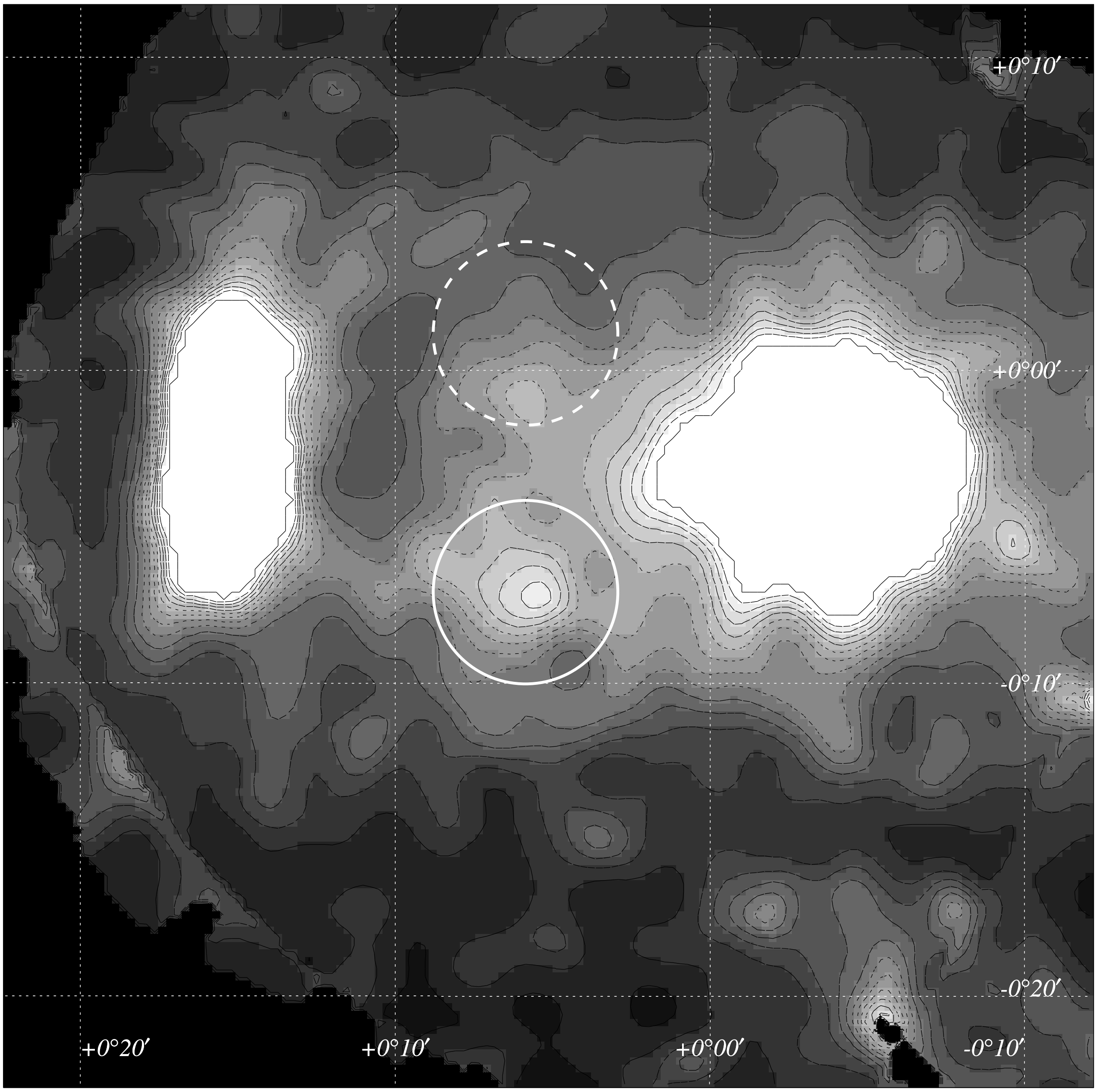

Figure 5.10: *ASCA* GIS image of the Radio Arc region in 5.8–7.0 keV band. Bright spot is shown by solid circle. The dashed line shows the background region. Two white regions are saturated with the bright X-ray sources: 1E 1743.1−2843 (left) and Sgr A region (right).

is symmetric in regard to the Galactic latitude of Sgr A*. The source and the background regions are shown in solid and dashed lines respectively, in Figure 5.10. The spectrum exhibits strong iron line at ~ 6.4 keV (Figure 5.11).

We first fit the spectrum with a power-law and a Gaussian line with the free center energy and width. Though the spectrum is roughly fitted with the best-fit values of photon index $\Gamma \sim 1.9$, the center energy of Gaussian $E_{\mathrm{C}} \sim 6.43$ keV, and the equivalent width of ~ 2.3 keV, it is not acceptable with the χ^2 of 35.4 (24 d.o.f.). There are residuals at ~ 1.9 keV (He-like Si), ~ 2.5 keV (He-like S), and ~ 3.1 keV (He-like Ar). These features indicate that the spectrum contains thermal component. The width of Gaussian is also large with the σ of ~ 300 eV, which implies that the iron line is a blend of neutral and ionized states.

A single thin-thermal plasma model also cannot reproduce the spectrum with a large residual at ~ 6.4 keV and the χ^2 of 50.9 (27 d.o.f.). Then we fit the spectrum with a thin-thermal plasma model and a simple XRN model used for Sgr B2 and Sgr C (a power-law and two Gaussian lines of iron Kα and Kβ). To convergence the fitting, we fixed the abundance of the thermal plasma to be 1.0, the photon index of the power-law to be 2.0 (same as Sgr B2), and equivalent width of lines to be 2.0 for Kα as the expected value in Inoue (1985). The center energies and the intensity ratio of iron lines are fixed to be the laboratory values.

At first we determine the parameters of thermal component with the spectrum of 1.0–3.5 keV band. Since XRN ordinary exhibits large absorption column and very weak X-ray emission in low energy band, the thermal component is dominant in this band. We obtain acceptable fittings with best-fit parameters and χ^2 of $kT = 2.8$ (> 1.2) keV, $N_{\mathrm{H}} = 5.1^{+2.9}_{-2.1} \times 10^{22}$ H cm^{-2}, and χ^2/d.o.f $= 15.4/10$. Although there still left residuals at ~ 1.9 keV and ~ 3.1 keV, reduced χ^2 becomes worse if we fit the spectrum with the abundance variable.

We fixed the temperature and the absorption column to be these values, and fit the 1.5–10 keV band adding the simple XRN model. The normalization of the thermal component is treated as variable. We then obtain acceptable fittings. Best fit values are shown in Table 5.6. We confirmed the strong neutral iron line. Though the center energy of the line is slightly smaller than 6.4 keV, it should be due to systematic uncertainty of detector or fitting method (affected by the thermal component).

We thus conclude that M0.11$-$0.08 also emits strong 6.4-keV line with the equivalent width of ~ 2.0 keV, though there is another component of thin-thermal plasma.

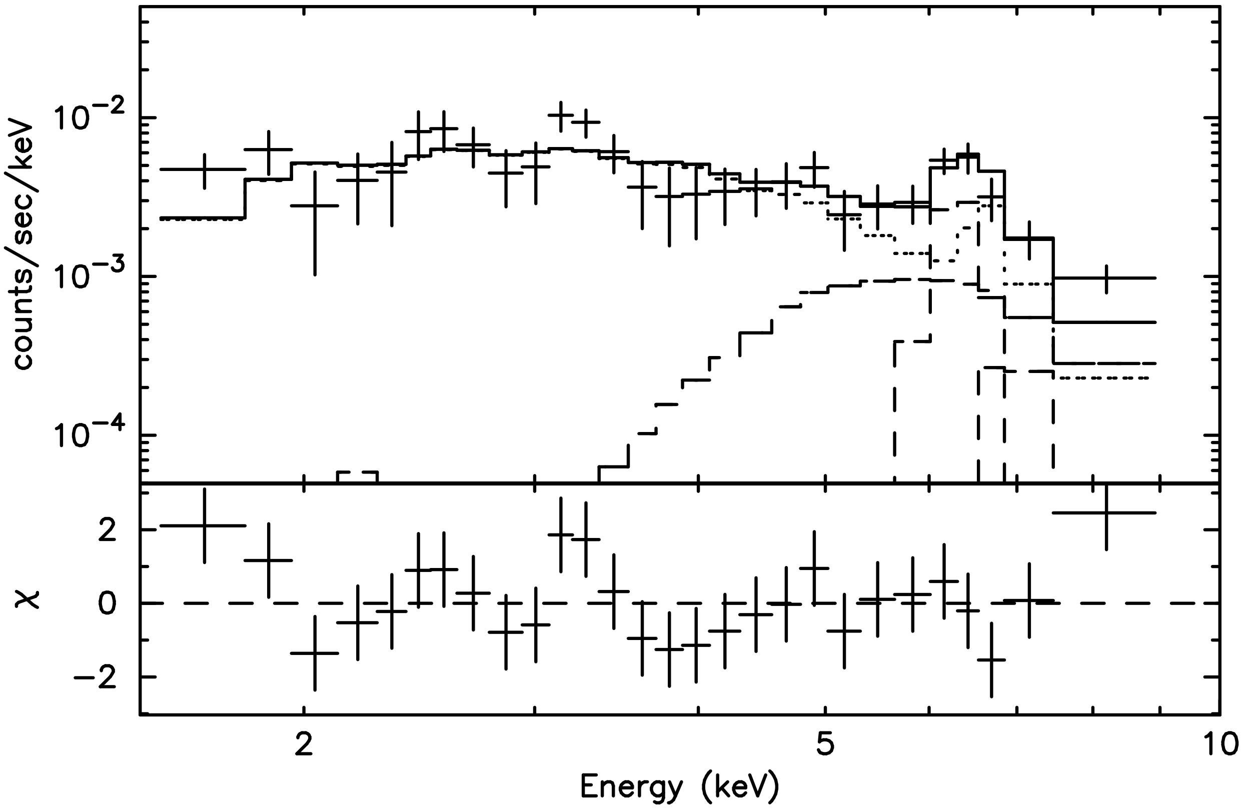

Figure 5.11: The X-ray spectrum of M0.11−0.08 obtained with *ASCA*. The solid line shows the best-fit spectrum, of which dotted line shows the thermal component and dashed lines show the simple XRN model (power-law and Kα, Kβ lines of neutral iron).

Table 5.6: Best-Fit Results of the X-ray Spectrum of M0.11−0.08 obtained with *ASCA* GIS

(thermal component)				
N_H [a]	kT [b]	Z [c]	F_X [d]	L_X [e]
5.1 (fixed)	2.8 (fixed)	1.0 (fixed)	34^{+3}_{-4}	3.1±0.4

(simple XRN model)									
	Continuum		Iron lines						total
			Kα			Kβ			
N_H [a]	Γ [f]	F_X [d]	E_C [g]	F_X [d]	EW [h]	E_C [g]	F_X [d]	EW [h]	L_X [e]
$54.7^{+20.3}_{-17.3}$	2.0 (fixed)	8.4±2.1	$6.28^{+0.08}_{-0.14}$	$3.7^{+1.0}_{-0.9}$	2.0 (fixed)	$6.93^{+0.08}_{-0.16}$	$0.7^{+0.1}_{-0.2}$	0.3 (fixed)	$5.4^{+1.4}_{-1.5}$
							χ^2/d.o.f.	···	33.6/26

[a] : Hydrogen column density [10^{22}H cm^{-2}].

[b] : The temperature of the plasma [keV].

[c] : Chemical abundance with ratio to solar abundance.

[d] : Flux (no correction of absorption) in the 2–10 keV band [10^{-5}photons cm^{-2} s^{-1}]. [e] : Absorption corrected luminosity in the 2–10 keV band [10^{34}erg s^{-1}].

[f] : Photon index of a power-law model for the continuum spectrum.

[g] : Center energy of iron line [keV].

[h] : Equivalent width of iron line [keV].

5.3.2 *Chandra* Observation

Chandra observed the Radio Arc region about 50 ksec in August 2000 (Section 4.2), which is including the molecular cloud M0.11−0.08.

Image

Figure 5.12 shows the 6.0–7.0 keV image obtained with *Chandra*, which is adaptively smoothed with the same method as Sgr B2. We confirm the diffuse X-ray emission at $(l, b) \simeq (0^\circ.1, -0^\circ.1)$. In addition, several point sources and filamentary structures are also found. We extract the point sources by the "wavdetect" method in the 3–8 keV image, and detect 186 point sources in $17' \times 17'$ region.

The intensity distribution of CS line with the radial velocity of 20–30 km s^{-1} is laid on the X-ray image. The diffuse emission is roughly coincident with the dense cloud. A larger filamentary structure is at the edge of the GC side of the cloud (see section 7.2.1). Another filament is located at the opposite side of the cloud (see section 7.1.2). These filaments are shown by dashed elliptical region in Figure 5.12. They are distinct in 3.0–8.0 keV raw (not smoothed) image (Figure 7.1, 7.4b, 7.5b).

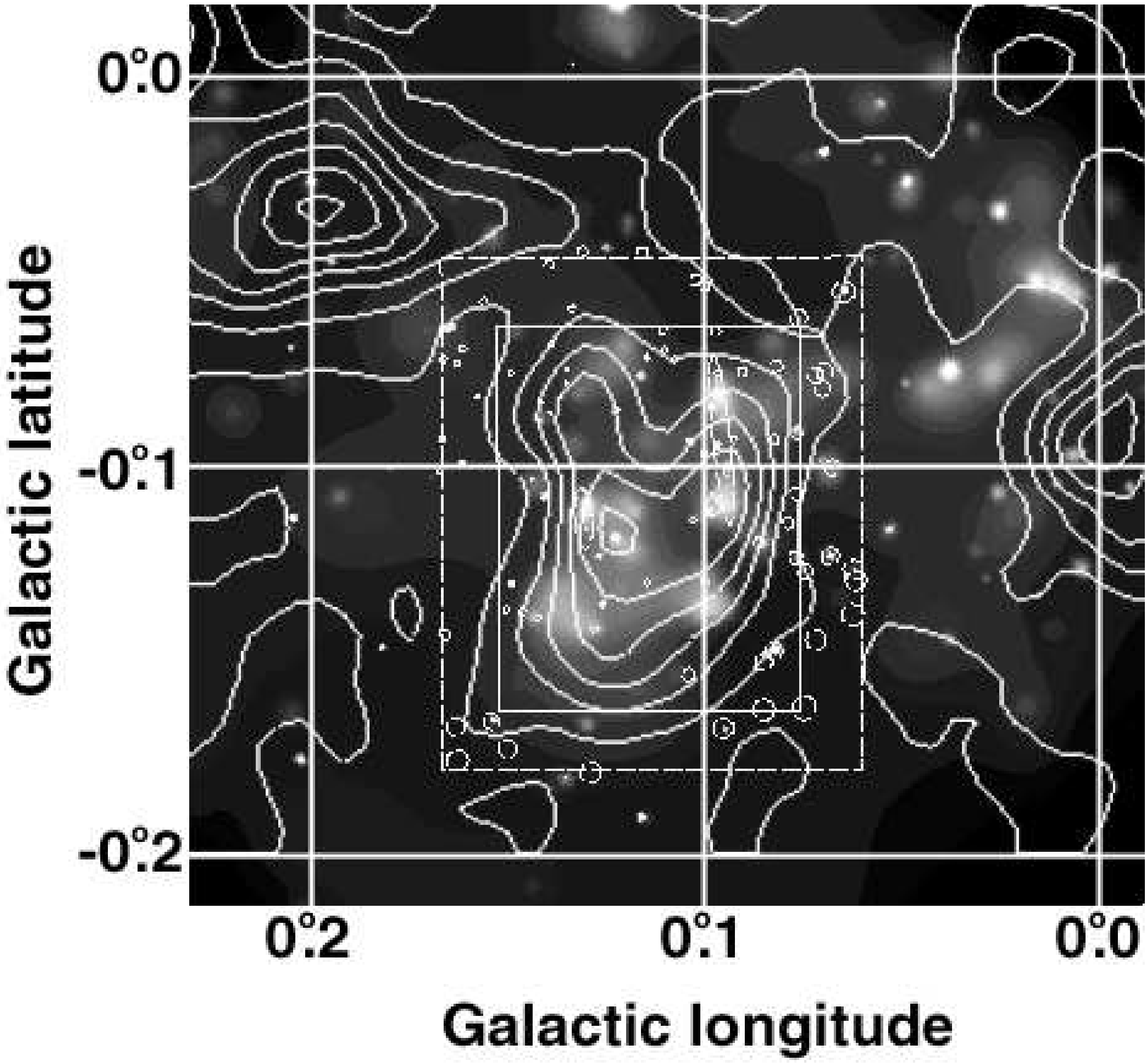

Figure 5.12: 6–7 keV image around M0.11−0.08 obtained with *Chandra*. Point sources are shown by circles, and two filamentary structures are indicated by ellipses. Contour shows the CS line intensity with the radial velocity of 20 km s^{-1} to 30 km s^{-1} (Tsuboi, Handa, & Ukita 1999). The source and the background regions are shown by solid and dashed lines.

spectrum

Since we revealed that the diffuse emission is coincident with the molecular cloud, we extract X-rays from the rectangle region of $6' \times 4\overset{\prime}{.}7$ enclosing the cloud. The contamination of point sources and filaments are excluded. Background region is surrounding rectangle of the source region. The source and background regions are shown in Figure 5.12. We fit the spectrum with the same model as *ASCA*. Since the energy resolution of ACIS is better than GIS, we fit the spectrum with the parameters of a thermal and a simple XRN components variable. We obtain acceptable fittings with χ^2/d.o.f. of 26.7/25. The best-fit parameters are shown in Table 5.7. Figure 5.13 shows the spectrum and best-fit model in solid line. The thermal and the simple XRN components are shown in dotted and dashed lines respectively. The parameters of thermal component are almost the same as *ASCA* results. We verified that the assumption in fitting analysis of *ASCA* spectrum is valid. We also confirmed that the simple XRN model can reproduce the spectrum. The absorption column of XRN component is also large as other clouds.

We also fit the combined spectrum of resolved point sources. The total luminosity of point sources is $\sim 2 \times 10^{34}$ erg s^{-1}, which is smaller than that of XRN component.

Table 5.7: Best-Fit Results of the X-ray Spectrum of M0.11−0.08 Obtained with *Chandra*.

(thermal component)				
$N_{\rm H}$[a]	kT[b]	Z[c]	$F_{\rm X}$[d]	$L_{\rm X}$[e]
$6.9^{+1.0}_{-0.7}$	$2.8^{+0.7}_{-0.5}$	1.0 (fixed)	30^{+3}_{-2}	$3.4^{+0.4}_{-0.3}$

(simple XRN model)									
Continuum			Iron lines						total
			Kα			Kβ			
$N_{\rm H}$[a]	Γ[f]	$F_{\rm X}$[d]	$E_{\rm C}$[g]	$F_{\rm X}$[d]	EW[h]	$E_{\rm C}$[g]	$F_{\rm X}$[d]	EW[h]	$L_{\rm X}$[e]
$23.5^{+10.3}_{-7.5}$	2.0 (fixed)	21±2	$6.36^{+0.01}_{-0.03}$	7.7±0.8	2.0 (fixed)	$7.01^{+0.02}_{-0.03}$	$1.2^{+0.1}_{-0.2}$	0.3 (fixed)	$6.1^{+0.7}_{-0.6}$
							χ^2/d.o.f.	···	26.7/25

^{a} : Hydrogen column density [10^{22}H cm^{-2}].

^{b} : The temperature of the plasma [keV].

^{c} : Chemical abundance with ratio to solar abundance.

^{d} : Flux (no correction of absorption) in the 2–10 keV band [10^{-5}photons cm^{-2} s^{-1}]. ^{e} : Absorption corrected luminosity in the 2–10 keV band [10^{34}erg s^{-1}].

^{f} : Photon index of a power-law model for the continuum spectrum.

^{g} : Center energy of iron line [keV].

^{h} : Equivalent width of iron line [keV].

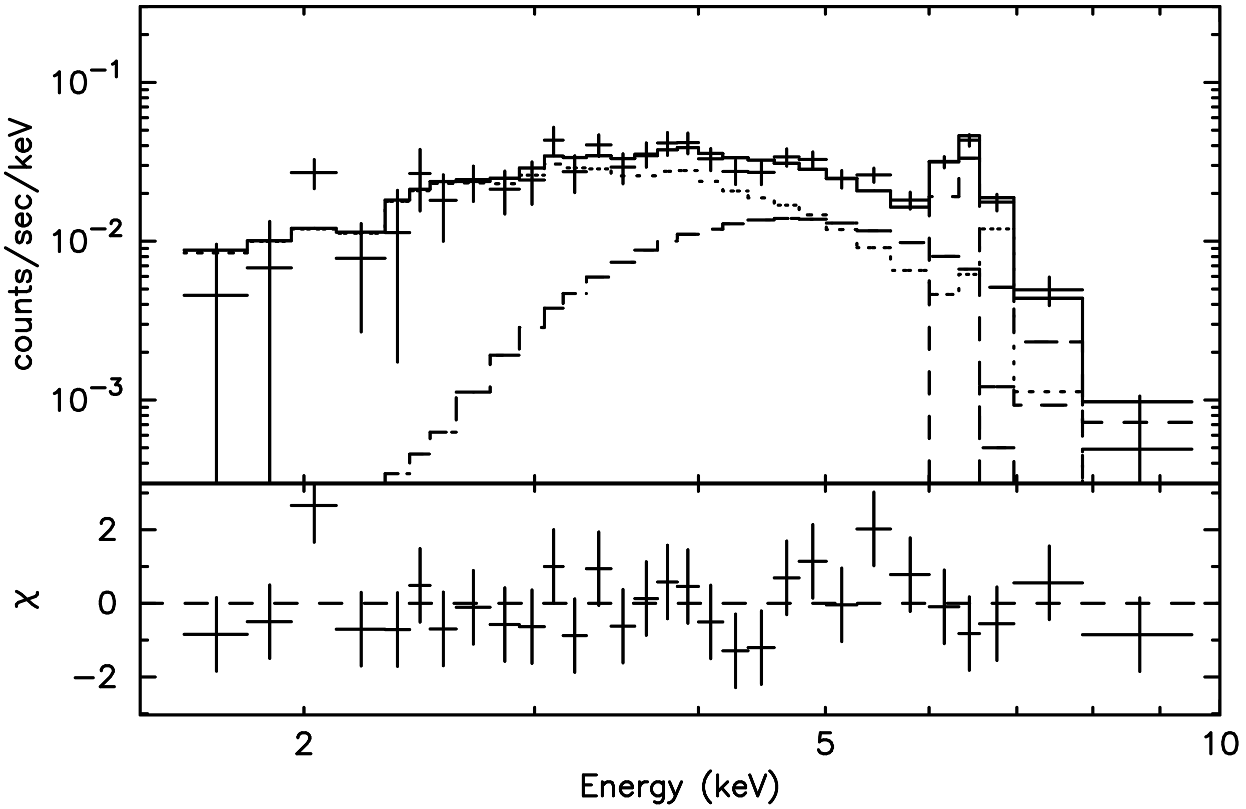

Figure 5.13: The X-ray spectrum of M0.11−0.08 obtained with *Chandra*. The best-fit spectrum is shown by solid line. The dotted line shows the thermal component, and the dashed lines show the simple XRN spectrum (a power-law with two narrow lines of neutral iron Kα and Kβ).

5.3.3 Discussion

By the observations of *ASCA* and *Chandra*, we revealed that the X-ray spectrum of M0.11−0.08 exhibits strong 6.4-keV line. Though there is also a thermal component, fluorescent X-rays should be emitted from the cloud. By using the simple XRN model, we can reproduce the spectrum. It is possible that M0.11−0.08 is also an XRN. This hypothesis is further verified with numerical simulations in section 5.5.

5.4 Clump 2

Clump 2 is a large molecular cloud at $(l, b) = (2.^\circ7\text{–}3.^\circ4, 0.^\circ0\text{–}0.^\circ8)$ (Stark&Bania 1986). The molecular cloud consists of a lot of cores with the total mass of 3×10^6 $M_\odot$ (section 2.3).

5.4.1 *ASCA* Observation

Maeda (1998) revealed the excess of 6.4-keV line in this field with *ASCA* Galactic plane survey. The Galactic longitudinal distribution of 6.4-keV line decreases with the larger longitude, but exhibits a bump at $l \sim 3^\circ$ (Figure 5.14). This region includes the Clump 2 cloud.

The 6.4-keV line and the large molecular cloud are common features in XRN, then we made a follow-up observation with *ASCA* in 1999 July. We concentrate the results of the follow-up observation in this section. The observed time is about 80 ksec (section 4.1).

6.4-keV line image

Figure 5.15 shows the 5.8–7.0 keV image. This field is located near GX 3+1, and the stray light contaminates the upper-right part of the image ($l \gtrsim 0.^\circ0$). There is no other distinct emission.

We then made the equivalent width map by the same method in Sakano (2000). Figure 5.16 shows the distribution of the equivalent width of the iron line. The excess is detected at $(l, b) \simeq$ ($0.^\circ0$, $2.^\circ7$). The X-ray peak is located at the GC side of the main body of Clump 2, and rather agrees with the envelope gas than a dense core (Figure 2.7). Photon statistics and the angular resolution is insufficient to make a detailed comparison between X-ray and radio image.

spectrum

We extract X-rays from the $4'$-radius circular region, and subtracted a background spectrum obtained from the annulus with the radius of $4'$–$6'$ (solid and dashed circles in Figure 5.16).

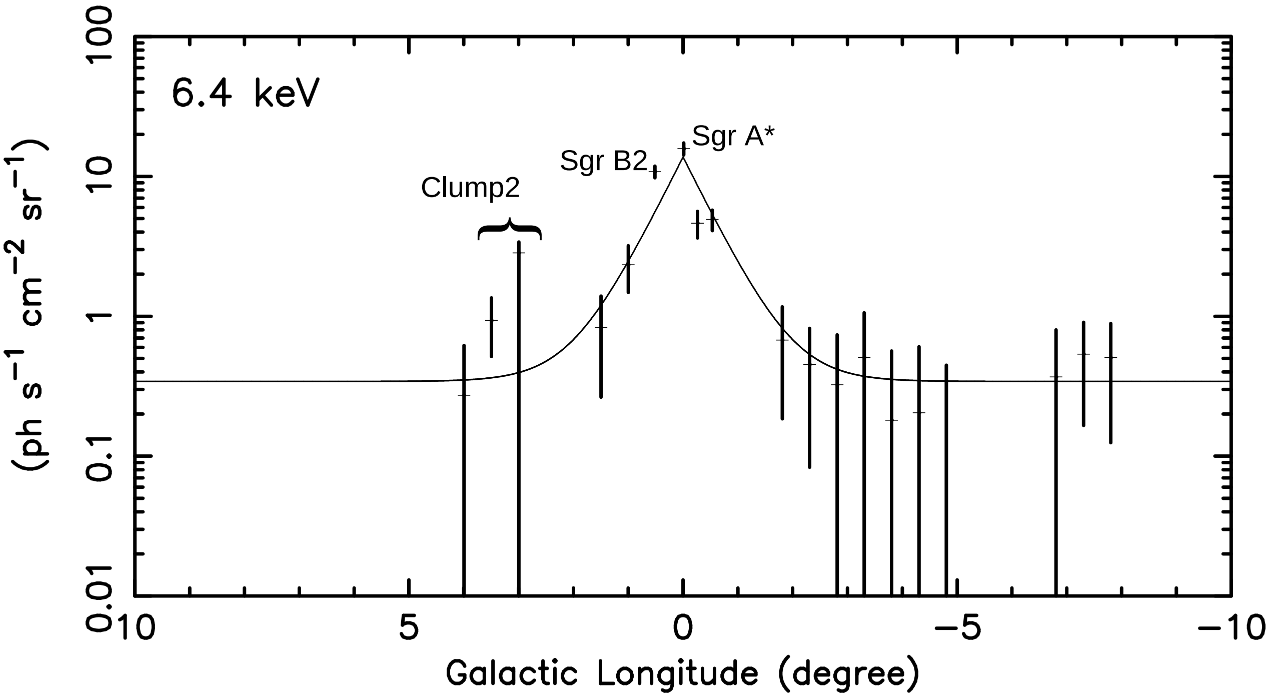

Figure 5.14: Intensity distribution of the iron neutral line in the GC region (Maeda 1998).

Figure 5.17 shows the spectrum. We fit the spectrum with a phenomenological model of a power-law and a Gaussian line. This model cannot reproduce the spectrum with the large reduced χ^2 of 1.85 (6 d.o.f.). Though we confirmed the strong iron line, we cannot limit the ionization state with the large error of the center energy of 6.21–6.95 keV. The equivalent width of the line is $\sim$ 5.9 keV. There is a residual at $\gtrsim$ 7.0 keV. We also fit the spectrum with a thin thermal plasma model. The abundances of elements are varied with the fixed ratio to the solar values. This model is rejected with the reduced χ^2 of 1.87 (7 d.o.f.). There is a large residual at 6–7.5 keV, or the strong iron line can not be reproduced with the thermal model.

We then fit the spectrum with a power-law model and two narrow Gaussian lines with the fixed center energies of iron Kα and Kβ (simple XRN model; see previous sections). The center energies and intensity ratio of iron lines are fixed to the laboratory values. We obtain better fitting with the reduced χ^2 of 1.73 (7 d.o.f). This χ^2 value is slightly larger than 90% accepted region with the probability of 9.7%. If we fix the equivalent width of the iron line to be 2.0 keV, we can obtain acceptable fittings with the best-fit values shown in Table 5.8. Absorption column of $\sim$ 5 $\times 10^{22}$ H cm^{-2} is consistent with interstellar absorption (Sakano 2000; see section 5.5.1).

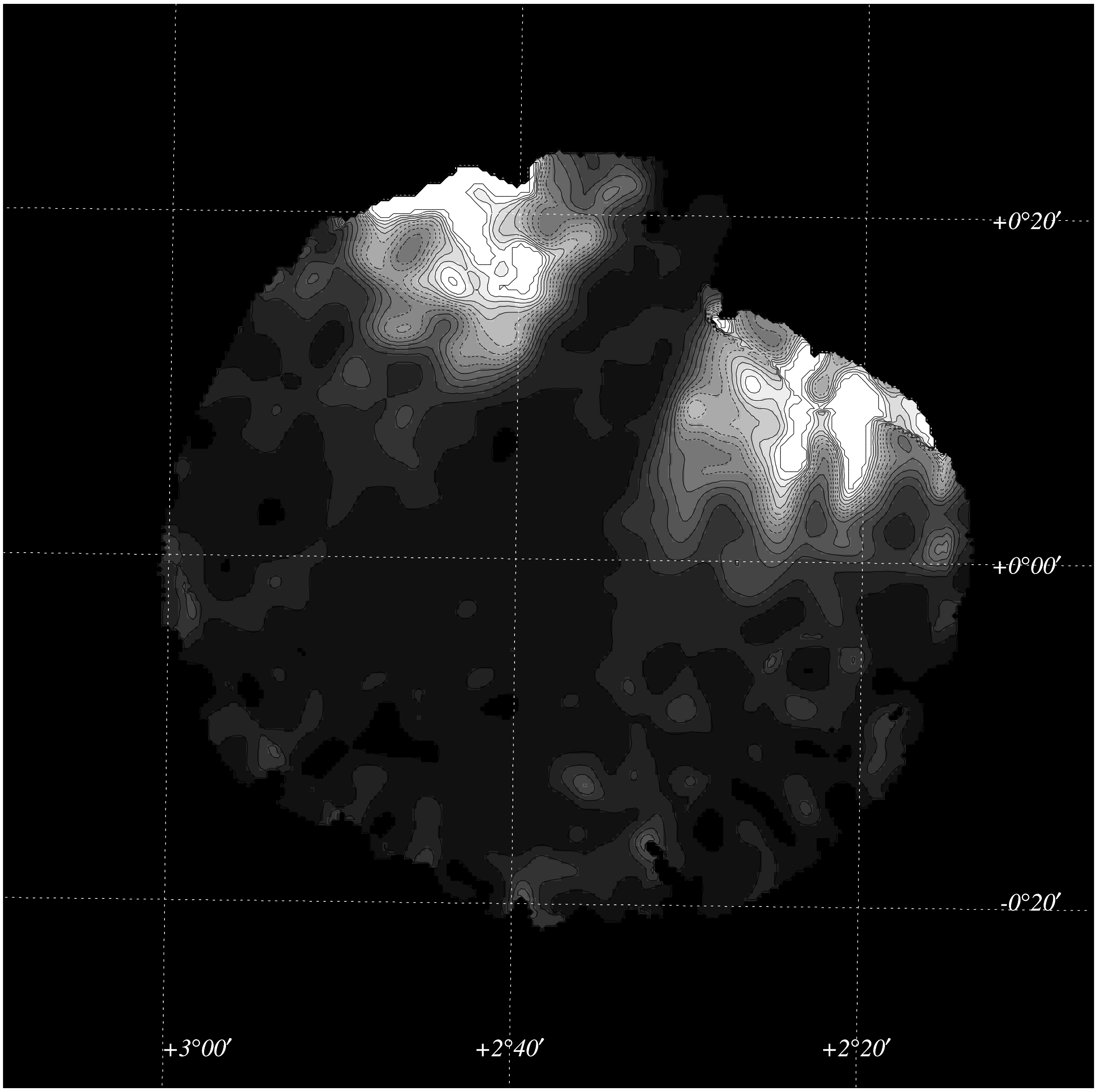

Figure 5.15: The 5.8–7.0 keV image of the Clump 2 region. The stray light of GX 3+1 is found in upper right.

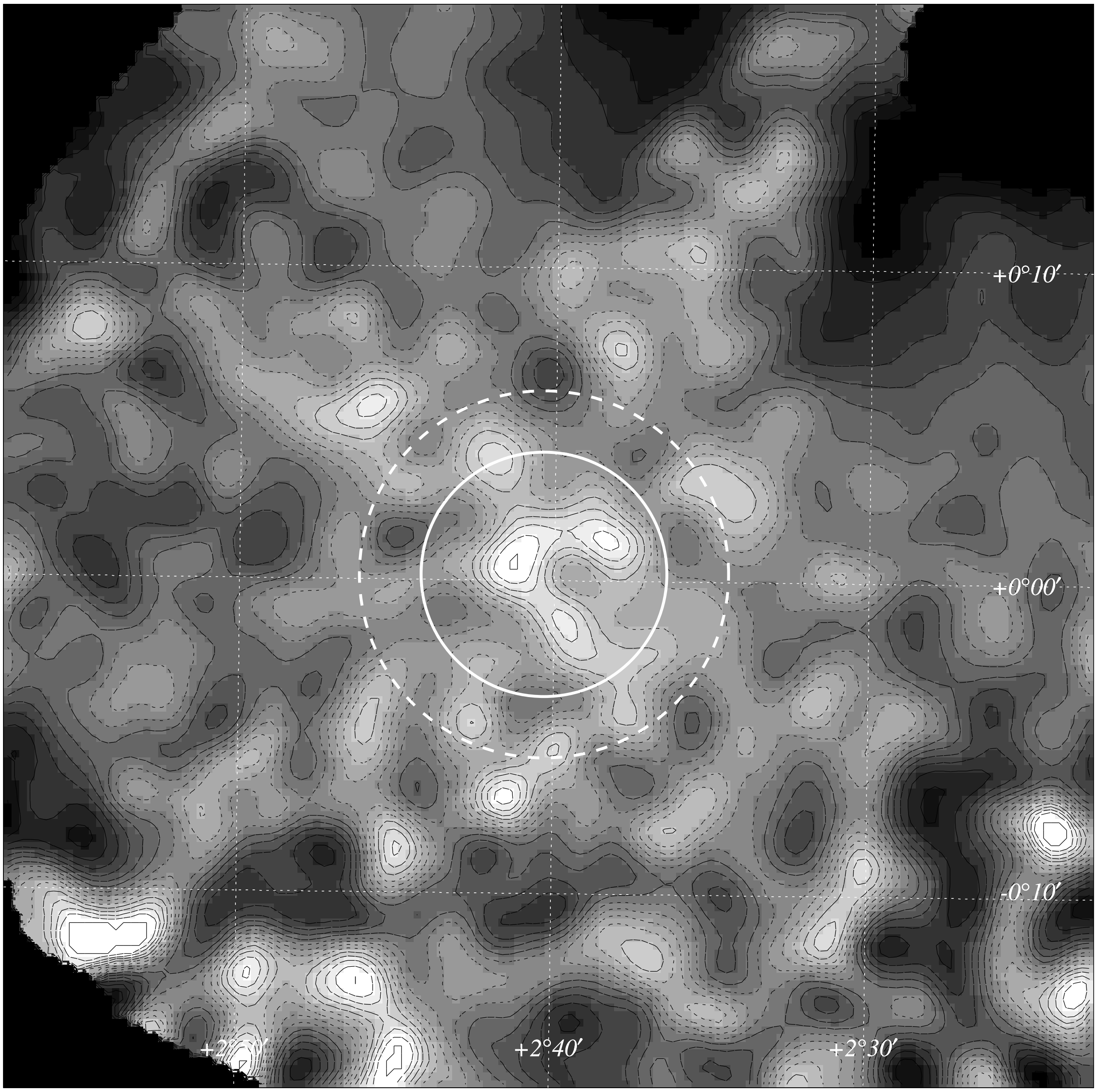

Figure 5.16: The distribution of the equivalent width of iron line on Clump 2 obtained with *ASCA*. Gray image shows the equivalent width of 0.0–2.0 keV in linear scale.

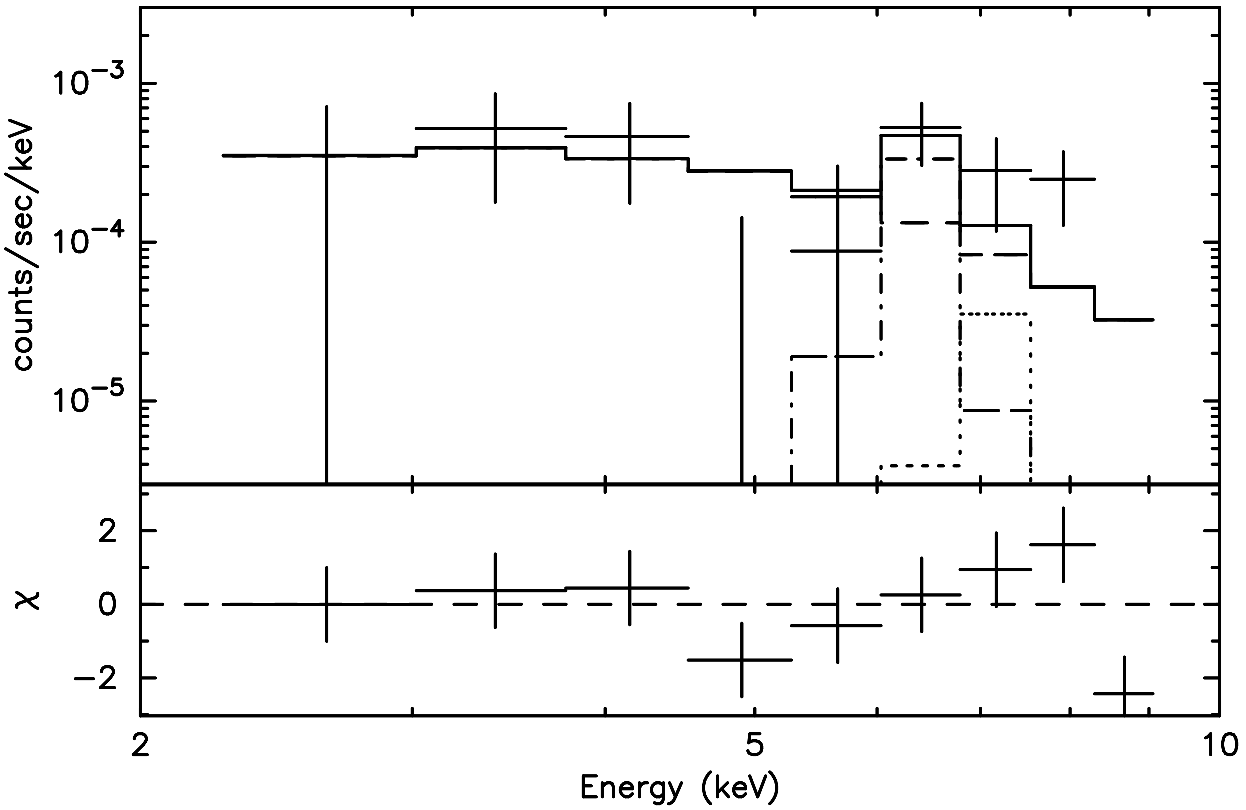

Figure 5.17: The X-ray spectrum of the diffuse X-ray emission at Clump 2 region. The solid line shows the best-fit spectrum with the simple XRN model.

Table 5.8: Best-Fit Results of the X-ray spectrum of Clump 2 obtained with *ASCA* GIS.

		Continuum				Continuum					
	$N_{\rm H}$ $^{\rm a}$	Γ $^{\rm b}$	$F_{\rm X}$ $^{\rm c}$	E $^{\rm d}$	$F_{\rm X}$ $^{\rm c}$	EW $^{\rm e}$	E $^{\rm d}$	$F_{\rm X}$ $^{\rm c}$	EW $^{\rm e}$	$L_{\rm X}$ $^{\rm d}$	χ^2/d.o.f.
GIS	$5.2^{+22.9}_{-3.7}$	2.0 (fixed)	22±11	6.40 (fixed)	$4.3^{+2.2}_{-2.1}$	2.0 (fixed)	7.06 (fixed)	0.6±0.3	0.3 (fixed)	$2.5^{+2.1}_{-1.4}$	12.4/8

^{a} : Hydrogen column density [10^{22}H cm^{-2}].

^{b} : Photon index of a power-law model for the continuum spectrum.

^{c} : Flux (no correction of absorption) in the 2–10 keV band [10^{-6}photons cm^{-2} s^{-1}].

^{d} : Center energy of iron line [keV].

^{e} : Equivalent width of iron line [keV].

^{f} : Absorption corrected luminosity in the 2–10 keV band [10^{33}erg s^{-1}].

5.4.2 Discussion

With 80-ksec observation with *ASCA*, we confirmed the diffuse X-ray emission which exhibits a strong iron line. Due to the limited photon statistics, we cannot constrain the physical parameters, such as ionization state of iron atoms. However, the equivalent width is too large to be explained by a thermal plasma model in ordinal abundance. If it is neutral iron line, large equivalent width is evidence for reflection. While, the absorption column is not larger than interstellar absorption. Hence it is difficult to conclude the origin of X-rays from Clump 2.

However, since the simple XRN model can reproduce the spectrum, we regard Clump 2 to be a candidate of XRN. The verification of XRN model by numerical simulation is seen in the next section.

5.5 Numerical Simulations of XRN Model

In section 5.1–5.4, we observed the molecular clouds in the GC region, and revealed the common features as follows;

1. we confirmed the presence of the very strong emission lines of neutral iron,
2. we found larger column densities than interstellar absorption (except Clump 2),
3. we found that the X-ray emitting region is extended and coincident with the molecular cloud. X-ray images of Sgr B2 and Sgr C are shifted to the GC side, in particular.

These peculiar X-ray spectra and distributions imply that the X-rays from these clouds are attributable to Thomson scattering (continuum emissions), photo-electric absorption of neutral iron atoms (low-energy cutoff and iron K-edge), and fluorescence (6.4-keV line), produced by an irradiation of an external X-ray source in the direction of the GC. The clouds should be the "X-ray Reflection Nebulae (XRNe)". In this section, we simulate the images and spectra of XRNe, and verify the hypothesis by comparing with the observations. In this analysis, we mainly use the *Chandra* results. However, we use the *ASCA* results for Clump 2, which is observed only with *ASCA*.

5.5.1 Conditions of Simulations

The geometry and configuration for XRN simulations are given in Figure 5.18, with the following assumptions.

(1) For the mass distribution, we adopt the result of ^{13}CO and the C^{18}O observations by Lis & Goldsmith (1989). The model cloud is cylinder-shape with its axis parallel to our line of sight.

The density distribution is shown as follows (in case of Sgr B2);

$$\left(\frac{n_{\mathrm{H_2}}}{1\mathrm{cm^{-3}}}\right) = 5.5\times10^4\left(\frac{r}{1.25\mathrm{pc}}\right)^{-2} + 2.2\times10^3, \tag{5.1}$$

where $n_{\mathrm{H_2}}$ is the number density of hydrogen molecules, and r is the projected distance from the center of the cloud. The thickness of the cloud is same as the radius. This formula gives the total molecular mass to be 6.3×10^6 $\mathrm{M_\odot}$ in the 45-pc diameter region. For the other clouds than Sgr B2, we assume the same density gradient as Sgr B2, and normalize the size and the density of the model cloud by using the observed mass and size of the cloud.

Since the density distribution is too simplified, we modify the shape of the model cloud for Sgr B2 to an elliptical cylinder to agree with the distribution of the radio intensity (e.g. Sato et al. 2000; see Figure 2.3). The ellipticity is 2, and its major axis is parallel to the line of longitude ($-30°$ to the Galactic plane; see Figure 5.19). Other clouds are assumed to be cylindrically symmetry, because X-ray images of these clouds are not simulated (see section 5.5.2).

(2) A primary source (irradiating source) is located in the GC-side with the normal angle to the cloud (cylinder) axis. The spectrum of the primary source is a power-law with photon index of 2 (Koyama et al. 1996).

For numerical simulations, we divided the model cloud into cells with same size, and calculated absorbed, reflected, and fluorescent X-rays in each cell as a function of incident X-ray energy (E) from the primary source. The size (number) of the cell is determined by the required fineness of the simulation. Figure 5.18 shows an example of the simulation of the 45-pc diameter cloud. When the cell size is 0.2 pc, the cloud is resolved into $225 \times 225 \times 113$.

For simplicity, we adopted further assumptions.

(3) The reflection and fluorescence are isotropic, and the absorption is given by the analytical function of the photoelectric cross section for the standard interstellar matter (Morrison & McCammon, 1983). The cross section of an iron atom is taken from Henke et al. (1982).

(4) Since the Thomson scattering optical depth is much smaller than that of the photoelectric absorption in the relevant energy band below 10 keV, we neglect the multiple Thomson scattering.

Then the probability $P_{\rm scat}(E)$ that a primary X-ray photon arrives at a cell, is scattered, and comes into our line of sight, is given as a function of photoelectric absorption cross section ($\sigma(E)$), the column density from the primary source to the cell ($N_{\rm H}^a$), the sell size (l), Thomson scattering cross section ($\sigma_{\rm T}$), the Hydrogen number density in the cell ($n_{\rm cell}$), and the column density from the cell to the surface of the cloud ($N_{\rm H}^b$) (see Figure 5.18).

$$P_{\rm scat} = l n_{\rm cell} \sigma_{\rm T} \exp\left(-N_{\rm H}^a \sigma(E) - N_{\rm H}^b \sigma(E)\right). \qquad (5.2)$$

Some fractions of the primary X-rays with energies above 7.1 keV, the K-edge of neutral iron, are absorbed with the cross section of an iron atom ($\sigma_{\rm Fe}(E)$). The absorbed X-rays are re-emitted as the 6.4-keV photons, with the probability of the fluorescence yield of 0.34 (Bambynek et al. 1972).

Thus the probability $P_{6.4}$, that a primary X-ray ($E \geq 7.1$ keV) is converted to the 6.4 keV line and comes into our line of sight, is similarly given;

$$P_{6.4} = 0.34 l n_{\rm cell} Z_{\rm Fe} \sigma_{\rm Fe}(E) \exp\left(-N_{\rm H}^{a}\sigma(E) - N_{\rm H}^{b}\sigma(6.4)\right), \tag{5.3}$$

where $Z_{\rm Fe}$ is abundance of iron.

In both the cases, the interstellar absorption from the primary source to the cloud is neglected. Adding the Galactic absorption from each cloud to the observer, we finally obtained simulated spectra.

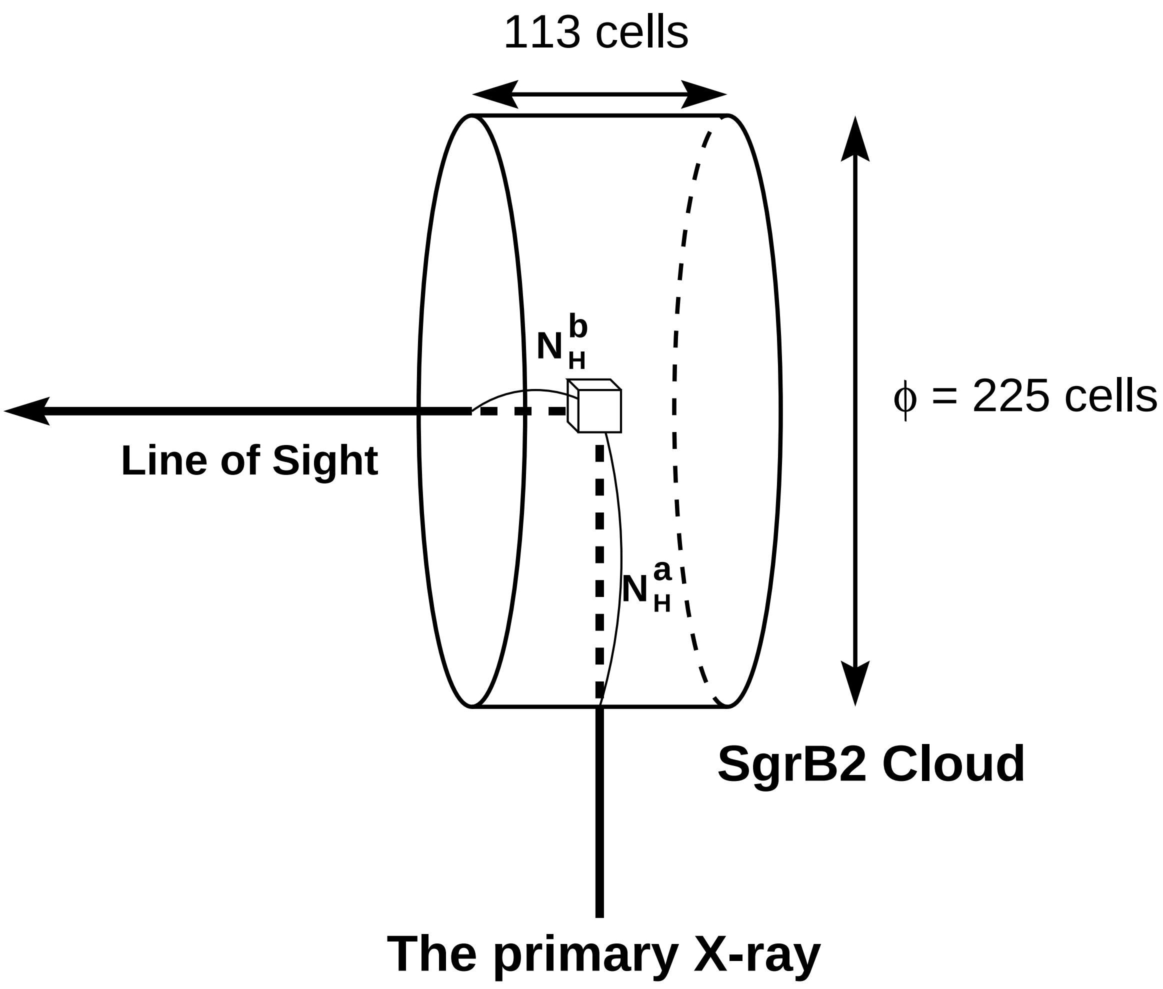

Figure 5.18: The schematic view of the XRN simulation . The cloud (45 pc diameter, 22.5 pc thickness) is divided into 225 × 225 × 113 cells, and the penetrating and reflecting (scattering) rate at each cell is calculated.

Mass and Size of each Cloud

We refer to radio observations of molecular lines for the size and the mass of each cloud. Since values vary with the definition of the parameters (particularly in size), we use the ratio to Sgr B2 cloud in each parameter to determine model cloud as possible.

In Table 5.9, we show the observed parameters of the clouds obtained with GC survey by Oka et al. (1998) and Stark et al. (1991). In these observations, the clouds are analyzed in unified manner, so we can obtain the accumulate ratio of parameters. For the Sgr C cloud, both survey data gives almost the same ratio to Sgr B2. We hence adopt the averaged ratio of 0.13 for the mass and 0.76 for the size, and estimate those parameters of model cloud to be $8.5 \times 10^5 M_\odot$ and 17.2 pc. The mass and size of Clump 2 is not mentioned in Oka et al. (1998). We used the data in Stark et al (1991), only.

M0.11−0.08 is not mentioned in Oka et al. (1998) nor Stark et al. (1991), and we cannot derive the ratio to Sgr B2. This cloud is investigated in detail by Oka et al. (2001) and Tsuboi et al. (1997) with CO and CS emission lines, respectively. The size of the cloud is almost the same in both observations, but the mass in Oka et al. (2001) is about an order of magnitude higher than the Tsuboi et al. (1997). It is because CS line is radiated from central dense core, while CO intensity may be due to the contribution of low-density gas. Since the model cloud of Lis & Goldsmith (1989) is based on CO data and the survey observations are made with CO lines, we refer to Oka et al. (2001). However, the uncertainty of mass and size may be large for M0.11−0.08. The estimated parameters of model clouds of four clouds are summarized in Table 5.9.

We must consider another factor in determining the cloud mass. Molecular clouds have two possible solutions in mass estimation: gravity equilibrium mass and pressure equilibrium mass. Oka et al. (1998) observed ^{12}CO and ^{13}CO line emissions, and revealed that if the clouds are assumed to be in gravity equilibrium, virial masses are an order of magnitude larger than masses estimated from the CO luminosity. To remove the discrepancy, they suggest that molecular clouds in the GC region should be in pressure equilibrium with the hot gas and/or the magnetic field near the cloud region. In this case, the masses become smaller than estimated values in Table 5.9. We then multiply a parameter $\eta(< 1)$ by each mass of the cloud.

Interstellar Absorption to each Cloud

The interstellar absorption to the GC region is systematically investigated by Sakano (2000). The column density is almost constant in the Galactic longitude direction ($|l_{\rm II}| \lesssim 1^\circ$), but largely

Table 5.9: The Parameters of the Molecular Clouds Used in XRN Simulation

	Mass ($\times 10^6 M_\odot$)			Size† (pc)		
	Oka98*	Stark‡	Model	Oka98*	Stark‡	Model
Sgr B2	7.1	6	6.3	36	100	22.5
Sgr C	0.96 (0.14)§	0.8 (0.13)§	0.85 (0.13)§	28 (0.78) §	75 (0.75)§	17.2 (0.76)§
Clump 2	—	3 (0.5)§	3.2 (0.5)§	—	480 (4.8)§	108 (4.8)§
M0.11−0.08	—	—	1.2¶	—	—	4.3¶

†: The radius of the cloud

*: The values are from Oka et al. (1998)

‡: The values are from Stark et al. (1991)

§: Values in parentheses show the ratio to the Sgr B2 cloud in each parameter.

¶: The values are from Oka et al. (2001)

decreases with the larger Galactic latitude. The 2-dimensional distribution can be expressed as:

$$N_{\rm H} = 4.1 \times e^{-\frac{1}{2}\left(\frac{|l'|}{2.1}\right)^2} \times |b'|^{-0.43} \quad (10^{22}{\rm H\ cm^{-2}}), \tag{5.4}$$

where $|l'| \equiv |l_{\rm II} + 0^\circ\!.056|$ and $|b'| \equiv |b_{\rm II} + 0^\circ\!.046|$ in the units of degree[1].

The center positions of the X-ray emissions are (l', b') = (0.724, 0.012), (−0.508, −0.001), (0.173, −0.062), (2.728, 0.049) for Sgr B2, Sgr C, M0.11−0.08, and Clump 2, respectively. The absorption column of each cloud is calculated to be 6–77 $\times 10^{22}$ H cm^{-2}. However, considering the extent of the clouds ($\sim 0^\circ\!.1$) and the rapid increase in absorption near $b' = 0$, these values are not significant. We then substitute the conservative limit of $b' = 0^\circ\!.1$, and obtain the column of $\sim 10^{23}$ H cm^{-2} for Sgr B2, Sgr C, M0.11−0.08, and $\sim 5 \times 10^{22}$ H cm^{-2} for Clump 2. We then adopted fixed values of 10^{23} H cm^{-2} (Sgr B2, Sgr C, M0.11−0.08) and 5×10^{22} H cm^{-2} (Clump 2) for the fittings of simulated spectra.

5.5.2 Simulated Images

For image analysis, we use only *Chandra* image of Sgr B2. Other clouds have poor photon statistics, and rather complicated density distributions, which are not valid for image analysis. While Sgr B2 is the most luminous in 6.4-keV line band and distributed in simple oval shape (Figure 2.3b, c).

[1]Our Galactic nucleus Sgr A* is located at ($l_{\rm II}$, $b_{\rm II}$) = (−0.056, −0.046).

Figure 5.19 is a simulated fluorescent line image of Sgr B2.The whole distribution of the fluorescent X-rays are concave shape pointing toward the irradiating source. These features resemble the *Chandra* image (Figure 5.3).

With the XRN model, the molecular cloud is irradiated by an external X-ray source. The X-rays penetrate into the molecular cloud, suffering with absorption, and excite iron atoms. Then fluorescent X-rays are emitted. If the cloud is optically thick, the X-rays cannot penetrate to the center of the cloud. Thus fluorescent X-ray distribution is shifted toward the irradiating source.

Hence the separation between the X-ray peak and the center of the cloud depends on the absorption column. We then compare the separation between the simulated and the observed fluorescent line image. Though the assumed shape of cylindrical configuration may not be valid for image simulation, the separation is a good indicator to estimate the cloud mass and abundances.

To compare the separation, we concentrate on the illuminated side of the molecular cloud. We make radial profiles of the observed and simulated flux in the opening angle of ± 60 degrees above and below the horizontal line pointing to the irradiating source located in the Galactic center direction.

The radial profile of the observed data in the 6.15–6.55 keV band is shown by the crosses in Figure 5.20, where the background level estimated from background region in Figure 5.3 is indicated by the dashed line. The central region within $10''$ radius are excluded because they are contaminated by the local excess of Sgr B2 Main. We also note that the other local excess, Sgr B2 North, is outside the opening angle of ± 60 degrees. We can see that the observed separation is about $\sim 40''$. While, simulated image with the solar abundance and $\eta = 1$ shows the separation of $\sim 90''$, which is significantly larger than observed value.

We then simulated the images with various abundances and masses. In the XRN model, X-rays above the 7.11 keV energy are absorbed mainly by iron atoms, while 6.4-keV X-rays are absorbed mainly by lighter elements such as carbon, nitrogen and oxygen[2]. Thus simulated separations depend on the number of iron atoms and other lighter elements, which are represented by two independent parameters[3] of ηZ_{Fe} and ηZ_{others}, where Z_{Fe} shows the abundance of iron, and Z_{others} shows the abundance of lighter elements. η is a coefficient of the mass

[2]X-rays above 7.11 keV also absorbed by lighter elements, but the efficiency is lower than iron atoms. The simulation includes cross sections of lighter elements even in higher energy

[3]Since the absorption cross sections of hydrogen and helium atoms are much smaller, we ignore the dependence on these atoms (total number is nearly proportional to η).

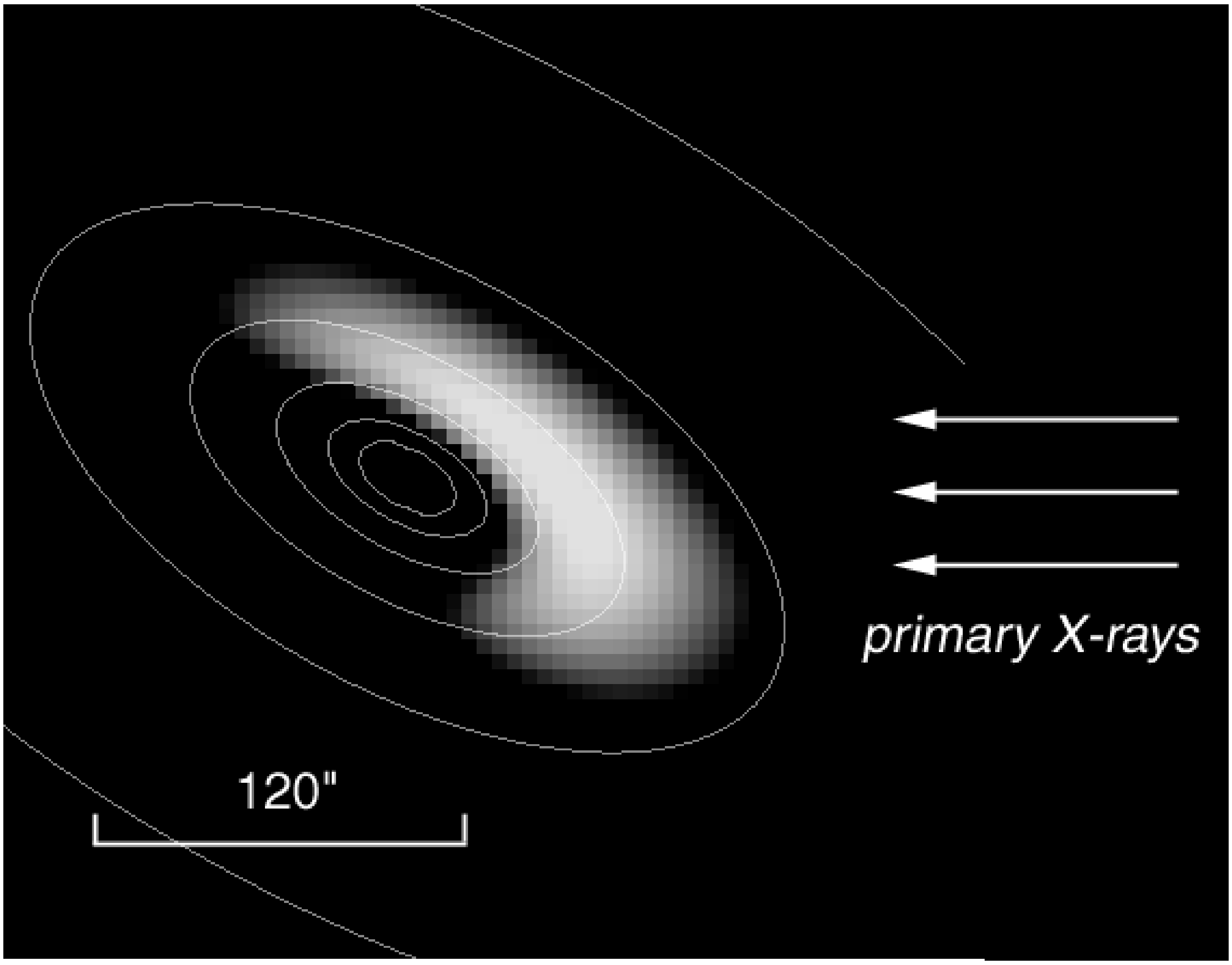

Figure 5.19: Simulated image of the iron fluorescent line with the XRN model. Contours show the density distribution of the model cloud. Primary X-ray source is to the right.

(section 5.5.1). We then simulate images with the various sets of ($\eta Z_{\rm Fe}$, $\eta Z_{\rm others}$).

The simulated profile fits the observed data well at the allowable region shown in Figure 5.21; the separation between X-ray peak and the cloud center is 1.5±0.4 pc (or 36±10″). We show the best-fit profiles of ($\eta Z_{\rm others}$, $\eta Z_{\rm Fe}$) = (0.3, 0.3) in Figure 5.20 in solid line.

Thus we revealed that the *Chandra* image can be reproduced by the simulated image. However, we need more complicated assumption of gas distribution for more accurate quantitative comparison.

5.5.3 Simulated Spectra

Figure 5.22 shows an simulated spectrum with the solar abundance and $\eta = 1$, in case of Sgr B2. There are strong Kα (6.40 keV) and Kβ (7.06 keV) lines of neutral iron and a deep iron K-edge (7.11 keV). In this subsection, we fit the simulated spectrum to the observed spectrum of the cloud. Spectral simulation is made for all the clouds.

Sgr B2

The simulated spectra are convolved with the response function of ACIS and are compared with the observed spectrum. We first fit the observed spectrum of Sgr B2 to the simulated one with the XRN model of solar abundances, where a free parameter is only the normalization of the flux.

This simulated spectrum, however, is rejected with a reduced χ^2 of 1.48 (23 d.o.f.). Residuals are found in the flux of the 6.4 keV line, depth of the K-edge and low-energy absorption.

As already mentioned in image analysis, X-rays above the 7.11 keV energy are absorbed mainly by iron atoms, while the lower energy X-rays are absorbed mainly by lighter elements such as carbon, nitrogen and oxygen. While continuum X-ray flux by the Thomson scattering is proportional to the number of electrons (∼hydrogen atoms). Accordingly, the ratio of absorption depth at 7.11 keV and low energy band is proportional to the abundance ratio of iron and the other elements. The equivalent width of the 6.40 keV line constrains the iron abundance. We thus simulate the spectrum with various abundance sets of iron and the lighter elements and compare with the observed spectrum.

Since the number of hydrogen atoms independently depend on η, there are three independent variables of η, $Z_{\rm Fe}$, and $Z_{\rm others}$. We then simulate the spectra with various sets of ($Z_{\rm Fe}$, $Z_{\rm others}$), and η.

We obtained acceptable fittings. The 90% confidence region is laid on the Figure 5.21 in

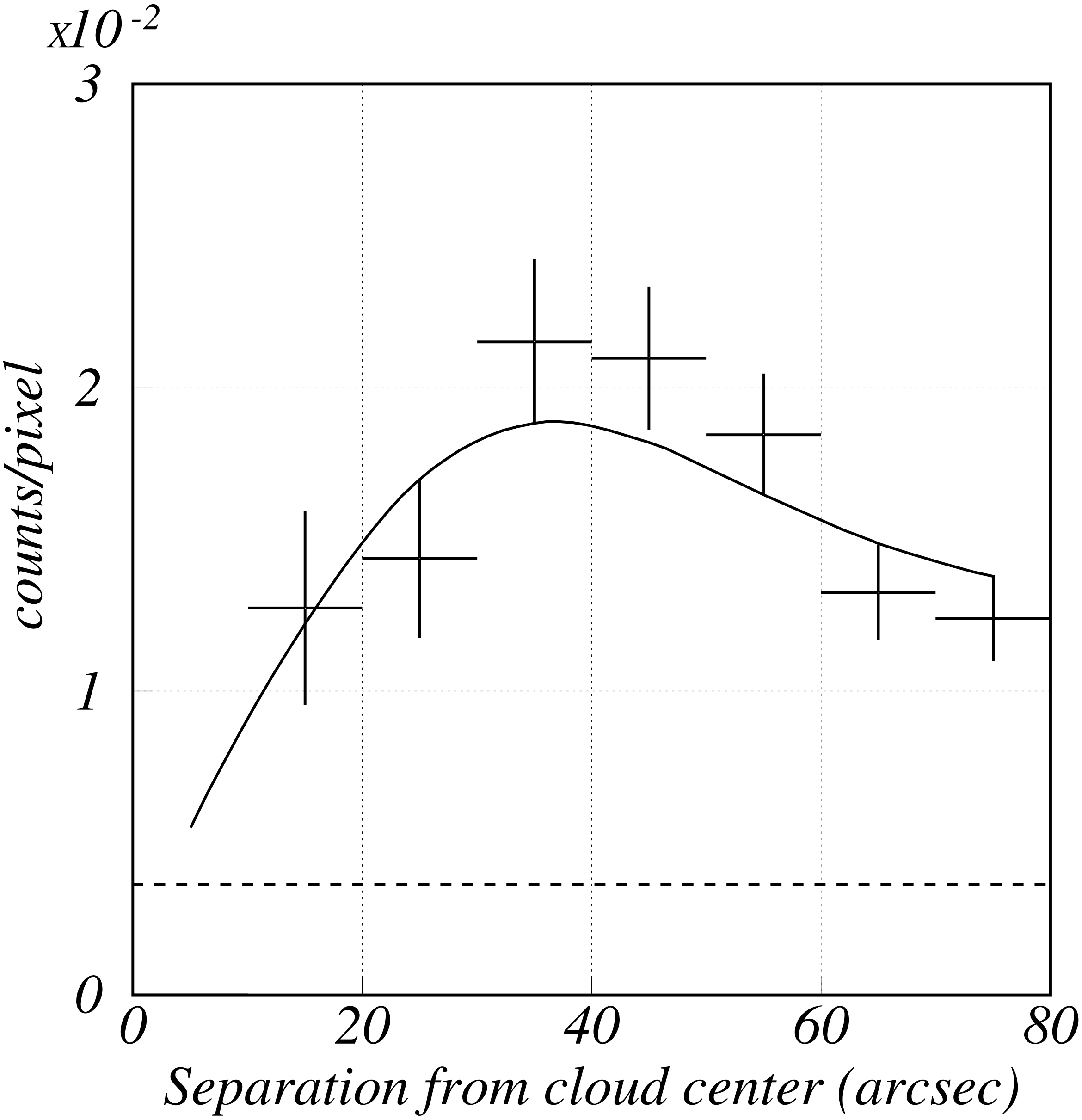

Figure 5.20: The radial profile of the surface brightness of the 6.4 keV line (crosses). The solid line shows the simulation of the XRN model, and the dashed straight line indicates the background level estimated from the background region shown in Figure 5.3.

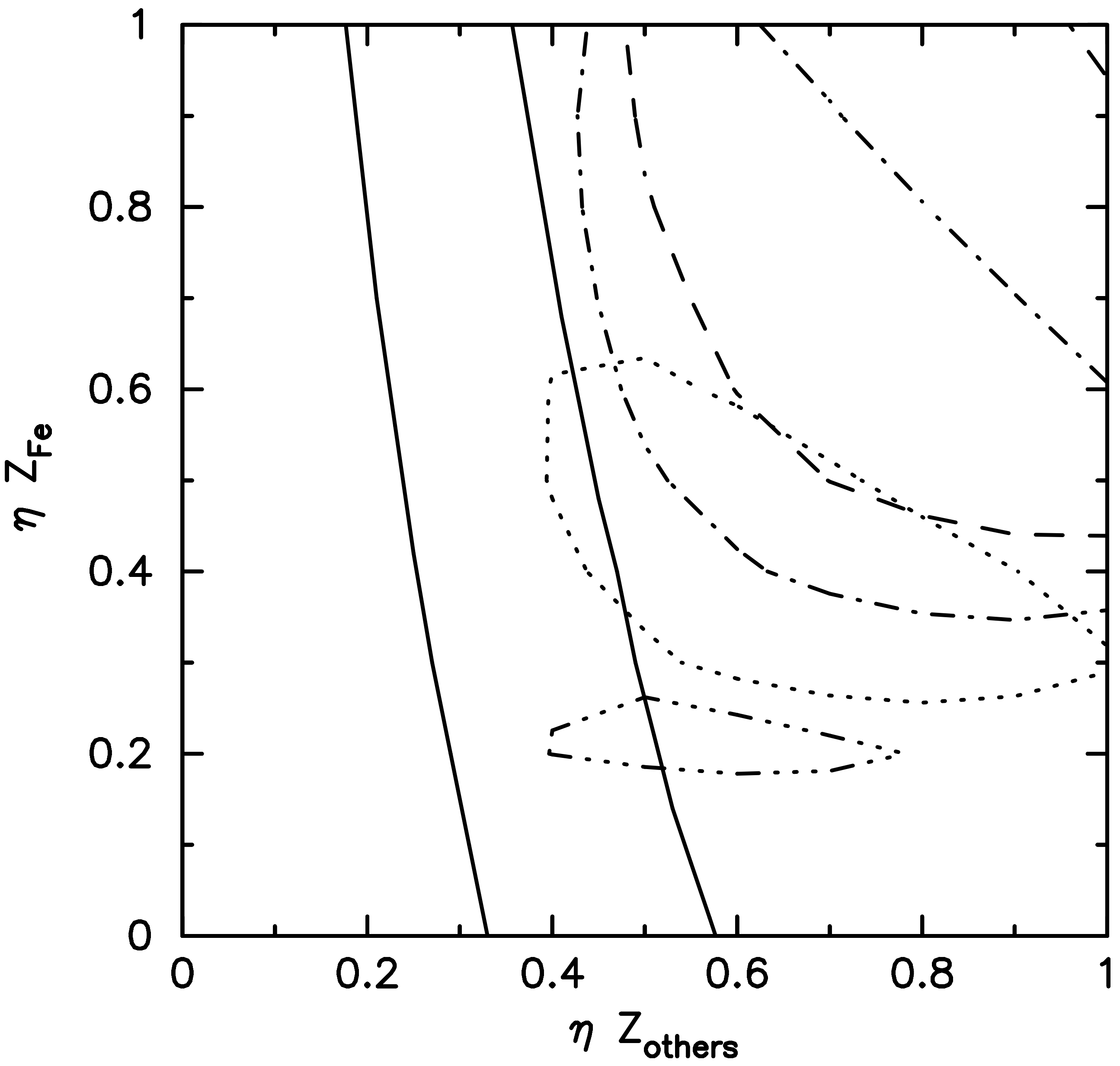

Figure 5.21: The allowable region of ηZ_{others} and ηZ_{Fe} constrained by image analysis (between two solid lines). Spectral constraints are also indicated by dashed ($\eta = 0.4$), dash-dotted ($\eta = 0.3$), dotted ($\eta = 0.2$), and dash-dot-dot-doted ($\eta = 0.1$) lines.

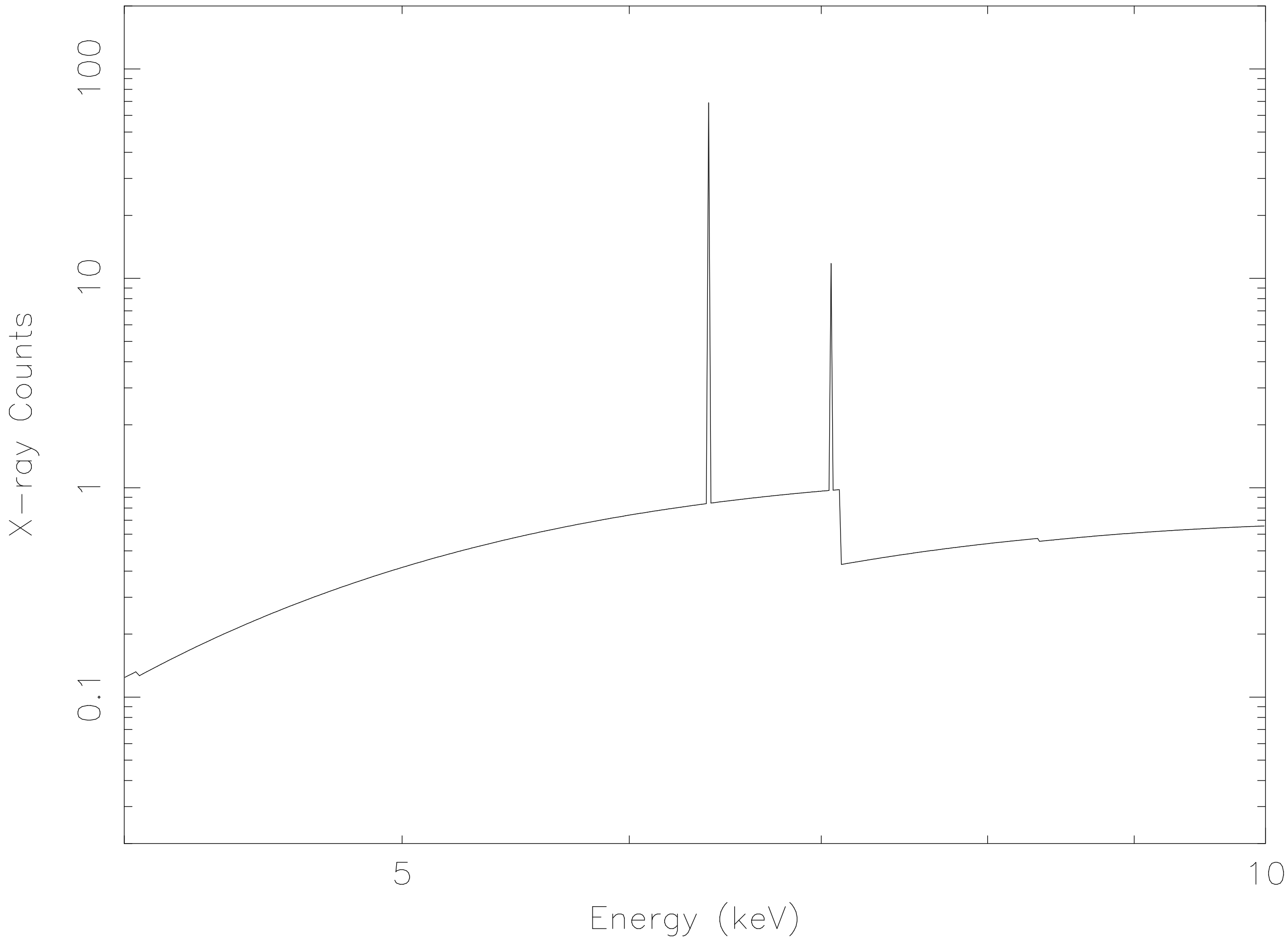

Figure 5.22: A simulated spectrum with XRN model. The spectrum exhibits iron Kα (6.40 keV), Kβ (7.06 keV) lines, and K-edge (7.11 keV).

case of $\eta = 0.1$, 0.2, 0.3, and 0.4. We can find that the allowable regions of the image and the spectral analysis overlap each other at $\eta < 0.3$. No significant lower limit of η is determined. In case of $\eta = 0.2$, the best-fit parameters within the overlapping region are $(Z_{\rm Fe}, Z_{\rm others}) = (2.5, 2.0)$. The best-fit model spectrum is shown in Figure 5.23.

Hence we revealed that observed image and spectrum of Sgr B2 can be explained by the XRN model.

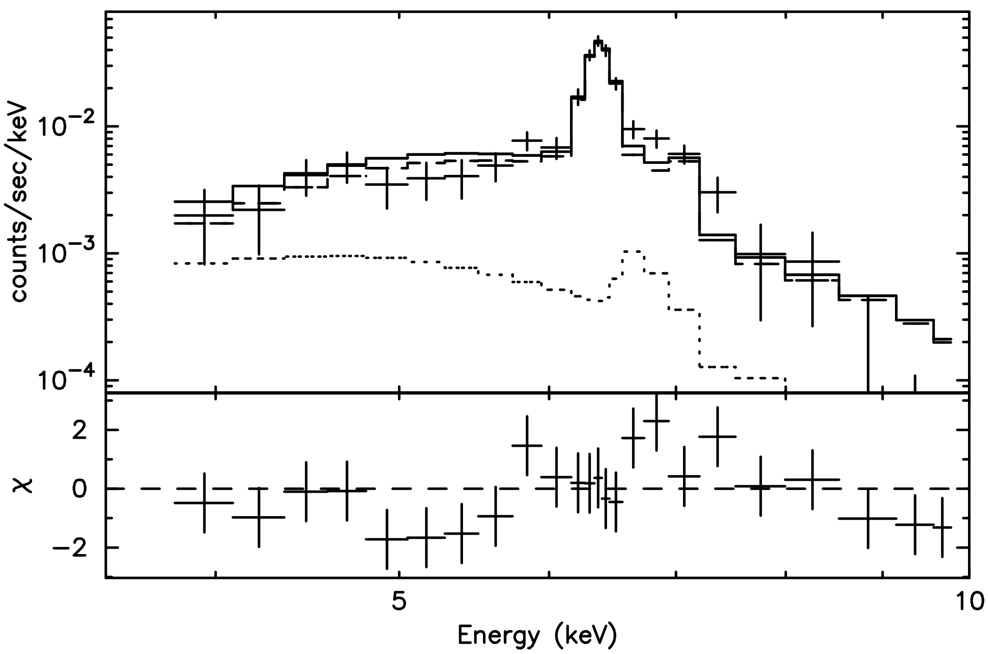

Figure 5.23: X-ray spectrum of Sgr B2 obtained with *Chandra* ACIS and best-fit spectrum of XRN model in case $\eta = 0.2$ (dashed line). The dotted line indicates the contribution of all the resolved point sources in Sgr B2.

Sgr C, M0.11−0.08, Clump 2

With the same procedure as Sgr B2, we fit the spectra of the rest three clouds. We have already known that $\eta < 0.3$ in case of Sgr B2. Assuming the coefficient η to be same in all clouds, we simulate the spectra in two cases: $\eta = 0.1$, 0.2. The acceptable regions of each case is shown in Figure 5.24, 5.25.

All of the spectra can be reproduced by simulated spectra. Hence XRN hypothesis is verified with numerical simulations.

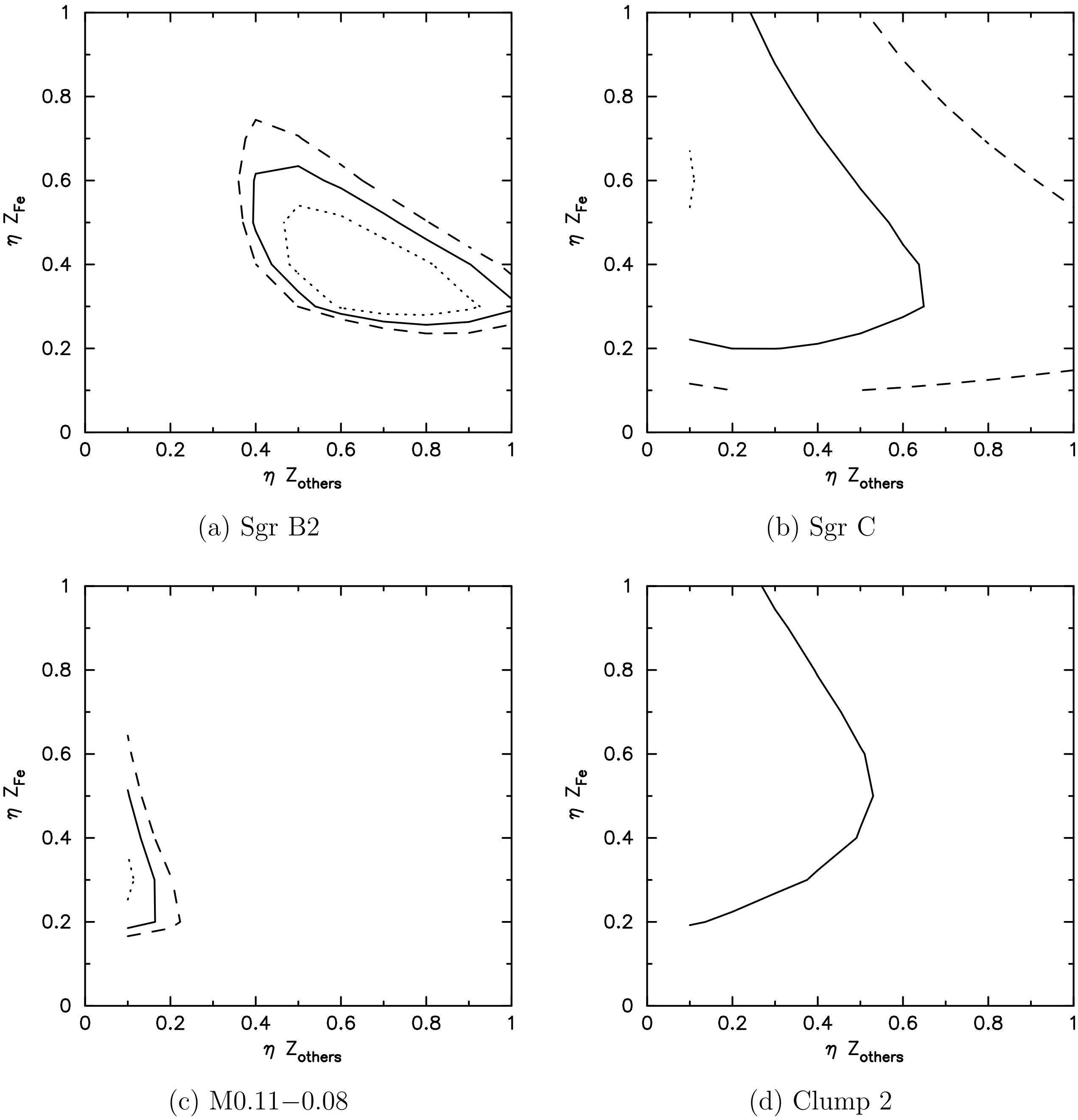

Figure 5.24: Acceptable regions of spectral fittings with XRN model ($\eta = 0.2$). 80%, 90%, and 95% acceptance level is shown by dotted, solid, and dashed lines, respectively. The acceptable regions of Sgr C, M0.11−0.08, and Clump 2 are left side of the lines.

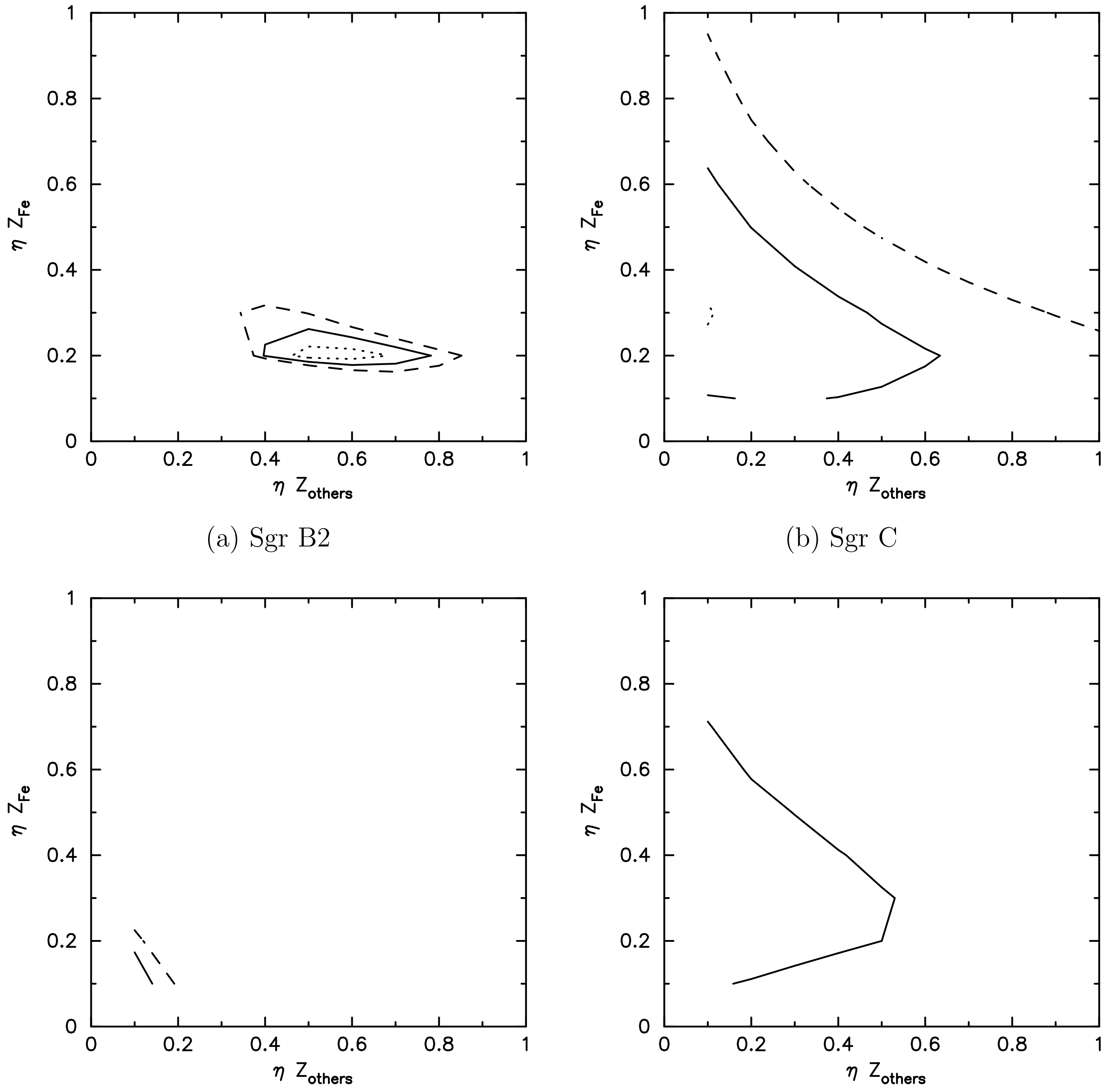

(a) Sgr B2 (b) Sgr C

(c) M0.11−0.08 (d) Clump 2

Figure 5.25: Confidence contours of spectral fittings with XRN model ($\eta = 0.1$). 80%, 90%, and 95% acceptance level is shown by dotted, solid, and dashed lines, respectively. The acceptable regions of Sgr C, M0.11−0.08, and Clump 2 are left side of the lines.

Chapter 6

Results II. — Supernova Remnants

Supernova remnants (SNRs) are the plausible candidate to produce the high-temperature plasma extended in the GC region. However, the number of discovered SNRs is insufficient to explain the large total energy of the plasma. Recently, high angular resolution of *Chandra* enables us to search very small SNRs because of the short evolution time after the explosion, or very faint SNRs which are buried in a surrounding X-ray emissions. In this chapter, I introduce the newly discovered SNR candidates: G 359.92−0.09 and G0.570−0.018.

6.1 G 359.92−0.09

G 359.92−0.09 is newly discovered in the X-ray band with *Chandra*. This SNR is at the south of Sgr A East.

6.1.1 Radio Observations

Ho et al. (1985) detected an elongated future, called "wisp", at $\sim 4'$ south of Sgr A* with the radio continuum observations (Figure 6.1). The radio emission from "wisp" is non-thermal and polarized 10–20 %. Combined with the distribution of NH_3 molecules, the authors indicated that the "wisp" is a part of the SNR, which is interacting with a molecular cloud. The inward curve of the Sgr A East and the other condensations aligned in a circular shape (shown by dotted line in Figure 6.1a) imply a shell-like structure, which is attributable to SNR. The later observation of the dynamics of molecular material supported the interaction with the molecular cloud and Sgr A East, then this SNR candidate is named G 359.92−0.09 (Coil & Ho 2000).

However, this object is detected only by radio band. In addition, only a few clumps are observed. The radio observations are insufficient to conclude that G 359.92−0.09 is SNR.

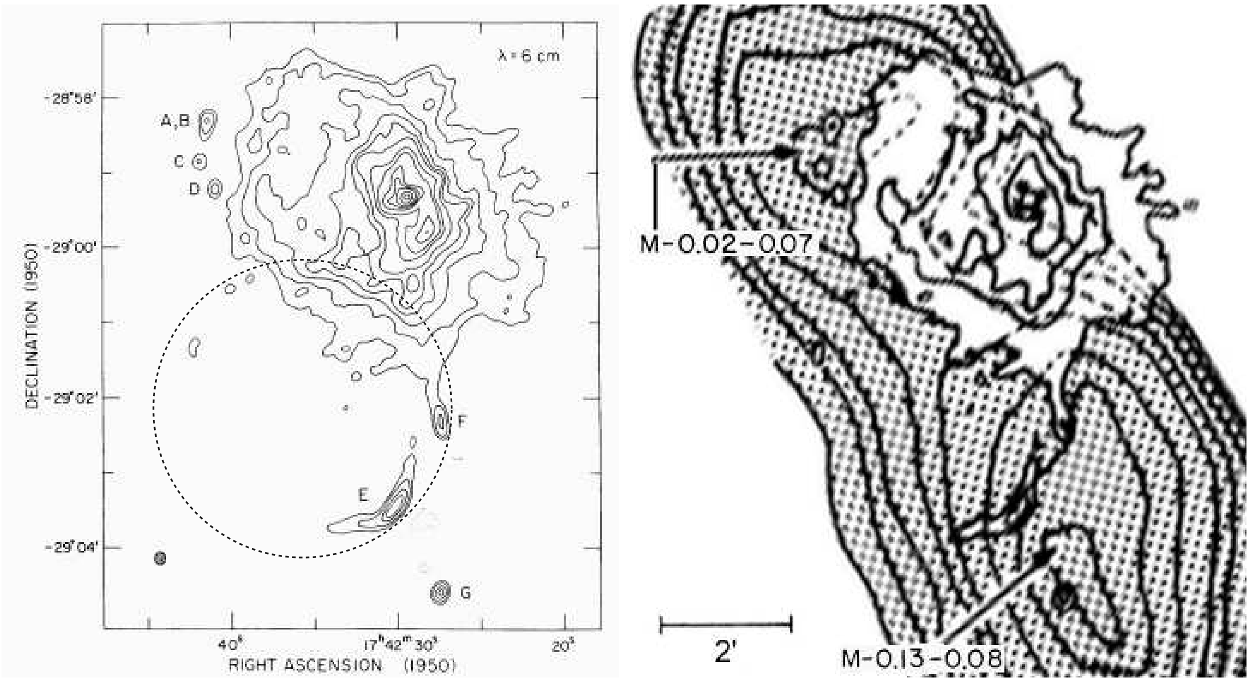

(a) Radio 6 cm image

(b) NH_3 image

Figure 6.1: The radio image of the Sgr A region (Ho et al. 1985). (a) 6 cm continuum map. A elongated future “wisp” (E) continues northwest into another condensation (F). Both condensations and other three features at R.A. = $17^{\mathrm{h}}42^{\mathrm{m}}40\overset{\mathrm{s}}{.}0$, Dec = -29°01′00″ (epoch 1950) may be part of a SNR with shell-type morphology (dotted circle). (b) The 6 cm continuum map superposed on an NH_3 emission map. Two molecular condensations of M$-0.02-0.07$ and M$-0.13-0.08$ are shown. The shell-like structure seems to interact with M$0.13-0.08$ at the position of “wisp”.

6.1.2 *Chandra* Observation

Image

Figure 6.2 shows the *Chandra* 3–8 keV image around the Sgr A region. A sharp structure is detected at the same position as "wisp". In addition, diffuse X-ray emission is detected from the eastern half (left in the figure) in the circular structure indicated in radio band.

Figure 6.3 shows the radial profiles of the diffuse X-ray emission in the each quadrant of the circular structure (divided by the dashed lines in Figure 6.2). There are excesses in the shell at the northeast and the southeast part compared with the outside region. The boundary shape is similar to a step-function. The northwest part shows no clear boundary because of the contamination of the intense X-ray emission from Sgr A East. The southwest part shows no excess in the shell, but has very sharp boundary, which is attributable to the "wisp".

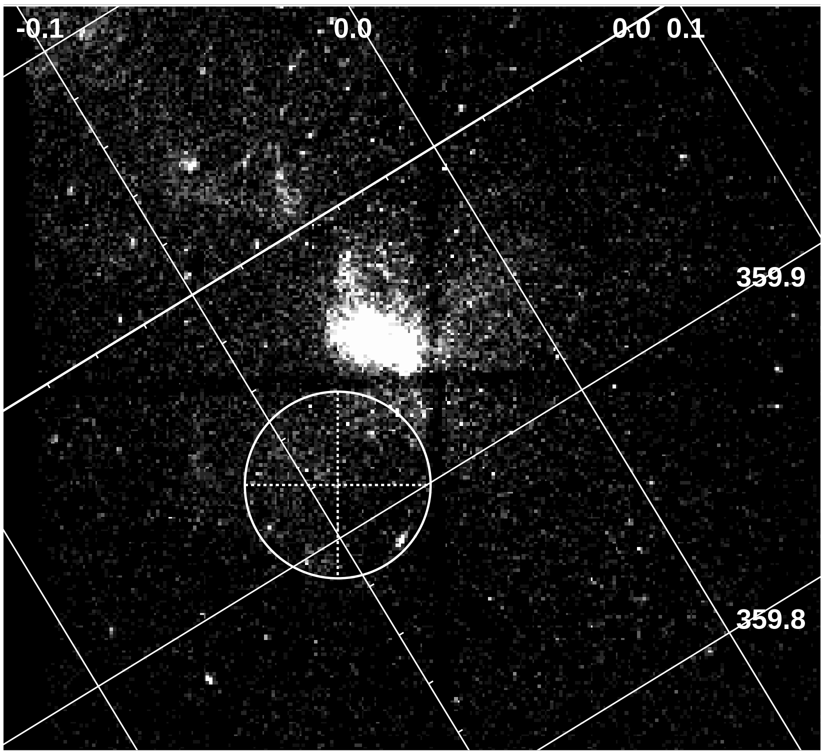

Figure 6.2: The X-ray image of G 359.92−0.09 in 3.0–8.0 keV band. Up is north, and left is east. There is diffuse emission in the circular region suggested by radio observations (solid line). Radial profiles are taken from the each quadrant of the circular region divided by dashed lines.

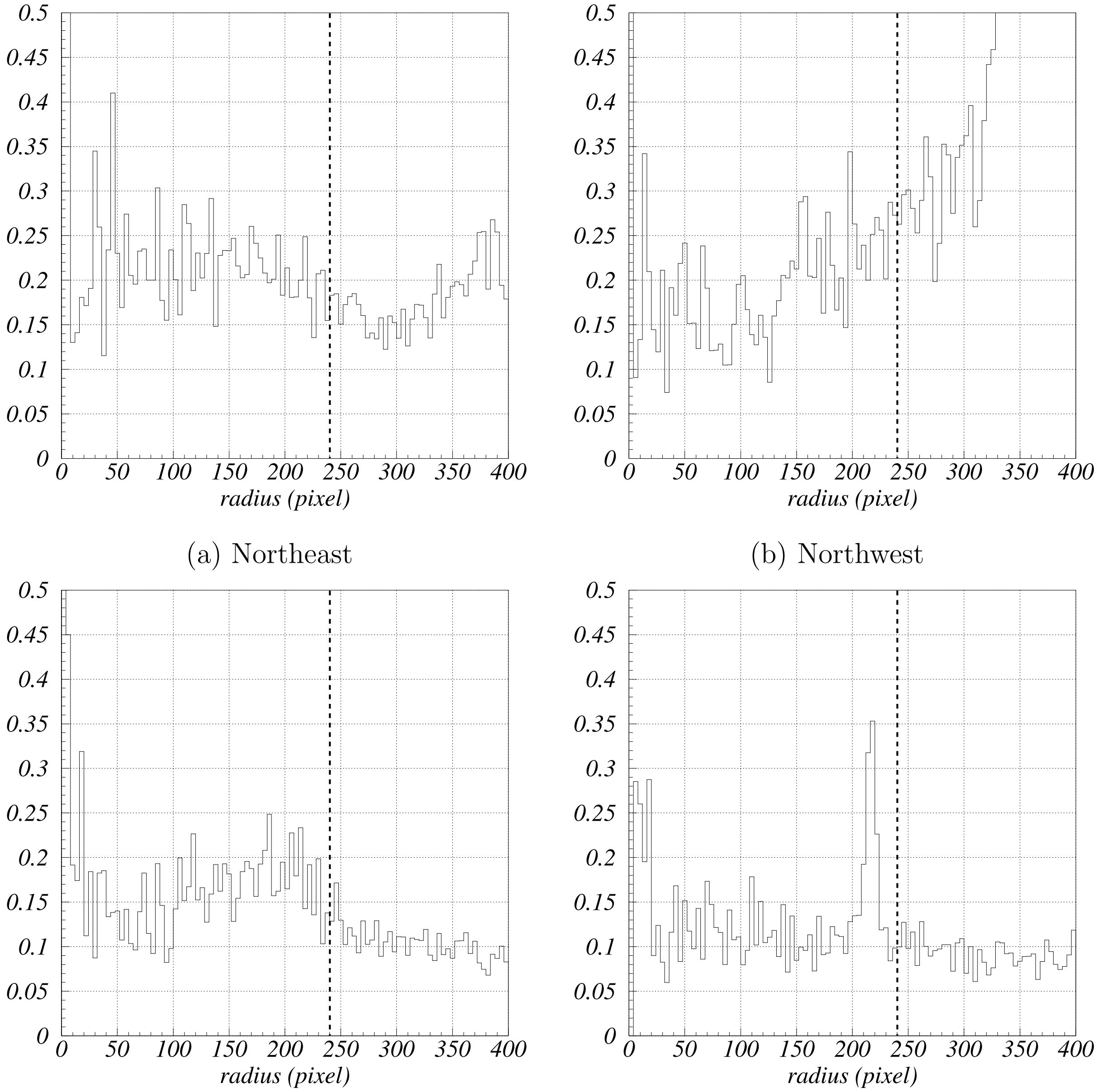

(a) Northeast

(b) Northwest

(c) Southeast

(d) Southwest

Figure 6.3: Radial profiles of the X-ray emission from (a) northeast, (b) northwest, (c) southeast, and (d) southwest part of the circular structure. In each figure, the horizontal line shows the radius from the shell center, and the vertical line shows the X-ray counts per pixel. Dashed lines show the boundary of circular region shown in Figure 6.2.

Spectrum

At first, we extract the X-rays from the eastern half of the shell structure, and make the spectrum (Figure 6.4). The source region is inside of the circle of $r < 2'$, and the background region is the annulus of $2' < r < 2\farcm 8$, where r is the distance from the center of the shell. The spectrum exhibits the strong iron K-line. We fit the spectrum with a phenomenological model of the thermal bremsstrahlung and an Gaussian line. The center energy of the iron is 6.62 keV, which is slightly lower than that of the He-like iron. We then fit the spectrum with the non-equilibrium ionization (NEI) model, and obtain the best-fit values shown in Table 6.1. The Hydrogen column density of about 6×10^{22} H cm^{-2} is consistent with the Galactic absorption to the GC (Sakano 2000). The ionization parameter nt, where n and t are plasma density and elapsed time after the plasma is heated-up, is $1.4^{+5.4}_{-0.6} \times 10^{11}$ s cm^{-3}. In this fitting, we fixed the metal abundances to be the solar values.

Figure 6.5 and Figure 6.6 show the X-ray spectrum of the "wisp" and the southwestern quadrant, respectively. Both spectra show the iron K-line. We fit the spectra with the same model as eastern half. The best-fit values are also shown in Table 6.1. Both region exhibit larger absorption than eastern half region.

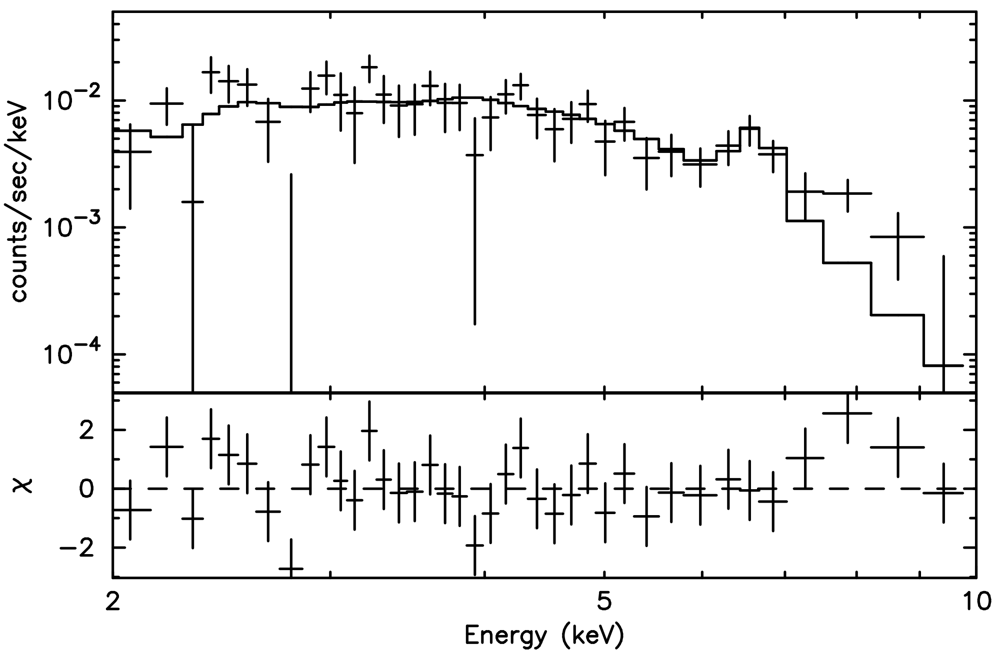

Figure 6.4: The X-ray spectrum of the eastern half region of the G359.92−0.09. The best-fit spectrum with NEI model is shown by solid line.

Table 6.1: Table

	N_H[a]	kT[b]	nt[c]	F_X[d]	L_X[e]	χ^2/d.o.f.
eastern half	$6.0^{+2.3}_{-2.3}$	$11.4^{+68.5}_{-8.0}$	$13.5^{+54.4}_{-5.4}$	15^{+1}_{-2}	$1.8^{+1.7}_{-0.4}$	44.37/38
wisp	37^{+7}_{-5}	12.7 (> 7.9)	884 (> 0.01)	4.4 ± 0.5	1.2 ± 0.2	6.0/5
southwestern quadrant	18^{+15}_{-11}	$2.6^{+74.7}_{-0.7}$	20.6 (> 0.1)	$4.3^{+0.9}_{-0.8}$	$1.4^{+220}_{-1.1}$	9.8/9

[a] : Hydrogen column density [10^{22}H cm^{-2}].

[b] : The temperature of the plasma [keV].

[c] : The ionization equilibrium parameter [10^{10}s cm^{-3}]

[d] : Flux (no correction of absorption) in the 2–10 keV band [10^{-13}erg cm^{-2} s^{-1}].

[e] : Absorption corrected luminosity in the 2–10 keV band [10^{34}erg s^{-1}].

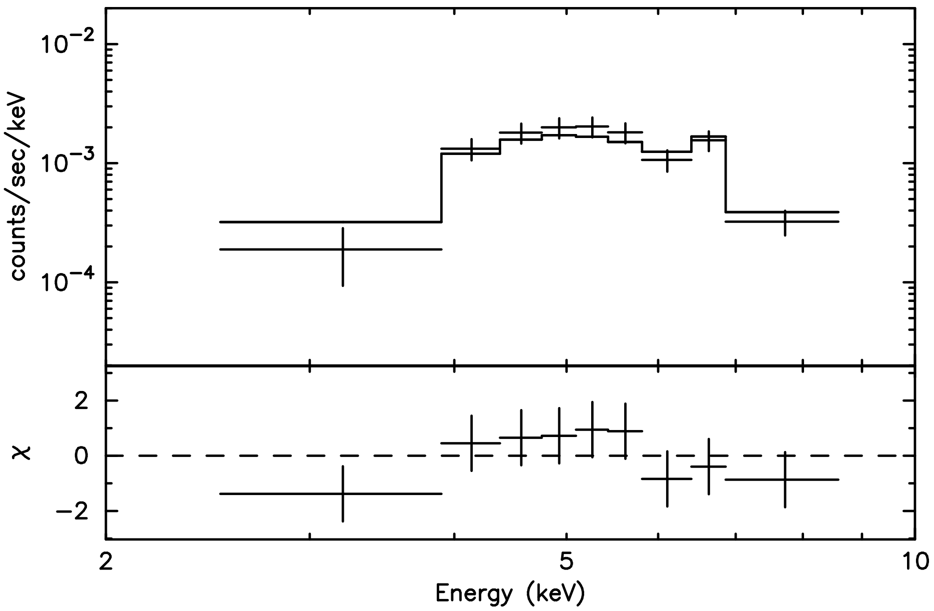

Figure 6.5: The X-ray spectrum of the “wisp”.

6.1.3 Discussion

X-ray emission from the western part

In section 6.1.2, we confirmed the presence of the diffuse X-ray emission at the eastern part of G359.92−0.09, but there is no clear excess in the western part. In addition, the spectrum

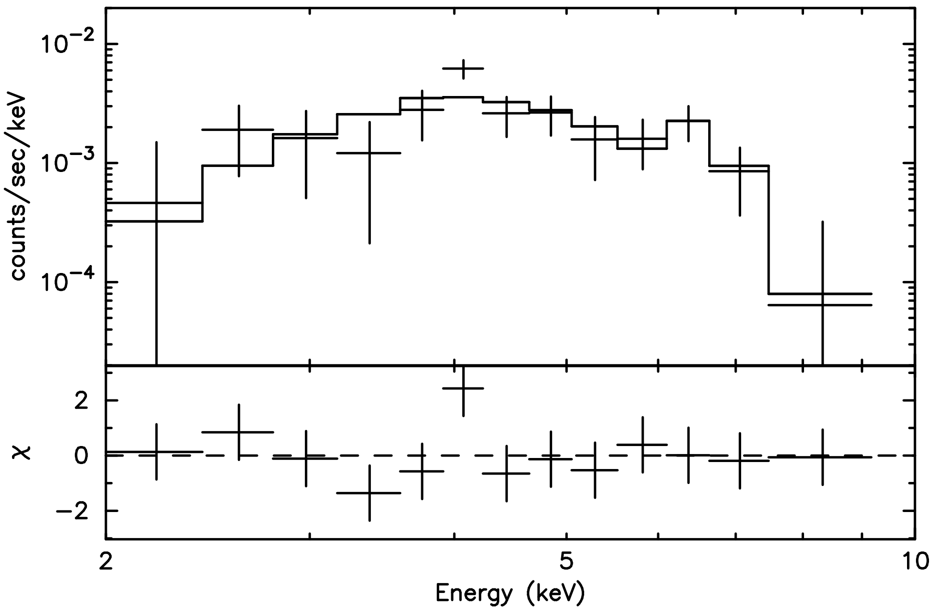

Figure 6.6: The X-ray spectrum of the southwestern quadrant of the G359.92−0.09.

analysis indicates that there is a larger absorption column in the west. These results imply that the western part of the SNR is behind the molecular cloud: M−0.13−0.08 in Figure 6.1b. The column density of the cloud is estimated to be (3–8) $\times 10^{23}$ H cm^{-2} by Zylka et al. (1990) and (8–14) $\times 10^{23}$ H cm^{-2} by Coil & Ho (1999). These values are larger than, or sufficient to explain the X-ray absorption.

Coil & Ho (2000) investigated the dynamics of the molecular clouds within 15 pc of the Galactic center, and concluded that the cloud and molecular flow, called southern stream, are interacting with G359.92−0.09. Though they suggested that the molecular cloud and southern stream are more behind the SNR, it is marginal and difficult to decide the position in line of sight only with the radio data (e.g. Coil & Ho 1999). Thus we suspect that at least a part of the molecular cloud is in front of the SNR, and the lack of X-ray intensity in the west is only due to the absorption.

Physical parameters

In this section, we use only eastern half data to estimate the physical parameters of the SNR. We assumed the distance to the SNR to be 8.5 kpc. With the spectral fitting, we obtained the best-fit values of emission measure ($E.M. = n^2V$) of 1.1×10^{57} cm^{-3}, and ionization parameter nt of 1.4×10^{11} cm^{-3} s, where V is the plasma volume. Assuming the X-rays are emitted from the uniform hemisphere with the size of the spectrum region of $2'$ (~ 5 pc) radius, the volume is calculated to be $\sim 7 \times 10^{57}$ cm^{-3}. Hence the plasma density (n) and ionization age (t) are estimated to be about 0.4 cm^{-3} and 10^4 year, respectively.

6.2 G0.570−0.018

This X-ray source is located at the $7'$ southwest from Sgr B2. *ASCA* detected a faint X-ray peak from the same observed region of Sgr B2. Then *Chandra* revealed a shell-like structure with the radius of about $10''$. The detailed description about G0.570−0.018 will be published soon (Senda et al. 2001).

6.2.1 *ASCA* Observation

Because G0.570−0.018 is near the Sgr B2 region, it is observed simultaneously with Sgr B2 (Section 5.1.1). The net observed time is about 95 ksec for GIS.

Image

Figure 6.7 shows the 6.0–7.0 keV image near the Sgr B2 region. The brightest X-ray peak is Sgr B2, but there is another peak near the center of the image (solid circle). This source is already mentioned in Sakano, Yokogawa, & Murakami (1999) and Sakano (2000), and named AX J1747.0−2828. We can not determine that X-rays are from a point source or an extended structure with the angular resolution of *ASCA*. The position of the peak is $0.°55 \leq l \leq 0.°57$, $-0.°02 \leq b \leq 0.°00$.

Spectrum

The spectrum is obtained from the $3'$ radius region around the X-ray peak, and the background region is annulus with the radius of $3'$–$4'$, which are indicated by solid and dashed lines in Figure 6.7, respectively. Figure 6.8 shows the spectrum.

We fit the spectrum with the phenomenological model of a thermal bremsstrahlung and a Gaussian line, and obtain acceptable fittings. The best-fit parameters are shown in Table 6.2. Strong Kα line of iron is detected with the center energy of 6.5–6.7 keV and the equivalent with of about 3.7 keV.

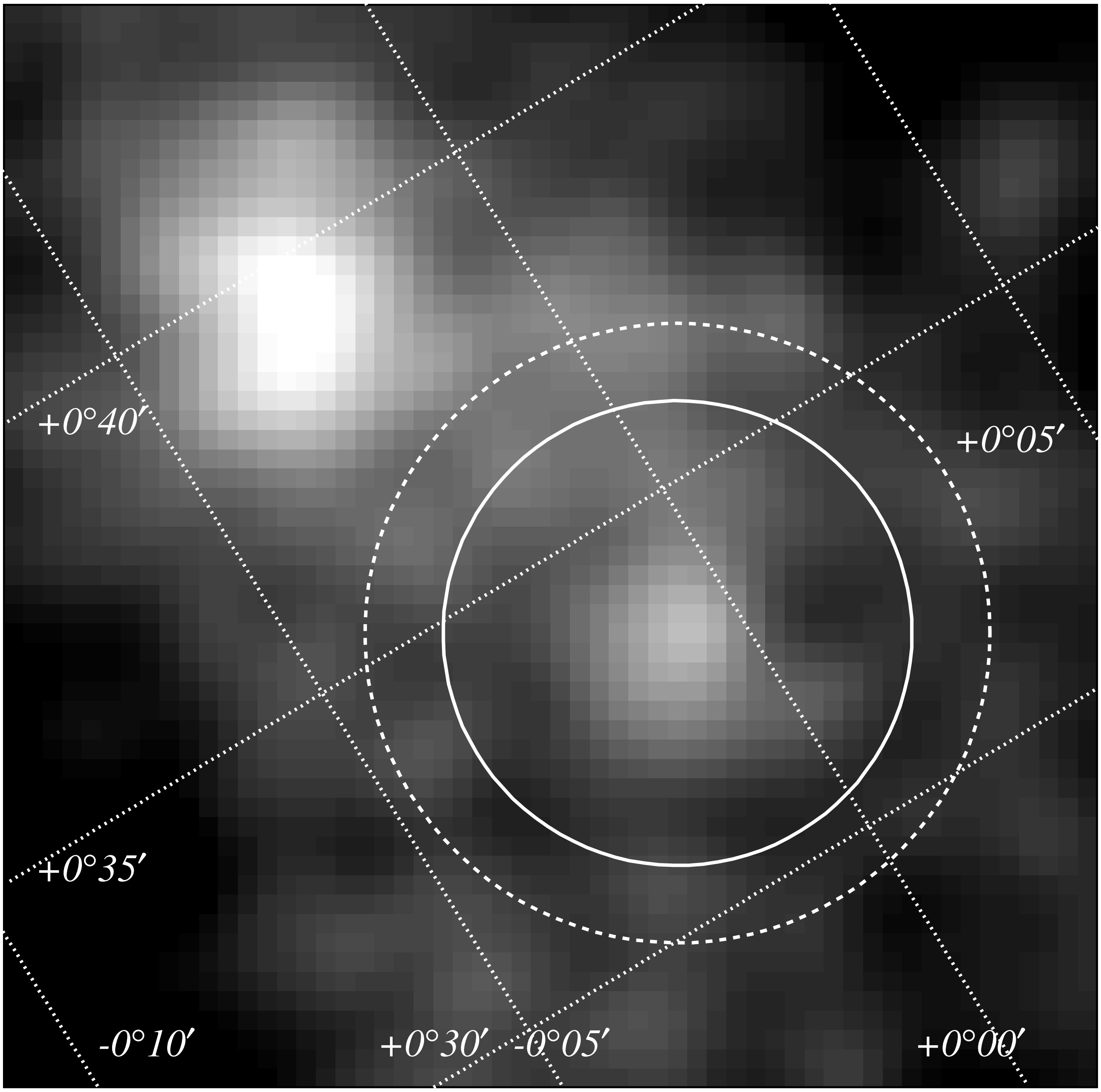

Figure 6.7: The 6.0–7.0 keV image around G0.570−0.018 observed with *ASCA*. The X-ray image is same as figure 5.1, but zoomed in G0.570−0.018

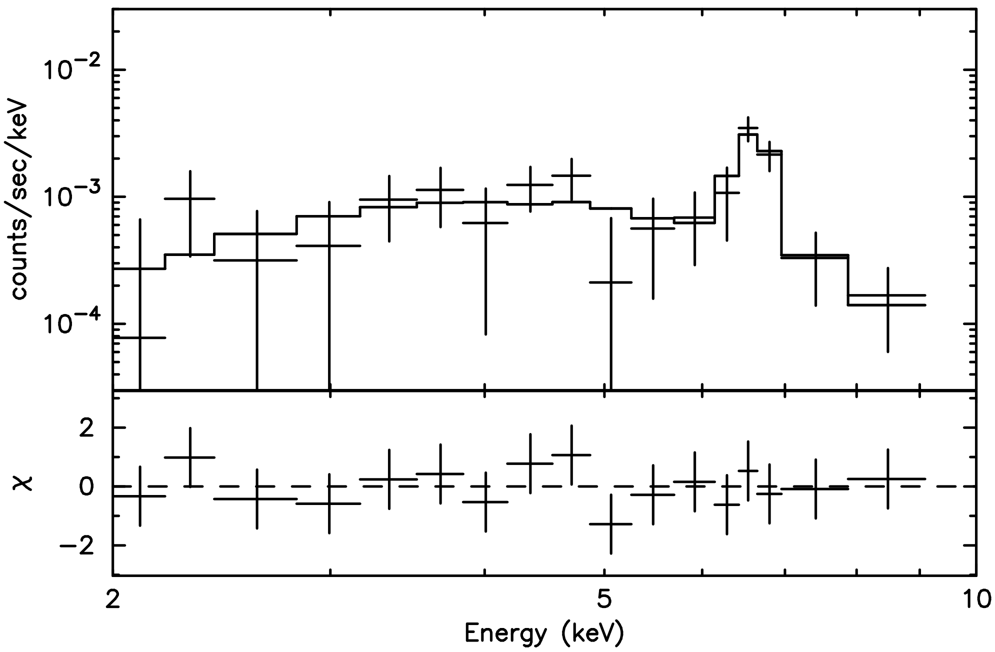

Figure 6.8: The X-ray spectrum of G0.570−0.018 obtained with *ASCA*. The solid line shows the best-fit spectrum with a thermal bremsstrahlung and a Gaussian line model.

Table 6.2: Best-Fit Results of the X-ray spectrum of G0.570−0.018 obtained with *ASCA*.

	Continuum			Iron line				
	$N_{\rm H}$[a]	kT[b]	$F_{\rm X}$[c]	$E_{\rm C}$[d]	$F_{\rm X}$[c]	EW[e]	$L_{\rm X}$[f]	χ^2/d.o.f.
GIS	$8.1^{+18.8}_{-5.3}$	13.6(>1.3)	4.7 ± 1.4	$6.60^{+0.12}_{-0.09}$	2.6 ± 0.8	3.7	9^{+3}_{-2}	6.4/12

[a] : Hydrogen column density [10^{22}H cm^{-2}].

[b] : The temperature of the plasma [keV].

[c] : Flux (no correction of absorption) in the 2–10 keV band [10^{-13}erg cm^{-2} s^{-1}].

[d] : Center energy of iron line [keV].

[e] : Equivalent width of iron line [keV].

[f] : Absorption corrected luminosity in the 2–10 keV band [10^{33}erg s^{-1}].

6.2.2 *Chandra* Observation

G0.570−0.018 is included in the 100 ksec observation field of Sgr B2 with Chandra.

Image

Figure 6.9 shows the *Chandra* image of G0.570−0.018 in 4.0–7.0 keV band. X-ray emission shows clear shell-like structure of about 10″ radius. The center of the shell is R.A.= $17^{\mathrm{h}}47^{\mathrm{m}}02\overset{\mathrm{s}}{.}6$, Dec= $-28°27'33''$ (epoch 2000), which corresponds to $(l, b) = (0\overset{\circ}{.}570,\ -0\overset{\circ}{.}018)$, the same position of the *ASCA* diffuse source within the error.

To investigate the shape of X-ray emission, we make a radial profile of X-ray emission from the center of the shell. Figure 6.10 is the radial profile in the 4.0–7.0 keV band. There is the clear excess around 10″ with the width of about 6″ (FWHM). Hence it is revealed that the diffuse emission is distributed as circular shape.

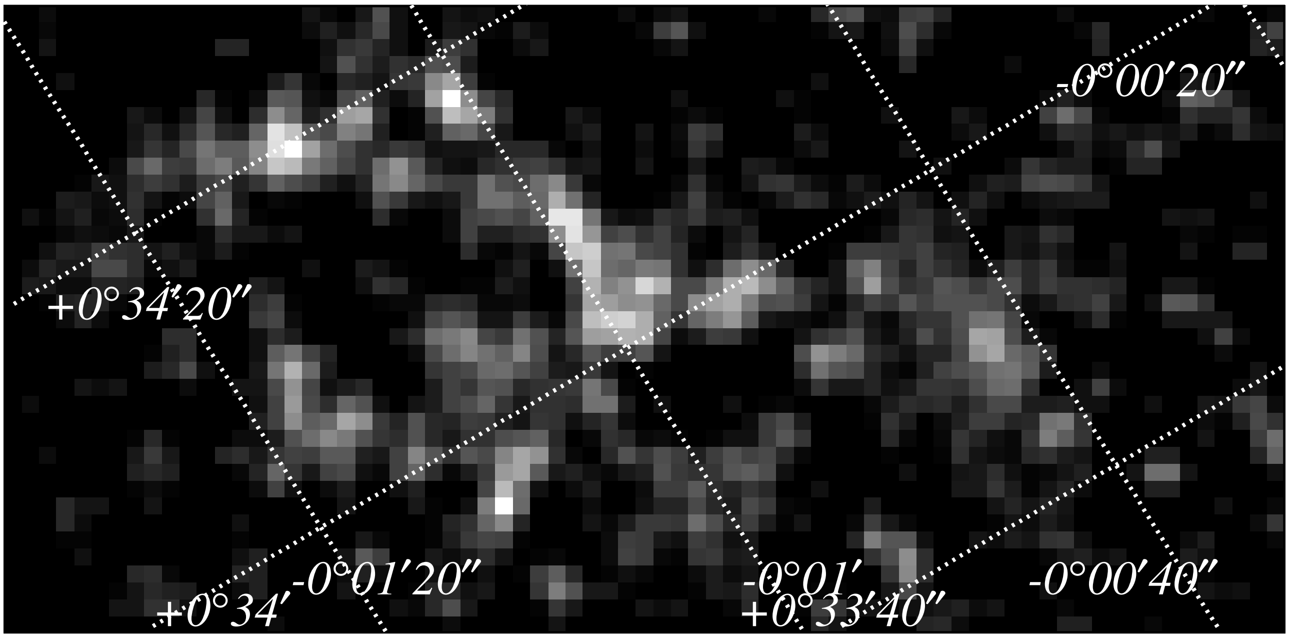

Figure 6.9: *Chandra* image of G0.570−0.018 in 4–7 keV band. A faint shell-like structure is shown.

Spectrum

The *Chandra* X-ray spectrum is made from the same area as with *ASCA*, while the background spectrum is taken from a source-free region with the same CTI effect as the source region. We fit the spectrum with a thermal bremsstrahlung and a Gaussian line, and obtained the best-fit parameters shown in Table 6.3. The parameters are consistent with the *ASCA* results within

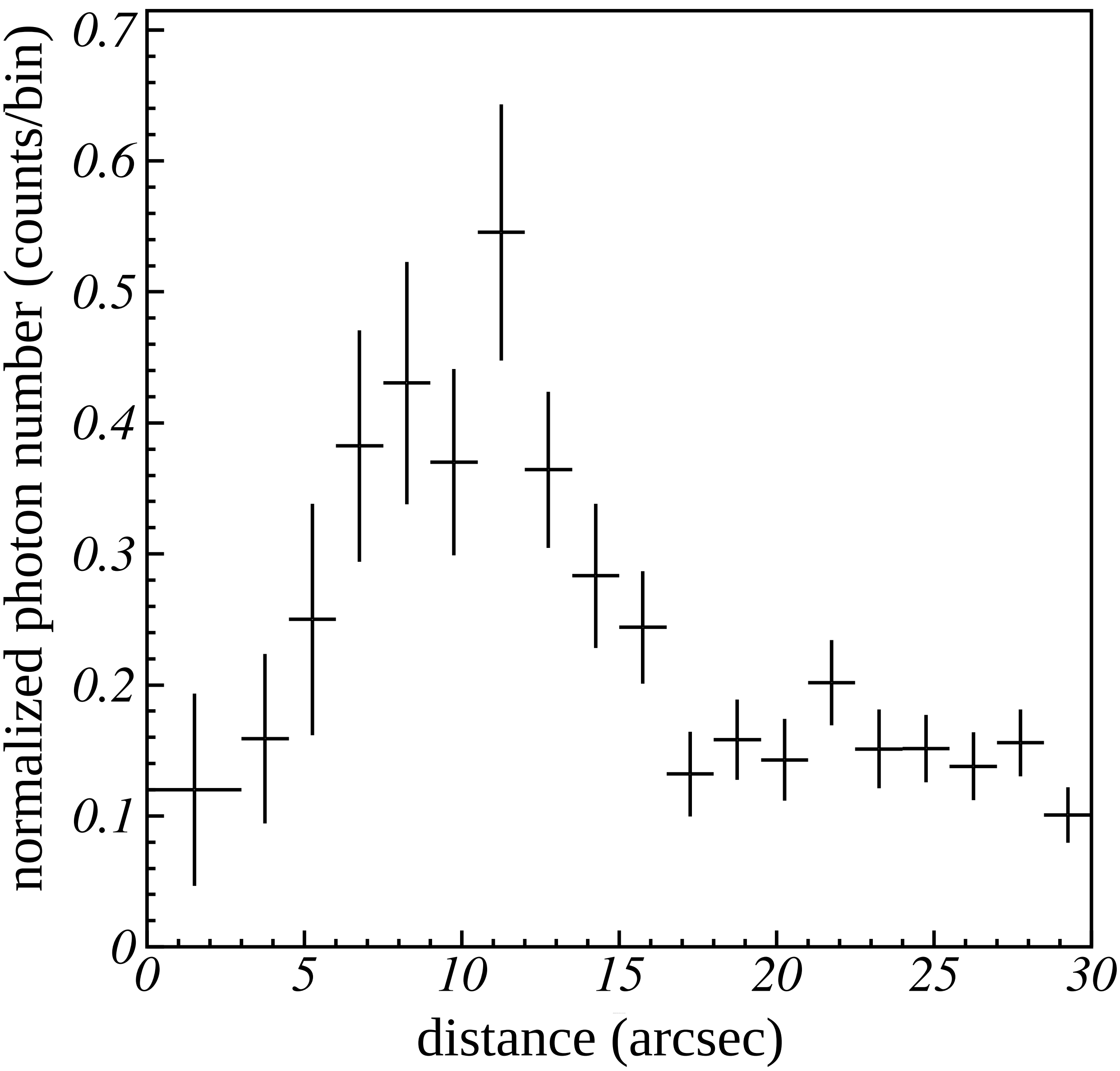

Figure 6.10: The radial profile of X-ray emissions from G0.570−0.018. The horizontal line shows the distance from the center of the shell-like structure.

90% errors. The center energy and the equivalent width of the iron line is 6.47–6.53 keV and 4.1 keV, respectively.

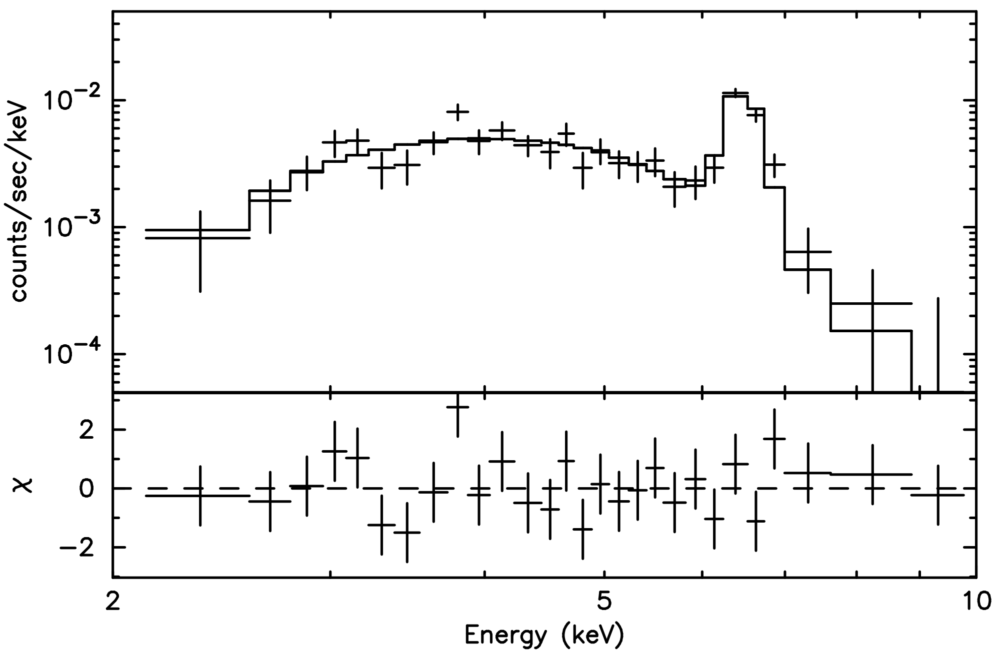

Figure 6.11: The X-ray spectrum of G0.570−0.018 obtained with *Chandra*.

6.2.3 Discussion

The faint X-ray emission discovered with *ASCA*, lately confirmed to have a shell-like structure. The spectrum can be reproduced with the thin thermal plasma model. These results imply that the X-rays are radiated from a SNR. In this section, we further investigate the properties of the G0.570−0.018.

Spectrum fitting with NEI model

Because the center energy of the line is smaller than that of the He-like iron, we fit the *ASCA* and the *Chandra* spectra simultaneously with NEI model. The best-fit parameters and spectra are shown in table 6.4 and figure 6.12, respectively. The ionization parameter nt is very small as $1.7{\times}10^{10}$ cm^{-3} s^{-1}. The X-ray emitting plasma is far from a collisional ionization equilibrium state. The hydrogen column density of $N_{\rm H} \sim 1.4 \times 10^{23}$ cm^{-2} is a consistent value with the interstellar absorption to the GC (Sakano 2000).

Table 6.3: Best-Fit Results of the X-ray spectrum of G0.570−0.018 obtained with *Chandra*.

	Continuum			Iron line				
	$N_{\rm H}{}^{\rm a}$	$kT^{\rm b}$	$F_{\rm X}{}^{\rm c}$	$E_{\rm C}^{\rm d}$	$F_{\rm X}{}^{\rm c}$	$EW^{\rm e}$	$L_{\rm X}{}^{\rm f}$	χ^2/d.o.f.
GIS	$11.9^{+3.4}_{-4.2}$	4.8(>3.4)	5.0 ± 0.4	6.50±0.03	$3.2^{+0.4}_{-0.3}$	4.1	13±1	26.2/22

^{a} : Hydrogen column density [10^{22}H cm^{-2}].

^{b} : The temperature of the plasma [keV].

^{c} : Flux (no correction of absorption) in the 2–10 keV band [10^{-13}erg cm^{-2} s^{-1}].

^{d} : Center energy of iron line [keV].

^{e} : Equivalent width of iron line [keV].

^{f} : Absorption corrected luminosity in the 2–10 keV band [10^{33}erg s^{-1}].

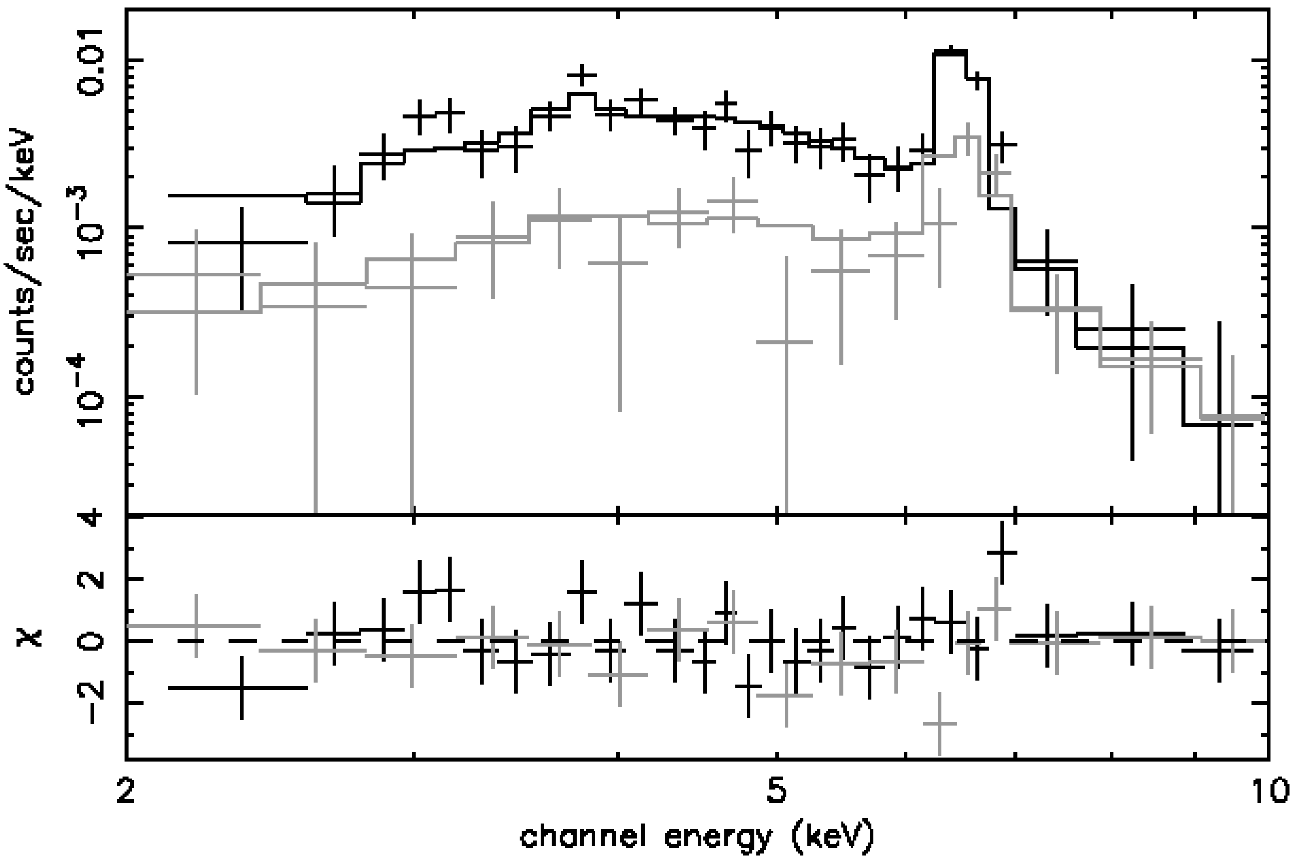

Figure 6.12: The simultaneously fitting of the *ASCA* (gray) and the *Chandra* (black) spectra. The solid lines show the best-fit spectra of NEI model.

Table 6.4: Best-Fit Results of the X-ray Spectrum with the simultaneously fitting of *ASCA* and *Chandra* with a NEI model

	Continuum						
GIS&ACIS	N_H [a]	kT [b]	nt	Z [c]	F_X [d]	L_X [e]	Reduced χ^2/d.o.f.
	$13.9^{+3.3}_{-3.2}$	$6.1^{+19.7}_{-3.0}$	$1.7^{+1.0}_{-0.4}$	$4.5^{+5.4}_{-2.9}$	8.2 ± 0.5	16^{+2}_{-1}	41.3/40

[a] : Hydrogen column density [10^{23}H cm^{-2}].

[b] : Plasma temperature of a thin thermal plasma model for the continuum spectrum.

[c] : Chemical abundance with ratio to solar abundance.

[d] : Flux (no correction of absorption) in the 2–10 keV band [10^{-6}photons cm^{-2} s^{-1}].

[e] : Absorption corrected luminosity in the 2–10 keV band [10^{33}erg s^{-1}].

Physical parameters

With the same procedure as G359.92−0.09, we estimate the density and the age of the plasma separately. From the image and the radial profile (section 6.2.2), we assumed the X-ray emitting region to be a spherical shell with the radius of $(10 \pm 3)''$ or 0.3–0.5 pc. Then the volume of the plasma is 1.2 $\times 10^{55}$ cm^3. The *E.M.* is derived from a new spectrum region with the smaller radius to exclude X-rays from the surrounding region. The *E.M.* is 5.5 $\times 10^{56}$ cm^{-3}, which is 67% of that of the whole area of G359.92−0.09. Then using the best-fit ionization parameter (nt) of 1.7 $\times 10^{10}$ cm^{-3} s, the plasma density (n) and the ionization age (t) are estimated to be 6.7 cm^{-3} and 80 year, respectively. The expanding velocity is about 4900 km s^{-1}. The age of the plasma is very young, and the SNR should be in a free expansion phase. In fact, the Sedov self-similar model leads the inconsistent results (Senda 2001).

Chapter 7

Results III. — Other Structures

With the high angular resolution of *Chandra*, we discovered many futures in the Galactic center region as well as SNRs or XRNs. In this section, we concentrate on new discoveries with *Chandra*.

Figure 7.1 shows the combined image of the *Chandra* observations of the Sgr A and the Radio Arc region. There are many clumps in the field (labeled 1–11). The filamentary structure is also found in the Sgr C region (Figure 5.8). This clump is labeled No. 12. As mentioned later, the physical properties are different from clump to clump; some show the 6.7 keV line, others are the 6.4 keV line emitters, and the others have non-thermal spectra. We classify the X-ray clumps based on the presence (absence) of iron K-line and its center energy (E_{C}); 6.4-keV clumps, 6.7-keV clumps, and non-thermal clumps. The detailed study of these clumps is made by Bamba et al. (2001).

In this chapter, we investigate the representative samples of these clumps. No. 2, 11 for non-thermal, No. 10, 12 for 6.4 keV, and No. 1 for 6.7-keV clumps.

7.1 Non-Thermal Clumps

7.1.1 No. 2 — G359.96−0.05

Image

Figure 7.2 shows the X-ray image and the radio continuum image of Sgr A region. The faint filamentary structure is found at the northeastern edge of Sgr A East. The X-ray structure is coincident with a faint radio filament. We named this structure G359.96−0.05 from the position in the Galactic coordinates.

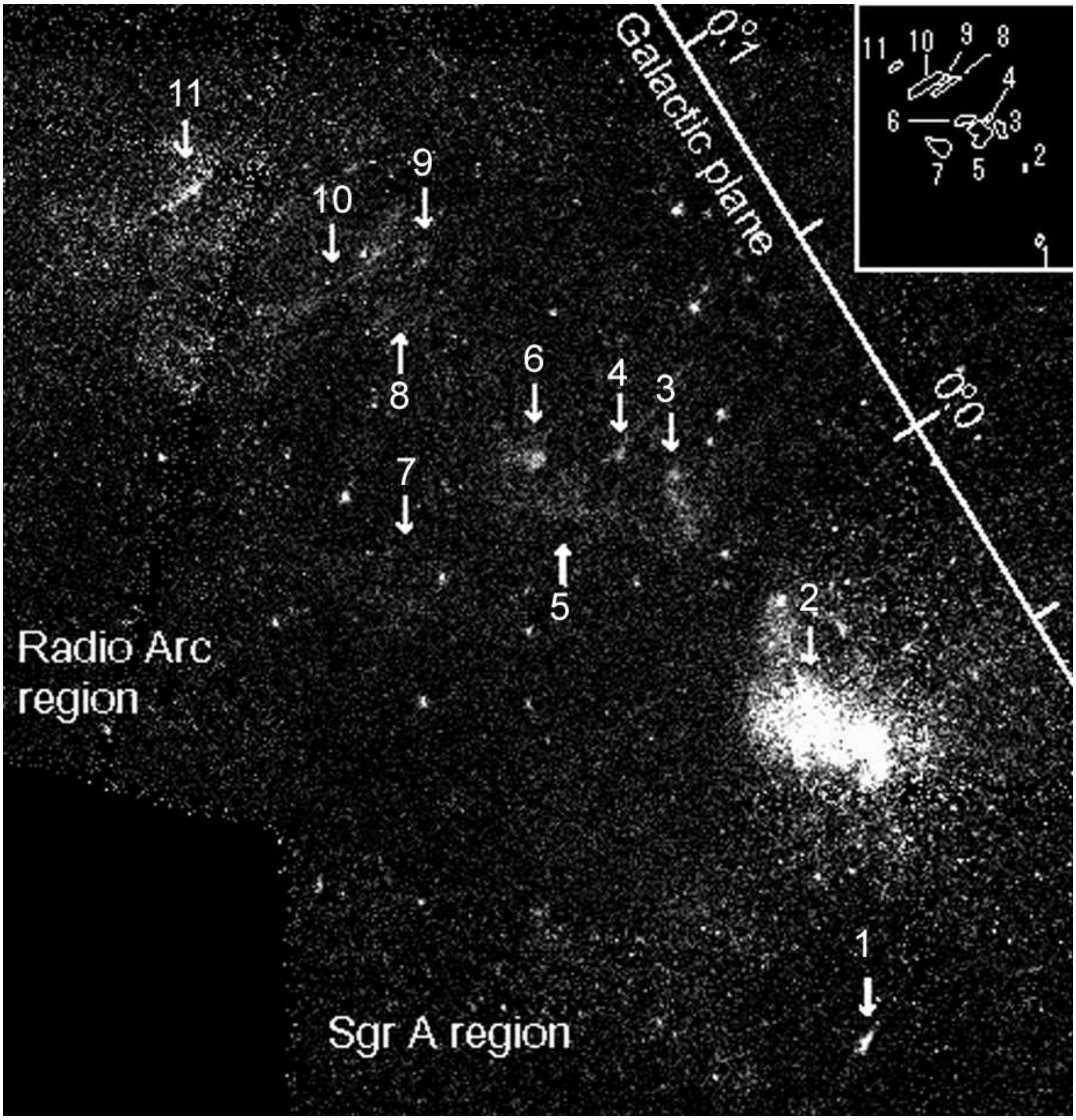

Figure 7.1: Merged image of the *Chandra* observations of the Sgr A and the Radio Arc region. Energy band is 3.0–8.0 keV. Many diffuse structures are shown, and indicated by number 1–11.

Spectrum

Figure 7.3 shows the X-ray spectrum of G359.96−0.05. The spectrum region is 3.″5×7″ rectangle surrounding the filament. The spectrum exhibits no line structure. We fit the spectrum with a power-law model, and obtain the best-fit parameters shown in Table 7.1. Due to the limited photon statistics, we cannot give significant constraint on the upper-limit of iron line intensity.

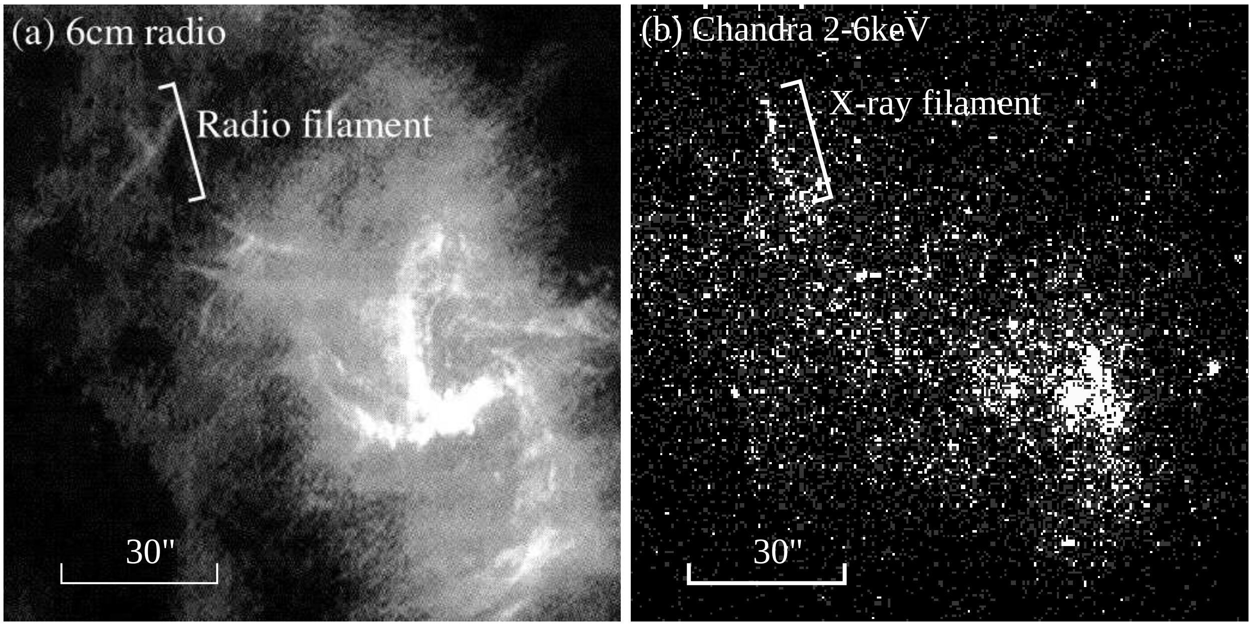

(a) Radio image (b) *Chandra* image

Figure 7.2: The X-ray and radio images of an X-ray filament G359.96−0.05. (a) and (b) show radio and *Chandra* images of the identical field around Sgr A* (Koyama 2001). The X-ray and radio filaments are located near at each other, implying physical correlation between them.

Table 7.1: Best-Fit Results of the X-ray spectrum of G359.96−0.05.

	Power-law				
	N_{H}[a]	Γ[b]	F_{X}[c]	L_{X}[d]	χ^2/d.o.f.
ACIS	$7.3^{+7.2}_{-5.5}$	$1.7^{+1.4}_{-0.6}$	$2.4^{+0.2}_{-0.3}$	$3.0^{+35.1}_{-0.6}$	9.5/15

[a] : Hydrogen column density [10^{22}H cm^{-2}].

[b] : Photon index of a power-law model for the continuum spectrum.

[c] : Flux (no correction of absorption) in the 2.0–10.0 keV band [10^{-13}erg cm^{-2} s^{-1}].

[d] : Absorption corrected luminosity in the 2.0–10.0 keV band [10^{33}erg s^{-1}].

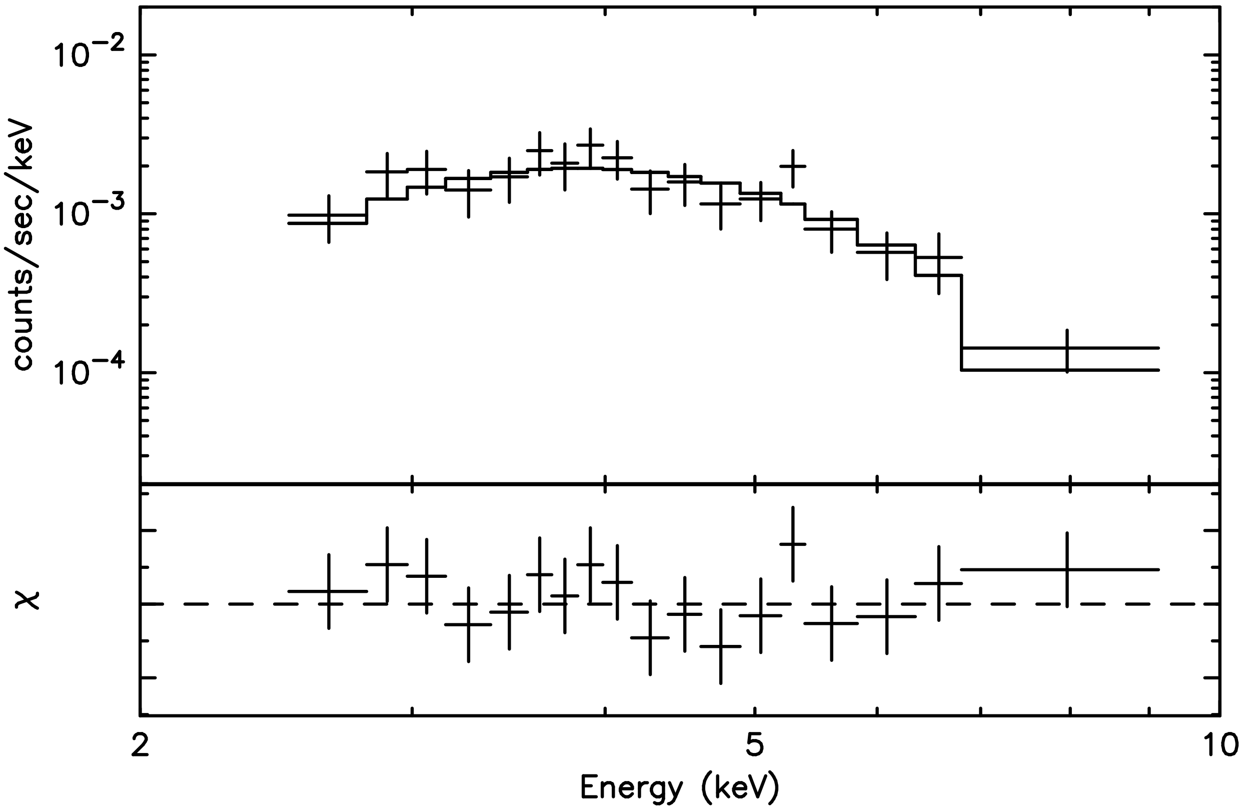

Figure 7.3: *Chandra* ACIS spectrum of G359.96−0.05. No line future is found.

Discussion

We found a filamentary structure at the Sgr A region. The spectrum shows no line structure, and can be reproduced with power-law model. The shape and the spectrum indicates that the X-rays from G359.96−0.05 is non-thermal origin, which may be attributable to a synchrotron emission by high energy electrons. Further verifications of the hypothesis requires more accurate observations in both radio and X-ray band.

7.1.2 No. 11 — G0.13−0.01

Image

Figure 7.4 shows the 3.0–8.0 keV band image of G0.13−0.01. It shows thin filamentary structure with the size of about $60'' \times 10''$. It is located at the edge of the molecular cloud M0.11−0.08 (section 5.3). Tsuboi, Ukita, & Handa (1998) and Oka et al. (2001) found an expanding shell at this side of the cloud.

Spectrum

We make the X-ray spectrum of G0.13−0.01 from the oval region surrounding the filament. Since G0.13−0.01 is buried in the diffuse X-ray emission from the cloud (section 5.3), we subtract the background spectrum extracted from the neighbor oval region. The spectrum and the background regions are shown in Figure 7.4a in solid and dashed lines, respectively.

The spectrum can be reproduced with a single power-law model. The best-fit spectrum and parameters are shown in Figure 7.4b and Table 7.2, respectively. To estimate the upper-limit of the iron line emission, we add a narrow Gaussian line with the fixed center energy of 6.4 or 6.7 keV. In both cases, the equivalent width of the line is $\lesssim$ 0.2 keV. Thus we conclude that G0.13−0.01 is a non-thermal filament.

Discussion

We detected the non-thermal emission from G0.13−0.01. Tsuboi, Ukita, & Handa (1997) and Oka et al. (2001) suggested that magnetic field is compressed by the interaction between the expanding shell and the molecular cloud, and electrons may be accelerated to relativistic energies through shock acceleration (section 2.3.3).

The X-rays from G0.13−0.01 should be synchrotron emission from high energy electrons. *Chandra* observation strongly support the hypothesis that this region is the cite of the electron

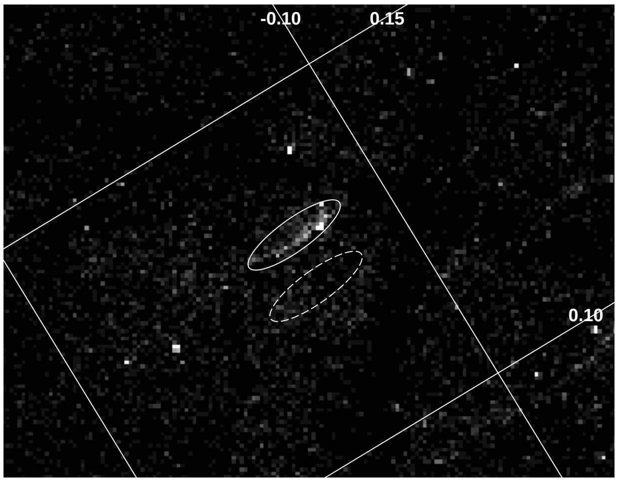

(a) *Chandra* image

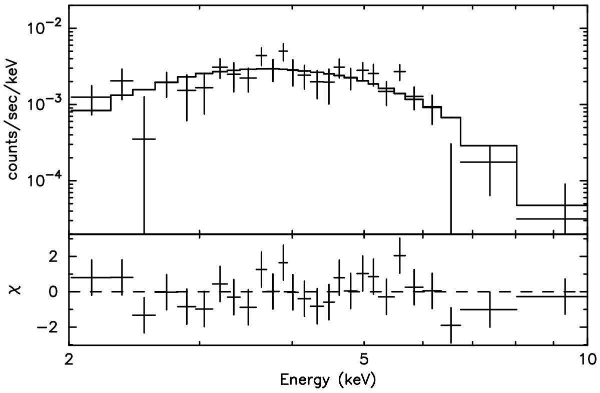

(b) *Chandra* spectrum

Figure 7.4: (a) 3.0–8.0 keV band image of G0.13−0.01 obtained with *Chandra*. Filamentary structure is shown in solid ellipse region. The dashed ellipse shows the background region. (b) *Chandra* spectrum of G0.13−0.01 fitted with a power-law model.

Table 7.2: Best-Fit Results of the X-ray Spectrum of G0.13−0.01.

	Power-law				
	$N_{\rm H}{}^{\rm a}$	$\Gamma^{\rm b}$	$F_{\rm X}{}^{\rm c}$	$L_{\rm X}{}^{\rm d}$	χ^2/d.o.f.
ACIS	$7.8^{+6.8}_{-3.3}$	$2.1^{+1.2}_{-0.8}$	$3.0^{+0.4}_{-0.3}$	4^{+39}_{-3}	23.0/25

^{a} : Hydrogen column density [10^{22}H cm^{-2}].

^{b} : Photon index of a power-law model for the continuum spectrum.

^{c} : Flux (no correction of absorption) in the 2.0–10.0 keV band [10^{-13}erg cm^{-2} s^{-1}].

^{d} : Absorption corrected luminosity in the 2.0–10.0 keV band [10^{33}erg s^{-1}].

acceleration. Note that the strong radio emission is outside of the cloud, and not coincident with G0.13−0.01 (see Figrue 2.5).

7.2 6.4-keV Clumps

7.2.1 No. 10 — G0.09−0.09

Image

Figure 7.5a shows the 3.0–8.0 keV image around G0.09−0.09. There is a filamentary structure with the size of $\sim 160'' \times 16''$. This filament is located at the edge of the M0.11−0.08 cloud on the GC side (see Figure 5.12).

Spectrum

Figure 7.5b shows the spectrum of G0.09−0.09. The spectrum and the background regions are shown in Figure 7.5a. We first fit the spectrum with a power-law and a narrow Gaussian line model. Though this model allows acceptable fittings, the photon index of the power-law model cannot be constrained in significant range. We then fix the photon index Γ to be 2.0, and obtain the best-fit parameters as shown in Table 7.3. The center energy is $\sim$ 6.4 keV, and consistent with that of neutral iron. The absorption column of $\sim 3 \times 10^{23}$ H cm^{-2} is larger than interstellar absorption to the GC region (Sakano 2000).

Discussion

As seen in Figure 5.12, this filament is located at the GC side of M0.11−0.08. The spectrum exhibits strong iron line with the equivalent width of $\sim$ 1 keV, and large absorption. These futures suggest that G0.09−0.09 is an XRN, which emits fluorescent and scattered X-rays. A small condensation of molecular material may be located at this position, and emit fluorescent X-rays. More detailed radio observations of molecular lines are required to reveal the origin of the X-ray emission.

7.2.2 No. 12 — G359.42−0.13

Image

We found the faint elongated structure in iron line image at the Sgr C region (Figure 5.8a). It is also found in 3.0–8.0 keV image (Figure 7.6a), which is perpendicular to the Galactic

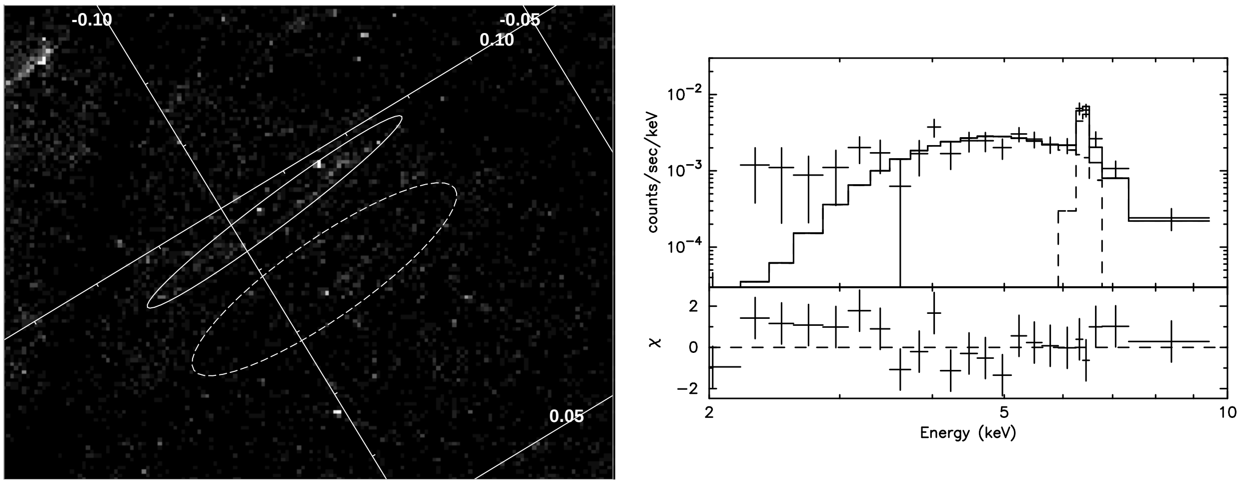

Figure 7.5: (a) 3.0–8.0 keV band image of G0.09−0.09 obtained with *Chandra*. Very faint filamentary structure is detected (solid ellipse). The dashed line shows the background region. (b) *Chandra* spectrum of G0.09−0.09. A strong iron line is detected.

Table 7.3: Best-Fit Results of the X-ray Spectrum of G0.09−0.09.

		Power-law		Iron line				
	$N_{\rm H}{}^{\rm a}$	$\Gamma^{\rm b}$	$F_{\rm X}{}^{\rm c}$	$E^{\rm d}$	$F_{\rm X}{}^{\rm c}$	$EW^{\rm e}$	$L_{\rm X}{}^{\rm f}$	Reduced χ^2 (d.o.f.)
ACIS	$27.7^{+9.3}_{-8.4}$	2.0 (fixed)	4.5±0.6	$6.42^{+0.04}_{-0.05}$	$0.9^{+0.3}_{-0.2}$	$1.1^{+0.2}_{-0.3}$	13^{+5}_{-4}	21.2/20

^{a} : Hydrogen column density [10^{22}H cm^{-2}].

^{b} : Photon index of a power-law model for the continuum spectrum.

^{c} : Flux (no correction of absorption) in the 2.0–10.0 keV band [10^{-13}erg cm^{-2} s^{-1}].

^{d} : Absorption corrected luminosity in the 2.0–10.0 keV band [10^{33}erg s^{-1}].

plane. The size is about $5' \times 1'.5$. It is not coincident with radio filaments or molecular clouds (Figure 2.4).

Spectrum

The spectrum of G359.42−0.13 is shown in Figure 7.6b. The spectrum and background regions are shown in Figure 7.6a by solid and dashed lines, respectively. The spectrum shows a line emission at 6–7 keV. We then fit the spectrum with a power-law and a narrow line model. The best-fit parameters are shown in Table 7.4. The center energy of the line agrees with the neutral iron, and the column density of hydrogen is $\sim 5 \times 10^{22}$ H cm^{-2}.

Discussion

We detected strong iron line from from G359.42−0.13, but the absorption is rather small. It is consistent or smaller than interstellar absorption to the GC region. The small absorption is contrary to the XRN mechanism. One possibility is that the emission line is from low-ionized iron, or X-rays are from NEI plasma. In fact, NEI plasma model can reproduce the spectrum with the best-fit parameters as follows: $N_{\rm H} \sim 9 \times 10^{22}$, $kT \sim 2.6$ keV, and the the ionization parameter $nt \sim 3 \times 10^{10}$ (χ^2/d.o.f = 5.0/9). X-ray flux is 9×10^{-13} erg s^{-1} cm^{-2} in 2–10 keV band. Though the limited photon statistics prevents us from further study, G359.42−0.13 may be a young SNR like G0.570−0.018.

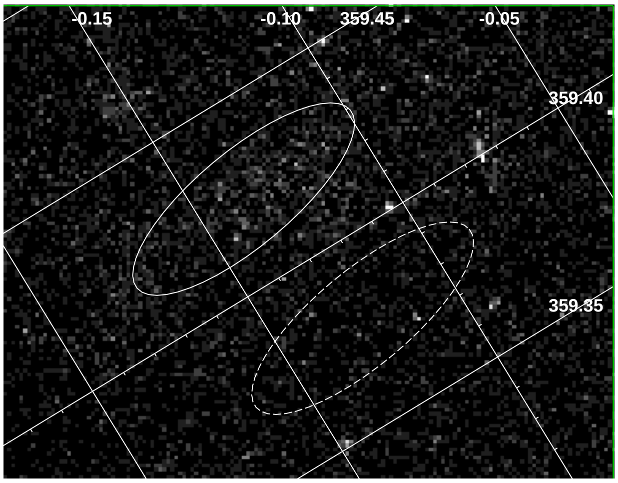

(a) *Chandra* image of G359.42−0.13

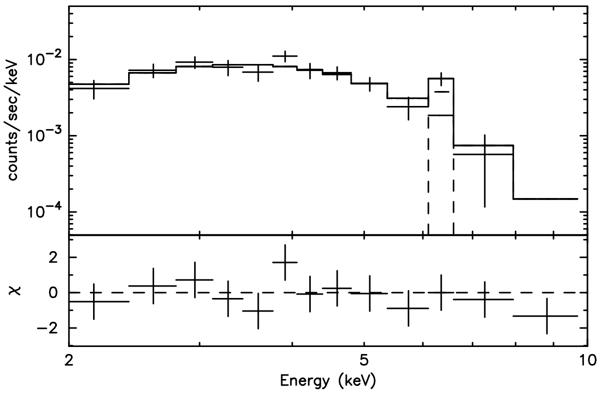

(b) *Chandra* spectrum of G359.42−0.13

Figure 7.6: (a) 3.0–8.0 keV band image of G359.42−0.13 obtained with *Chandra*. The concentration of the X-ray emission is shown in solid ellipse region. Dashed line shows the background region. (b) *Chandra* spectrum of G359.42−0.13. Iron line is detected at ~ 6.4 keV.

Table 7.4: Best-Fit Results of the X-ray Spectrum of G359.42−0.13.

		Power-law			Iron line			
	$N_{\mathrm{H}}{}^{\mathrm{a}}$	Γ^{b}	$F_{\mathrm{X}}{}^{\mathrm{c}}$	E^{d}	$F_{\mathrm{X}}{}^{\mathrm{c}}$	EW^{e}	$L_{\mathrm{X}}{}^{\mathrm{f}}$	Reduced χ^2 (d.o.f.)
ACIS	$5.3^{+1.4}_{-0.9}$	2.0 (fixed)	9.2±1.0	$6.38^{+0.19}_{-0.21}$	$1.3^{+0.5}_{-0.6}$	1.0±0.5	12^{+3}_{-2}	7.8/9

^{a} : Hydrogen column density [10^{22}H cm^{-2}].

^{b} : Photon index of a power-law model for the continuum spectrum.

^{c} : Flux (no correction of absorption) in the 2.0–10.0 keV band [10^{-13}erg cm^{-2} s^{-1}].

^{d} : Absorption corrected luminosity in the 2.0–10.0 keV band [10^{33}erg s^{-1}].

7.3 6.7-keV Clumps

7.3.1 No. 1 — G359.88−0.08, a part of G0.570−0.018

We detected filamentary structure at the south of the Sgr A region. The spectrum exhibits 6.7-keV line, and the distribution is coincident with a radio structure of "wisp".

The nature of this clump is already studied in section 6.1, and G359.88−0.08 is revealed to be a part of SNR. The spectrum and the image of this structure are shown in section 6.1.

Thus 6.7-keV clumps are possible to be SNRs. We can find new SNRs in the Galactic center by the X-ray observations.

Chapter 8

Discussion

We revealed that;

- giant molecular clouds emit 6.4-keV line
- there are new faint SNRs in the GC region
- there are numerous new X-ray features in the GC region

in the previous chapters. We discuss the implication of these results in this chapter.

8.1 Verification and Consequence of the X-ray Reflection Nebula

In chapter 5, we investigate the giant molecular clouds in the GC region, and revealed that all clouds emit strong 6.4-keV line. Since the 6.4-keV line is a characteristic line from neutral iron atoms, we suspect that the cloud is irradiated by an external luminous X-ray source. This hypothesis is confirmed by the simulated spectra and image (only Sgr B2) of the XRN model.

However, there remains an important problem; what is the primary X-ray source (or primary X-ray sources) to radiate molecular clouds? In this section, we investigate what is the external primary source.

8.1.1 Required Luminosity

From the equation (5.2), (5.3), we calculate the fractions of the reflected and fluorescent fluxes, hence estimate the required luminosity of the primary source to give the observed fluxes of continuum X-rays and the 6.4-keV photons.

At first, we estimate the luminosity of primary source of Sgr B2. We adopt the best-fit values of $\eta = 0.2$, and $(Z_{\rm Fe}, Z_{\rm others}) = (2.5,\ 2.0)$ for this analysis. The required luminosity is,

$$L_{2-10\rm keV} \sim 10^{39} \left(\frac{d}{100\rm pc}\right)^2 \rm erg\ s^{-1}, \tag{8.1}$$

where d is the distance from the primary X-ray source to Sgr B2. Since the reflecting region is extended largely over the Sgr B2 cloud, the required X-ray flux should be the value averaged over a time of about 100 yr. This may exclude galactic binary transient sources as the primary X-ray, whose duty cycle of flaring may be very short. We hence compare the required flux with the observed luminosities of rather stable sources found in the catalog near the GC in Table 8.1 (Sakano et al. 2001).

The observed luminosities of cataloged bright X-ray sources near the GC are 2–46 $\times 10^{36}$ erg s^{-1}, which are much lower than that required to explain the reflected luminosity of Sgr B2. The present X-ray sources cannot produce the strong fluorescent X-rays observed from the molecular clouds. As already mentioned, the luminosity of internal point sources are also insufficient. In fact, required luminosity exceeds the Eddington luminosity of neutron star.

This "no luminous primary source" problem leads to an exciting consequence; there was a very luminous X-ray source in the GC region in the past. The plausible candidate of the past luminous X-ray source is the massive black hole Sgr A*, as already proposed in Koyama et al. (1996). Sgr A* was bright some hundreds of years ago, the light travel time between Sgr A* and Sgr B2, and is dim at present. The shifted X-ray images of Sgr B2 and Sgr C support that the primary X-ray source is in the direction of GC.

Table 8.1: Comparison between Required Luminosities and the Observed Ones

X-ray sources	d^a	$L^b_{\rm obs}$	$L^c_{\rm req}$
1E 1740.7−2942	233	3	5400
A 1742−294	175	3	3000
1E 1743.1−2843	62	2	380
SLX 1744−299/300	250	4	6300
GX 3+1	275	46	7600

[a]: The projected distance to Sgr B2 [pc].

[b]: The observed luminosity in the 2–10 keV band (Sakano et al. 2001) [10^{36} erg s^{-1}].

[c]: The required luminosity to account for the observed X-ray fluxes of Sgr B2 [10^{36} erg s^{-1}].

If the primary source of Sgr B2 is the Galactic nucleus (not a neighborhood of Sgr B2), the other clouds are also irradiated by the same primary source. We further verify the primary source by the required luminosities for other clouds.

Table 8.2 shows the required luminosities for other clouds in case the primary source is Sgr A*. The errors are derived only by the errors in observed luminosities. We use the same parameters as Sgr B2: $\eta = 0.2$, and $(Z_{\rm Fe}, Z_{\rm others}) = (2.5, 2.0)$ for Sgr C and Clump 2. However, since these values are not in the 90% acceptance region of M0.11$-$0.08, we adopt the best-fit values of $(Z_{\rm Fe}, Z_{\rm others}) = (1.5, 0.5)$ with $\eta = 0.2$ for M0.11$-$0.08.

SgrC, which is at almost the same distance as Sgr B2 from Sgr A*, requires smaller luminosity. However, considering the systematic uncertainties in spectral analysis[1], these values are consistent. In fact, *ASCA* results requires about $7 \pm 2 \times 10^{38}$ erg s^{-1}, which is consistent with that of Sgr B2.

Required luminosity for Clump 2 is also consistent. While, M0.11$-$0.08 requires an order of magnitude lower than other three clouds. It may be attributable to long time variability of Sgr A*, because M0.11$-$0.08 is closest to Sgr A*. We conclude that fluorescent X-rays from all of the cloud can be explained by past activities of the Galactic nucleus Sgr A*.

Table 8.2: Required Luminosities of Sgr A* to explain the observed intensity of fluorescent and scattered X-rays.

	$l_{\rm II}$ [deg]	$b_{\rm II}$ [deg]	d^a [pc]	$I^b_{6.4}$ [$\times 10^{-5}$ ph cm^{-2}]	$L^c_{\rm SgrA}$ [10^{38} erg s^{-1}]
SgrB2	0.67	-0.03	109	5.6	9^{+3}_{-2}
SgrC	-0.56	-0.05	76	1.4	3^{+3}_{-2}
M0.11$-$0.08	0.12	-0.11	28	3.7	0.7 ± 0.1
Clump2	2.67	0.00	409	0.4	5^{+4}_{-3}

[a] : The distance from the Sgr A* to the cloud.

[b] : The observed intensity of 6.4-keV line.

[c] : The required luminosity of Sgr A* to produce the observed 6.4-keV line emission. The errors are derived only by the errors in observed luminosities.

8.1.2 The Past Activities of the Galactic Nucleus

In the previous subsection, we estimated the required luminosities to explain the X-ray intensity of four molecular clouds. These luminosities should indicate the past luminosity of Sgr A* corresponding to the light travel time from Sgr A* to each cloud. We thus convert the distance

[1]There is another uncertainty in the radial distance to us.

from Sgr A* to elapsed time, and make a light curve for the past 2000 years (Figure 8.1). The luminosity is almost constant until a few hundreds years ago, and seems to decrease gradually to the present value. However, there is only five data points. We cannot discuss the detailed variability. The time span of each data point corresponds to the size of the cloud. Our method is also insensitive to time variability in shorter time scale.

The past activity of Sgr A* would be generated by a surge of accretion on the MBH due, for example, to the passage of dense shell of a young supernova remnant Sgr A East as is discussed by Maeda et al. (2001) based on the new *Chandra* results of the GC. They estimated the age of SNR to be $\sim 10^4$ years, and the dense shell reached Sgr A* $\sim 10^3$ years ago. Then the shell swept the surrounding matter, and the luminosity became anomalously low. This time scale agrees with the derived light curve by the XRN model. The luminosity could be as bright as the Eddington luminosity of 3 $\times 10^{44}$ erg s^{-1}, which is also enough to explain the intensity of fluorescent X-rays. Coker (2001) further confirmed this results, and predicted that the luminosity of Sgr A* should increase over the next $\gtrsim 10^3$ years as the accreting matter is accumulated again by cluster's winds.

Hence our results of past activities of Sgr A* suggest that Sgr A* is accidentally in a low luminosity phase at present.

8.1.3 Mass and Abundance of the Cloud

Oka et al. (1998) proposed that the molecular clouds in the GC region is in pressure equilibrium. In this case, the masses of the clouds become about an order of magnitude smaller, and the total mass within the central 400 pc of the Galaxy is (2–6) $\times 10^7$ $M_\odot$.

The total mass of the Galactic center is estimated by several methods. Diffuse γ-ray in the Galaxy is mainly produced with interaction of cosmic ray and matter. The total mass can be estimated by diffuse γ-ray flux. Hence the upper limit of the total mass was given as 6×10^7 $M_\odot$ within 500 pc (Blitz et al. 1985). Sakano (2000) also estimated the total mass within less than 380 pc to be 6.4×10^7 $M_\odot$ from the absorption column to bright X-ray sources in the GC region. This value is thought to be a upper limit since it is derived by assuming the solar abundance. If the abundance is higher than solar value, it is reduced by a factor.

Thus all observations favor pressure equilibrium. We estimated the mass of the cloud to be < 0.3 times gravity equilibrium mass. Our result also supports the pressure equilibrium.

Chemical abundances of the GC region is also an important problem. It has been debatable whether the GC region is overabundant or not (section 2.1.1). Our results of Sgr B2 shows

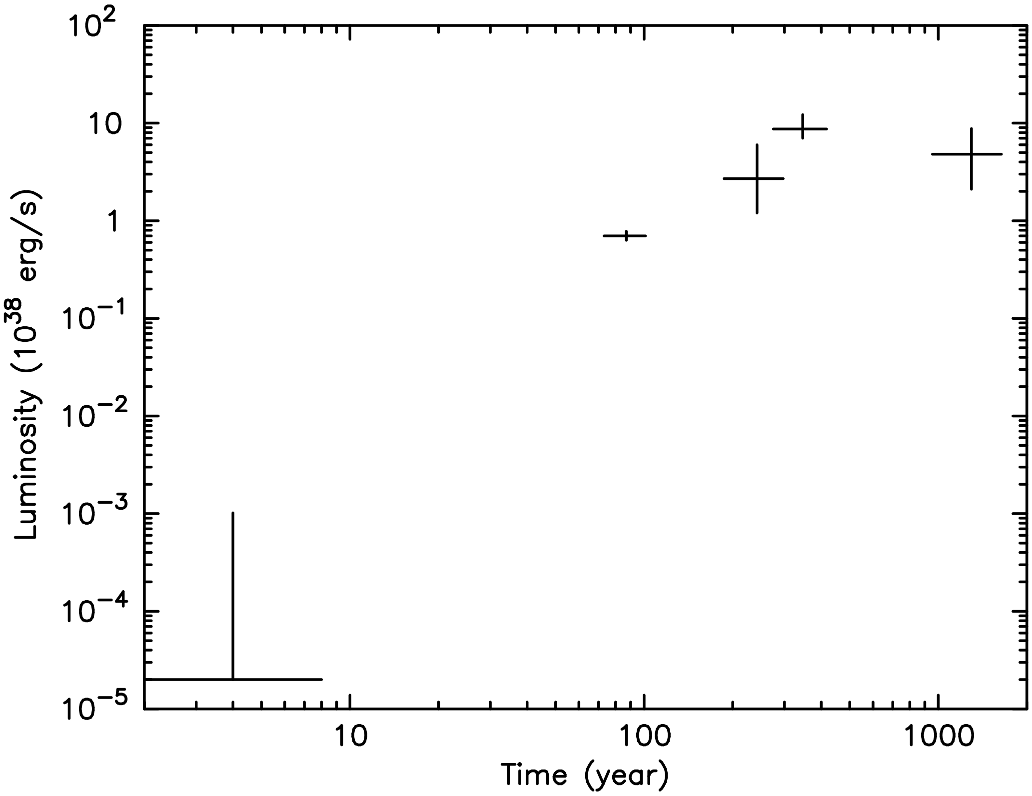

Figure 8.1: The time variability of the Sgr A* for the past 2000 years derived by XRN simulation. The luminosities are estimated by fittings of observed spectra with simulations of XRN model for -100 – -2000 years ago. The time span corresponds to the size of each cloud. The luminosity of recent 10 years is from the direct observations with *ASCA* and *Chandra* (Maeda 1996; Baganoff et al. 2001a, 2001b).

overabundance with $1.5 \lesssim Z_{\rm Fe} \lesssim 3.0$ and $2.0 \lesssim Z_{\rm others} \lesssim 5.0$ ($\eta = 0.2$, here and hereafter). While we only obtained lower limit of $Z_{\rm Fe}$, and upper limit of $Z_{\rm others}$ in case of Sgr C, M0.11−0.08, and Clump 2. M0.11−0.08, in particular, shows the upper limit of $Z_{\rm others} \lesssim 1.0$, which is inconsistent with other clouds. If it is a real feature, the abundances are different from cloud to cloud. However, the spectrum of M0.11−0.08 includes thermal component. It may arise systematic uncertainty to reduce the abundance. If we underestimate the X-ray flux of thermal component, absorption in lower energy band becomes smaller, and lower abundance is obtained.

$Z_{\rm Fe}$ is constrained to be $\gtrsim 1.0$ for all the clouds. The iron abundance is mainly determined by equivalent width of the fluorescent iron line. The line structures generally have better photon statistics than continuum emission, and the ratio of fluorescent and scattered X-rays are not affected by the cloud shape. Thus the abundance of iron has relatively good confidence than that of other lighter elements.

The XRN scenario has a potentiality to determine the total gas mass and chemical abundances. However, since the assumed density distribution may not be valid for image analysis, further observations, especially in radio band, are essential to obtain accurate parameters.

8.1.4 Further Verifications

Our hypothesis of XRN is confirmed by numerical simulations of image and spectrum. Future observations will further confirm the hypothesis of XRN.

The most convincing evidence is a detection of polarized X-rays. The scattered X-rays are polarized perpendicular to the direction of primary X-rays. Churazov, Sunyaev, & Sazonov (2001) estimated the degree of polarization to be about 33%. Polarized X-rays also can be a good probe to determine the direction of primary X-ray source. This method is valid even for the small cloud, which is optically thin to the center, and the X-ray image is not shifted from the center.

We can investigate the short time variability of the primary source by the evolution of X-ray image. Sunyaev & Churazov (1998) simulated the morphology of the surface brightness distribution, the equivalent width and the shape of the fluorescent line from the Sgr B2 cloud as a function of time and relative position of the XRN and the primary (irradiating) source. They examined both the cases of a flare-like and a step-function (X-ray flux is constant but suddenly decreases to zero) irradiation by an X-ray source. As they demonstrated, a short time variability is the key to investigating the nature of the irradiating source, whether it is the Galactic nucleus or a binary X-ray source. For comparison with data, some observations with high angular resolution are necessary. The *Chandra* resolution of 0.5 arcsec, for example, can attain the time resolution of about 1 month, which is typical flare duration of a transient binary.

8.2 Origin of the High Temperature Plasma

With the high angular resolution of *Chandra*, we discovered new SNRs and SNR candidates from the GC region (chapter 6, 7). SNRs are one of the most plausible candidates to produce the high temperature plasma filling the central $1^\circ \times 2^\circ$ region of our Galaxy. In this section, we investigate the contribution of SNRs to high temperature plasma.

8.2.1 Energy Injection

The temperature of the GC plasma is $\sim$ 10 keV. Since the Galactic gravity cannot confine such a high temperature plasma, the plasma is expanding. If we assume the expanding speed to be the sound velocity ($v \sim 1600$ km s^{-1}), it takes about 50000 yr to reach the present size (Koyama 1996). It means that the energy of 10^{54} erg is injected into the GC region within the past 50000 yr.

One SNR releases about 10^{51} erg. Then a thousand of SNRs are required to produce the total energy. If supernova explosion rate is constant, it corresponds to one supernova per 50 yr. We discovered two SNRs, which is younger than 10^4 yr. In addition, Maeda et al. (2001) revealed that the shell-like radio structure Sgr A East is also a SNR with the age of $\sim 10^4$ yr. We then assume that we can observe SNRs which are younger than 10000 yr by $\sim$ 50 ksec observations.

With this assumption, we estimate the expected number of SNRs in the GC region. Long exposure observations are made at three regions (Sgr A, Radio Arc, and Sgr B2). The net observed area is about 800 arcmin^2. While, the size of the GC plasma is $1.^\circ 8 \times 1.^\circ 0 \simeq 5100$ arcmin^2, which is about 6.4 times of the long exposed area. Thus we simply estimate that about 20 SNRs younger than 10000 yr are hidden in the short exposed or not observed area in the GC region. The number of SNRs which is younger than 50000 yr becomes 100. It is an order of magnitude lower than required number. Thus SNRs discovered till now explain only 10% of the total energy of the GC plasma.

However, there may be additional SNRs in the GC region. Some fractions of newly discovered clumps may be SNRs. Radio observations discovered numerous shell-like structures from the GC region (e.g. Oka et al. 2001), which may also be SNRs. The discovery of G0.570−0.018 may be a piece of evidence that there are many supernovae in the GC region. The age of this SNR is $\sim$ 80 yr, which is near the expected supernova rate. Further observations in X-ray and radio wavelength would reveal the accurate contribution of SNRs.

8.2.2 Temperature

The temperature is also a difficult problem to explain the high temperature plasm by SNRs. The temperature of GC plasma is $\sim$ 10 keV, which is much higher than that of the Galactic SNR. This fact cause doubt on a thermal origin of the GC plasma (Tanaka et al. 2000)

Newly discovered SNRs in the GC region tend to show high temperature compared with Galactic SNRs out of the GC region. For example, the temperature of G0.570−0.018 is $\sim$ 6 keV, and that of G359.92−0.09 is $\sim$ 11 keV. If it is common to GC SNRs, high temperature of the GC plasma can be explained. However, observed temperatures have very large errors. It is not certain whether these SNRs really exhibit high temperature comparable to the plasma temperature. The lower limit of these temperatures are $\sim$ 3 keV. Further detail observations and studies for the evolution of SNR in peculiar environment in the GC are required.

Bibliography

[1] Baganoff, F., et al. 2001a, ApJ, submitted, (astro-ph 0102151)

[2] Baganoff, F. K. et al. 2001b, Nature, 413, 45

[3] Balick, B. & Brown, R. 1974, ApJ, 194, 265

[4] Bally, J., Stark, A. A., Wilson, R. W., & Henkel, C. 1988, ApJ, 324, 223

[5] Balucinska-Church, M. & McCammon, D. 1992, ApJ, 400, 699

[6] Bamba, A., Koyama, K., Murakami, H., Senda, A., Takagi, S., & Yokogawa, J. 2002

[7] Bambynek, W., Crasemann, B., Fink, R. W., Freund, H.-U., Mark, H., Swift, C. D., Price, R. E., & Rao, P. V. 1972, Reviews of Modern Physics 44, 716

[8] Bania, T. M. 1977, ApJ, 216, 381

[9] Burke, B. E., Mountain, R. W., Harrison, D. C., Bautz, M. W., Doty, J. P., Ricker, G. R., & Daniels, P. J. 1991, IEEE Trans., ED-38, 1069

[10] Burke, B. E., Mountain, R. W., Daniels, P. J., and Dolat, V. S. 1994, IEEE Trans. Nuc. Sci., 41, 375

[11] Benson, J. M. & Johnston, K. J. 1984, ApJ, 277, 181

[12] Binette, L., Dopita, M. A., D'Odorico, S., & Benvenuti, P. 1982, A&A, 115, 315

[13] Carr, J. S., Sellgren, K., & Balachandran, S. C. 2000, ApJ, 530, 307

[14] Coil, A. L. & Ho, P. T. P. 1999, ApJ, 513, 752

[15] Coil, A. L. & Ho, P. T. P. 2000, ApJ, 533, 245

[16] Coker, R. F. 2001, A&A, 375, L18

[17] Churazov, E., Sunyaev, R., & Sazonov, S. MNRAS accepted astro-ph/0111065

[18] de Pree, C. G., Gaume, R. A., Goss, W. M., & Claussen, M. J. 1995, ApJ, 451, 284

[19] de Pree, C. G., Gaume, R. A., Goss, W. M., & Claussen, M. J. 1996, ApJ, 464, 788

[20] de Pree, C. G., Goss, W. M., & Gaume, R. A. 1998, ApJ, 500, 847

[21] de Vicente, P., Martín-Pintado, J., Neri, R., & Colom, P. 2000, A&A, 361, 1058

[22] Dotani, T., Yamashita, A., Ezuka, H., Takahashi, K., Crew, G., Mukai, K., & the SIS Team 1997, The *ASCA* news (Greenbelt: NASA GSFC), 5, 14

[23] Ebeling, H., White, D. & Rangarajan, V. 2000, MNRAS, submitted

[24] Feigelson, E. D. & Montmerle, T. 1999, ARAA, 37, 363

[25] Feldman, U. 1992, Physica Scripta, 46, 202

[26] Gaume, R. A., & Claussen, M. J. 1990, ApJ, 351, 538

[27] Genzel, R., Hollenbach, D., & Townes, C. H. 1994, Reports of Progress in Physics, 57, 417

[28] Genzel, R., Eckart, A., Ott, T., & Eisenhauer, F. 1997, MNRAS, 291, 219

[29] Gotthelf, E. 1996, The *ASCA* news (Greenbelt: NASA GSFC), 4, 31

[30] Hasegawa, T., Morita, K.-I., Okumura, S., Kaifu, N., Suzuki, H., Ohishi, M., Hayashi, M., & Ukita, N. 1985, in Masers, Molecules and Mass Outflows in Star Forming Regions, ed. A. D. Haschick (Westford: Haystack Observatory), 275

[31] Hayashida et al. 1999, Astroprticle Physics, 10, 303

[32] Henke, B. L., Lee, P., Tanaka, T. J., Shimabukuro, R. L., & Fujikawa, B. K. 1982, Atomic Data and Nuclear Data Tables, 27, 1

[33] Ho, P. T. P., Jackson, J. M., Barrett, A. H., & Armstrong, J. T. 1985, ApJ, 288, 575

[34] Houghton, S., & Whiteoak, J. B. 1995, MNRAS, 273, 1033

[35] Inoue, H. 1985, Space Science Reviews, 40, 317

[36] Ishisaki, Y. 1997, Ph.D. Thesis

[37] Johnson, W. N., Harnden, F. R., & Haymes, R. C. 1972, ApJL, 172, L1

[38] Kawai, N., Fenimore, E. E., Middleditch, J., Cruddace, R. G., Fritz, G. G., Snyder, W. A., & Ulmer, M. P. 1988, ApJ, 330, 130

[39] Kinzer, R. L., Milne, P. A., Kurfess, J. D., Strickman, M. S., Johnson, W. N., & Purcell, W. R. 2001, ApJ, 559, 282

[40] Koyama, K., Awaki, H., Kunieda, H., Takano, S., & Tawara, Y. 1989, Nature, 339, 603

[41] Koyama, K., Maeda, Y., Sonobe, T., Takeshima, T., Tanaka, Y., & Yamauchi, S. 1996, PASJ, 48, 249

[42] Koyama, K. 2001, ASP Conf. Ser. 251: New Century of X-Ray Astronomy, in press (astro-ph/0108109)

[43] Kuan, Y. -J. & Snyder, L. E. 1996, ApJ, 470, 981

[44] Lindqvist, E., Sandqvist, Aa., Winnberg, A., Johanssoun, L.E.B., and Nyman, L.-Å. ApJ 1995, 113, 257

[45] Lis, D. C., & Goldsmith, P. F. 1989, ApJ, 337, 704

[46] Lis, D. C., Goldsmith, P. F., Carlstrom, J. E., & Scoville, N. Z. 1993, ApJ, 402, 238

[47] Lis, D. C. & Carlstrom, J. E. 1994, ApJ, 424, 189

[48] Liszt, H. S. & Spiker, R. W. 1995, ApJS, 98, 259

[49] Liu, S. Y., Mehringer, D. M., Miao, Y., & Smyder, L. E. 1998, ApJ, 501, 680

[50] Maeda, Y., Koyama, K., Sakano, M., Takeshima, T., & Yamauchi, S. 1996, PASJ, 48, 417

[51] Maeda, Y. 1998, Ph.D. Thesis

[52] Maeda, Y. et al. 2001, ApJ, in press (astro-ph/0102183)

[53] Makishima, K., et al. 1996, PASJ, 48, 171

[54] Martín-Pintado, J., de Vicente, P., Rodríguez-Fernández, N. J., Fuente, A., & Planesas, P. 2000, A&A, 356, L5

[55] Mehringer, D. M., Goss, W. M., & Palmer, P. 1994, ApJ, 434, 237

[56] Mehringer, D. M. 1995, ApJ, 454, 782

[57] Mehringer, D. M., & Menten, K. M. 1997, ApJ, 474, 346

[58] Melia, F. & Falcke, H. 2001, ARAA, 39, 309

[59] Mezger, P. G., Duschl, W. J., & Zylka, R. 1996 A&A Review, 7, 289

[60] Morita, K.-I., Hasegawa, T., Ukita, N., Okumura, S. K., & Ishiguro, M. 1992, PASJ, 44, 373

[61] Morris, M. & Serabyn, E. 1996, ARAA, 34, 645

[62] Morrison, R & McCammon, D. 1983, ApJ, 270, 119

[63] Murakami, H., Koyama, K., Sakano, M., Tsujimoto, M., & Maeda, Y. 2000, ApJ, 534, 283

[64] Murakami, H., Koyama, K., Tsujimoto, M., Maeda, Y., & Sakano, M. 2001, ApJ, 550, 297

[65] Murakami, H., Koyama, K., & Maeda, Y. 2001, ApJ, 558, 687

[66] Narayan, R., Mahadevan, R., Grindlay, J. E., Popham, R. G., & Gammie, C. 1998, ApJ, 492, 554

[67] Ohashi, T., et al. 1996, PASJ, 48, 157

[68] Oka, T., Hasegawa, T., Hayashi, M., Hanada, T., & Sakamoto, S. 1998, ApJ, 493, 730

[69] Oka, T., Hasegawa, T., Sato, F., Tsuboi, M., and Miyazaki, A. (2001) PASJ 53, 779

[70] Prantzos, N. 1998, IAU Symp. 188: The Hot Universe, 188, 31

[71] Purcell, W. R. et al. 1997, ApJ, 491, 725

[72] Sakano, M., Yokogawa, J., & Murakami, H. 1999, Japanese-German Workshop on High Energy Astrophysics, 113

[73] Sakano, M. 2000, Ph.D. Thesis

[74] Sakano, M., Koyama, K., Murakami, H., Maeda, Y., & Yamauchi, S. 2001, ApJS, accepted (astro-ph/0108376)

[75] Sato, F., Hasegawa, T., Whiteoak, J. B., & Miyawaki, R. 2000, ApJ, 535, 857

[76] Senda, A., Murakami, H., & Koyama, K. 2001, ApJ, in press (astro-ph/0110011)

[77] Serlemitsos, P. J., et al. 1995, PASJ, 47, 105

[78] Shiki, S., Ohishi, M., & Deguchi, S. 1997, ApJ, 478, 206

[79] Sidoli, L., Mereghetti, S., Treves, A., Parmar, A. N., Turolla, R., & Favata, F. 2001, A&A, 372, 651

[80] Simons, D. A., Hodapp, K.-W., & Becklin, E. E. 1990, ApJ, 360, 106

[81] Skinner, G. K. et al. 1987, Nature, 330, 544

[82] Stark, A. A. & Bania, T. M. 1986 ApJ, 306, L17

[83] Stark, A. A., Bally, J., Gerhard, O. E., & Binney, J. 1991, MNRAS, 248, 14P

[84] Syunyaev, R., Pavlinskii, M., Churazov, M. G. E., Grebenev, S., Markevich, M., Dekhanov, I., Yamburenko, N., & Babalyan, G. 1991, Soviet Astronomy Letters, 17, 42

[85] Sunyaev, R. & Churazov, E. 1998, MNRAS, 297, 1279

[86] Takagi, S., Murakami, H., & Koyama, K. 2001, submitted to ApJ

bibitemTanaka94 Tanaka, Y., Inoue, H., & Holt S. S. 1994, PASJ, 46, L37

[87] Tanaka, Y., Koyama, K., Maeda, Y., & Sonobe, T. 2000, PASJ, 52, L25

[88] Tsuboi, M., Handa, T., & Ukita, N. 1999, ApJS, 120, 1

[89] Tsuboi, M., Ukita, N., & Handa, T. 1997, ApJ, 481, 263

[90] Vogel, S. N., Genzel, R., & Palmer, P. 1987, ApJ, 316, 243

[91] Yamashita, A. et al. 1997, IEEE Trans. Nuc. Sci., 44, 847

[92] Yamashita, A. 1998, Ph.D. Thesis

[93] Yamauchi, S., Kawada, M., Koyama, K., Kunieda, H., & Tawara, Y. 1990, ApJ, 365, 532

[94] Yusef-Zadeh, F., Morris, M., & Chance, D. 1984, Nature, 310, 557

[95] Yusef-Zadeh, F. & Morris, M. 1987, ApJ, 320, 545

[96] Yusef-Zadeh, F., Melia, F., & Wardle, M. 2000, Science, 287, 85

[97] Zylka, R., Mezger, P. G., & Wink, J. E. 1990, A&A, 234, 133

Acknowledgments

I am deeply thankful to Prof. K. Koyama for his 5-year guidance of X-ray astronomy. He gave me many precious advises and told me the attitude to research works. I would like to express my gratitude to Dr. Y. Maeda and Dr. M. Sakano. They always give me valuable suggestions. The large portion of this work is based on their pioneer works. I am indebted to Ms. A. Bamba and Mr. A. Senda for the analysis of a SNR and faint structures in the Galactic center.

I thank all the members of *ASCA* and *Chandra* team. These wonderful X-ray satellites are essential for my study for the Galactic center. Some of the *ASCA* data is obtained by a part of *ASCA* Galactic Plane/Center survey project. I am grateful to the principal investigator, Dr. S. Yamauchi. He also gave me many useful suggestions. I also use the data of the Galactic center survey with *Chandra*, which are contributed by Prof. Q. D. Wang.

I am deeply grateful to Prof. G. Garmire and Dr. Y. Tsuboi for their kind treatment in my stay at Pennsylvania State University to analyze *Chandra* data. I also had good discussions with Prof. E. Feigelson. I am helped by Dr. K. Ebisawa, Y. Terashima in my visit to NASA/GSFC.

Many people give me useful suggestions. I thank to Dr. T. Oka, Prof. T. Hasegawa, Prof. F. Sato, Mr. T. Sawada. I am grateful to Drs. H. Matsumoto, H. Tomida, K. Hamaguchi, and M. Nishiuchi for their kind instruction in X-ray astrophysics and analysis software.

I acknowledge all the people in Cosmic Ray laboratory in Kyoto University for their support and encouragement. I spent pleasant days with them. This work is financially supported by the Japan Society for the Promotion of Science.

I especially thanks to my family and my friends, finally.